

Electronic Thesis and Dissertation Repository

12-16-2016 12:00 AM

Nanoscale Thermal and Electronic Properties of Thin Films of Graphene and Organic Polyradicals

Sabastine Chukwuemeka Ezugwu, *The University of Western Ontario*

Supervisor: Prof. Fanchini Giovanni, *The University of Western Ontario*

A thesis submitted in partial fulfillment of the requirements for the Doctor of Philosophy degree in Physics

© Sabastine Chukwuemeka Ezugwu 2016

Follow this and additional works at: <https://ir.lib.uwo.ca/etd>

 Part of the [Condensed Matter Physics Commons](#), and the [Optics Commons](#)

Recommended Citation

Ezugwu, Sabastine Chukwuemeka, "Nanoscale Thermal and Electronic Properties of Thin Films of Graphene and Organic Polyradicals" (2016). *Electronic Thesis and Dissertation Repository*. 4304. <https://ir.lib.uwo.ca/etd/4304>

This Dissertation/Thesis is brought to you for free and open access by Scholarship@Western. It has been accepted for inclusion in Electronic Thesis and Dissertation Repository by an authorized administrator of Scholarship@Western. For more information, please contact wlsadmin@uwo.ca.

Abstract

Ultrathin film materials have attracted significant attention in light of their potential applications in very large scale integrated electronics and data storage. The amount of data that can be addressed and stored in memory devices scales inversely with the thickness of the active layer of these components and ultrathin thermal sinks are required to evacuate heat from memory devices and other electronic components. In our thesis, we have developed a suite of scanning-probe and nano-optical techniques focused on understanding the electronic surface properties and thermal conductivity of ultrathin materials. We discuss a few specific examples in which we applied these techniques towards improved performance of thin films of graphene and organic polyradicals towards specific applications. A new nano-optical technique, near field scanning thermoreflectance imaging (NeSTRI), has been invented and implemented by us for contactless imaging of the thermal properties of graphene thin films and poly-[1,5-diisopropyl-3-(cis-5-norbornene-exo-2,3-dicarboxiimide)-6-oxoverdazyl] (P6OV). We utilized Kelvin-probe force microscopy for understanding the surface properties of copper nanoparticle decorated graphene thin films with superior electrical conductivity, and to design energy level matched flash memory devices from P6OV. Our work has led to deeper understanding of the nanoscale thermal and electronic properties of thin films of graphene and organic polyradicals and the interplay between their performance and fabrication parameters.

Keywords:

Graphene thin films, Organic polyradicals, Graphene-polymer composites, Graphene-copper nanoparticles, Thermal and electronic properties, Ultrathin memory devices, Kelvin probe force microscopy, Scanning near field optical microscopy, scanning near field thermoreflectance imaging.

Co-Authorship Statement

This thesis contains material from published and submitted papers. Sabastine Ezugwu was supervised by Prof. Giovanni Fanchini over the course of this thesis work. Prof. Fanchini contributed to the general direction of all the papers presented in this thesis.

The work presented in Chapter 2 was done in collaboration with Mr. Sina Kazemian. Mr. Kazemian, with some collaboration from Mr. Dong-Yup Choi, performed the theoretical modelling for extracting the thermal properties from experimental data as well as discussion of the results from his model. I built the NeSTRI set-up and did all the experiments, including graphene-based thin film fabrication, NeSTRI measurement and discussion of the experimental results. The literature review was done on a 50% – 50% basis. Dr. Reg Bauld gave technical support for the NeSTRI set-up. The paper is currently under review in Nanoscale.

The work presented in Chapter 3 was done in collaboration with Dr. Arash Akbari-Sharbat and Dr. Shafiq Ahmed. Dr. Ahmed prepared some of the graphene-thin films, and others were supplied directly by Prof. Fanchini. I did Cu-NPs deposition, UV-Vis transmittance measurements, AFM/KPFM measurements, experimental data analysis and literature review of the experiments. Dr. Akbari-Sharbat contributed to SEM, on a 50-50% basis, theoretical data analysis and literature review and he performed the theoretical modelling in collaboration with Prof. Cottam. Dr. Reginald Bauld also contributed to the optimization of the KPFM. The work has been published in Carbon.

The work presented in Chapter 4 was done entirely by me under guidance of Prof. Fanchini.

In Chapter 5, the polyradicals used for the memory device fabrication were synthesized by Dr. Joseph A. Paquette from Western's Department of Chemistry, under guidance of his supervisor,

Prof. Joe B. Gilroy. Dr. Paquette also provided graphs with the chemical structure of P6OV, presented in Figure 1.10 of Chapter 1. I did the experimental work, analysis, literature review and discussion relating to: thin film fabrication from raw material provided by Dr. Paquette, thin film characterization, and device design and assembling. Prof. Fanchini contributed with the model for explaining the electrical, optical and memory properties of these systems. Mr. Vishal Yadav, an OMG exchange student, contributed, under immediate guidance from myself and Prof. Fanchini, to some preliminary thin film deposition and electrical characterization experiments (not presented here) and is therefore indicated as an author in the resulting paper, although the actual experiments leading to the discovery of the transport properties and memory effects in P6OV, which are reported in this thesis, are not his. This work has been published in *Advanced Electronic Materials*.

The polyradicals used to fabricate polymer/graphene nanocomposites reported in Chapter 6 were synthesized by Dr. Paquette under guidance of Prof. Gilroy. Mr. Luis Santana, a MITACS Globalink international exchange student, deposited the graphene-based thin film used for this work, with inputs from myself and Prof. Fanchini. Mr. Santana also carried out, under the same guidance, the UV-Vis transmittance measurements reported in this chapter. I performed the I-V and NeSTRI measurements on these samples, before and after P6OV incorporation, literature review, data analysis and discussion, with inputs from Prof. Fanchini for measurement interpretation.

Acknowledgments

I would like to express my gratitude to my supervisor, Prof. Giovanni Fanchini for his immense support over the entire time I worked with him in pursuance of my PhD degree. He provided for me terrific opportunity after opportunity for outstanding research experience, including inter-departmental, faculty and industrial research collaborations. And as I mention elsewhere, Prof. Giovanni not only provides direction, he is also very generous with his time in attending to and offering useful and insightful discussions. I also wish to acknowledge Dr. Arash Akbari-Sharbat for his support in many different ways too numerous to mention! He has been a superb friend and colleague, and an excellent resource of inspiration when it mattered most. I wish him the best of luck continuing his research as a post-doctoral fellow. I would like to express my gratitude to my advisory committee members; Prof. Peter Simpson and Prof Lyudmila Goncharova. Many thanks for your insightful advice and support.

Also worthy of mention are many people connected to this thesis through useful collaboration, especially Dr. Joseph Paquette and Prof. Joe Gilroy of Chemistry department, Dr. Shafiq Ahmad, Dr. Reg Bauld, Mr. Sina Kazemian, Dr. Ranjith Divigalpitiya of 3M Canada and Mr. Luis Santana. I would like to thank other members of Giovanni's group, past and current students: Dr. Faranak Sharifi, Dr. Paul Bazylewski, Jaewoo Park, Miguel H. Boratto, Ouyang Teeno, Edith Yeung, Shahbaz Masood and Li Ye. I would like to thank all these people for their insightful views, especially at group meetings.

I would also like to acknowledge the foundation to my graduate studies laid by Prof. Fabian Ezema and all the support received from Prof. P. U. Asogwa, both at The University of Nigeria, Nsukka. I am indebted to both of you for the progress and achievement in my academic pursuit.

Finally, and most importantly, I would like to express my utmost gratitude to my lovely wife, Angela, my son, Ebubechukwu and daughter, Madeleine for all the support, love, prayer and encouragement. I love and cherish you all!

Table of Contents

Abstract	i
Co-Authorship Statement.....	ii
Acknowledgments.....	iv
Table of Contents	vi
List of Figures	x
List of Appendices	xxiv
List of Symbols, Variables and Abbreviations	xxv
Chapter 1: Thin film materials used in this thesis and their characterization methods.....	1
1.1 Objectives and background	1
1.2 Characterization techniques used in this work.....	4
1.2.1 Atomic force and scanning near field optical microscope.....	4
1.2.2 Scanning near field optical microscopy operation	7
1.2.3 Atomic force microscopy/Scanning Kelvin Probe force microscopy system.....	9
1.2.3.1 Tip calibration and work function determination.....	12
1.3 Materials used in this thesis	12
1.3.1 Graphene and graphene-based thin films.....	12
1.3.1.1 Preparation of graphene-based thin films.....	14
1.3.2 Organic Polyradicals (OPR)	17
1.3.2.1 Synthesis of stable organic radical polymers.....	19
1.3.2.2 Preparation of poly-[1,5-diisopropyl-3-(cis-5-norbornene-exo-2,3-dicarboxiimide)-6-oxoverdazyl]	19

1.3.2.3 Application of organic polyradicals in memory devices	22
1.4 Electrical transport in polymer materials	25
1.4.1 Poole Frankel transport	25
1.4.2 Ohmic transport processes	27
1.5 Conclusions	29
References	30

Chapter 2: Nanoscale Thermal Imaging of Graphene-based Thin Films

2.1 Scanning Near-Field Thermoreflectance Imaging	35
2.1.1 Existing thermal imaging techniques	35
2.1.2 A new thermal imaging technique	37
2.2 NeSTRI Apparatus	39
2.3 Materials	44
2.4 Numerical model	45
2.5 Results	49
2.5.1 Sample absorbance	49
2.5.2 Multi-frequency NeSTRI imaging	53
2.6 Discussion	58
2.7 Conclusion	60
References	61

Chapter 3: Nanoscale investigation of graphene-based thin films decorated with copper Nanoparticles

3.1	Introduction	64
3.2	Experimental	66
3.3	Results.....	68
3.3.1	Control of Cu-NP's size and distribution on graphene surface	68
3.3.2	Transparency of graphene thin films decorated with Cu-NPs	68
3.3.3	The work function of graphene-based thin film decorated with Cu-NPs.....	70
3.4	Theoretical results	73
3.5	Comparison and discussion of theoretical and experimental results.....	77
3.6	Conclusion	83
	References	84

Chapter 4: Thermal conductivity of Cu-NP decorated multi-layer graphene platelets

4.1	Introduction	87
4.2	Methods	89
4.3	Results and Discussion	92
4.3.1	Topography and SNOM transmittance and reflectance images	92
4.3.2:	NeSTRI images	94
4.4	Conclusion	99
	Reference	99

Chapter 5: Physical Properties of Organic Polyradical P6OV and Its Bistability

5.1	Introduction	102
5.2	Experimental	104
5.2.1	Device Fabrication	104
5.2.2	Characterization	107
5.3	Current–Voltage Characteristics and Electronic Energy Levels in P6OV	108
5.4	Memristor Design Criteria	115
5.5	Memristor Performance	120
5.6	Conclusion	125
	References	126

Chapter 6: Electrical, Optical and Thermal properties of P6OV:Graphene nanocomposites

6.1	Experimental	130
6.1.1	Thin film deposition	130
6.1.2	Characterization of P6OV/Graphene nanocomposites	132
6.2	Optical images of Graphene and P6OV/Graphene nanocomposites	133
6.3	Electrical conductivity of Graphene and P6OV/Graphene nanocomposites	139
6.4	Thermoreflectance imaging of P6OV/Graphene nanocomposites	143
6.5	Conclusion	149
	References	150

Chapter 7: Conclusion and Future work

7.1.	Conclusions	152
7.2.	Future Work	155

List of Figures

Figure 1.1: Scheme of the characterization apparatus utilized for nanoscale investigation of surface electronic and thermal properties of specific ultrathin materials and devices studied in this thesis. Kelvin probe force microscopy (KPFM), an atomic force microscopy (AFM) – based technique is used for nanoscale mapping surface electronic properties. Scanning near-field optical microscopy (SNOM) is adapted and modified for thermal imaging3

Figure 1.2: Atomic interaction forces between the AFM tip and the sample surface, which define the modes of AFM operation into contact, non-contact and tapping modes5

Figure 1.3: Schematic of the Witec Alpha 300S atomic force microscope (right) used in this work. On the left is a magnified image of a confocal microscope and hollow AFM cantilever that permit near field optical imaging of the studied sample.....6

Figure 1.4: Far field and near field obtained when incident probe light is scattered from nano-hole of diameter, d machined at the end of an atomic force microscope cantilever. Scattered wave is observed at distances that is of the order of the wavelength of the light.7

Figure 1.5: Schematic of AFM/SNOM system showing the collection of probe laser light for operation in transmission and reflection modes.....8

Figure 1.6: Schematic diagram of Kelvin Probe Force Microscopy. A lock in amplifier used at the second resonance frequency of the cantilever is operated in amplitude modulation mode. In this mode, the tip-sample electrostatic force is measured directly from the amplitude of the

cantilever using a lock-in amplifier referenced to the AC potential signal by a function generator.
.....10

Figure 1.7: The schematic structure of (a) graphene and (b) graphite. Graphene is one atom thick planar sheet while graphite consists of stacked layers ($N \sim \infty$) of graphene weakly bonded by van der Waals forces13

Figure 1.8: Preparation steps for the fabrication of graphene thin films. Graphene is prepared in solution based on exfoliation of graphite using RNA as surfactant. The resultant graphene layer in solution is vacuum-filtrated on a membrane and subsequently transferred on desired substrate. The middle image is the picture of filtration setup in Fanchini’s group laboratory in the Department of Physics and Astronomy at Western University. The last image is the picture of graphene thin films on glass substrate of different thicknesses obtained from different filtration volumes of graphene/RNA suspension16

Figure 1.9: Classification of organic radicals based on the atom centres into (a) nitrogen-centred radicals, (b) carbon-centred radicals, (c) nitroxide based and (d) oxygen-centred radicals. The dot on each atomic centre represents a singly-occupied electronic orbital (e) The general structure of verdazyl radicals. A family of verdazyl based polyradicals are developed by replacing the X group with atoms or groups such as carbonyl group or thiocarbonyl group.18

Figure 1.10: Synthesis steps for the production of poly-[1,5-diisopropyl-3-(cis-5-norbornene-exo-2,3-dicarboxiimide)-6-oxoverdazyl] – polymer 13 (P6OV), the polyradical used in this thesis work for the fabrication of organic memory device. The synthesis steps consist of (1) condensation, (2) oxidation, (3) esterfication and (4) polymerization reactions.
.....20

Figure 1.11: Resistive switching in a typical radical polymer based memory device. The device which was initially in a low conductivity state (I_{DA}) is activated to high conductivity state at the threshold voltage, V_{write} . The high conductivity state persists during a positive biasing (I_{EBC}) until another threshold voltage, V_{erase} which returns the device to low conductivity state. The voltage range at which no transition occurs, V_{read} , can be used to read and understand the state of the device.24

Figure 1.12 (a) I-V curves of highly insulating polymer thin film showing non-ohmic, Poole-Frenkel-like behavior [30]. The polymer used in ref. 30 is poly-[1,5-diisopropyl-3-(cis-5-norbornene-exo-2,3-dicarboxiimide)-6-oxoverdazyl].....27

Figure 1.13: (a) The current – voltage curves of a polymer-based thin films at four different thicknesses in high conductivity state, which were fitted with straight lines to demonstrate ohmic transport [30]. (b) Film resistivity values obtained from the low-voltage portions of I-V curves. Resistivity is thickness-independent in the high conductivity state, while it dramatically increases at decreasing thickness in the low-conductivity state, possibly due to preferential alignment of polymer filaments along the substrate.....29

Figure 2.1: (a) (a) Setup used for recording transmission (τ) and reflection (ρ) SNOM images, from which $A_0(x,y)$, the absorbance of the sample can be obtained and used to determine the heat generation profile according to eq.(2). (b) NeSTRI setup used for scanning near-field thermoreflectance images in phase ($\delta\phi_0$) and amplitude ($\delta\rho_0$). A 405-nm pump beam, modulated at frequency ω , heats the sample over a large area from the inverted microscope. Heat, after diffusing along the thin film surface, is transferred to air. Air changes in volume and thus experiences, at a certain phase lag, periodic changes in refractive index that induce small oscillations in reflectance at the air-sample interface.

Such oscillations are probed, in amplitude and phase, by a CW 532-nm probe beam originating from the upright SNOM microscope and detected in lock-in mode via the SMA coupler. A set of filters at the SMA coupler eliminate 405-nm light scattered from the pump beam.41

Figure 2.2: Picture of different pieces of apparatus coupled used to achieve our NeSTRI measurement. (a) Witec Alpha 300S aperture-type AFM/SNOM system in Fanchini’s group laboratory in the Department of Physics and Astronomy at Western University (b) A magnified view of the system showing the upright confocal microscope for focusing the probe green laser onto the hollow AFM tip, scan stage and the reflection mode accessory. The inverted microscope used to focus the pump beam laser is not visible in this picture. (c) The pump beam laser, mechanical chopper for frequency modulation of pump beam and the pump beam optics for focusing and alignment. (d) The controller of the mechanical chopper and dual phase lock-in amplifier.....43

Figure 2.3: (a) AFM topography, (b) SNOM CW reflectance, and (c) amplitude and (d) phase of thermoreflectance modulations recorded from a multilayer graphene flake. The pump laser, modulated at $\omega = 150$ Hz, was switched off and on every 128 lines of a 512-line sample scan. Pump laser modulation has no effects on the topography and CW reflectance images, but it is essential for observing thermoreflectance images50

Figure 2.4: (a) AFM topography, (b) Transmission mode and (c) Reflection mode SNOM images of graphene platelets comprising of different number of layers. The topography was obtained simultaneously during SNOM measurements. (d) Absorbance, A_0 versus number, N of graphene layers. The absorbance was determined from the transmittance and reflectance data obtained from the SNOM images in (b) and (c). Multilayer graphene

platelets are highly absorbing, while few-layer are semi-transparent. All of them are weakly reflecting.52

Figure 2.5: (a) NeSTRI amplitude and (b) phase images recorded at 75 Hz pump beam modulation frequency in non-contact from the test sample. Dotted squares highlight the detail that is further investigated in figures 2.6 to 2.8. Negative phase is a consequence of $h < 0$ in eq. 2.6 and is a strong indication of the fact that images are from genuine complex thermoreflectance signals. An excellent correlation between NeSTRI images in the present figure and the corresponding contact AFM and SNOM images from figure 2.4 can be observed.54

Figure 2.6: (a) Detail of AFM and (b) SNOM reflectance images of multilayer graphene (MLG) flake from figure 2.4. (c) Thermo-reflectance amplitude and (d) phase at $\omega = 45$ Hz frequency and (e) thermoreflectance amplitude and (f) phase at $\omega = 450$ Hz. It is always observed $\delta\phi_0(x,y) < 0$, as a consequence of $h < 0$ in eq. 6 which means that $\delta\rho(x,y,t)$ and $T(x,y,t)$ are in phase opposition of 180° . (g) The amplitude monotonically decreases as ω increases, as a consequence of shorter thermal diffusion length at increasing frequency. (h) The phase in graphene increases from about -1.6° to nearly zero and, from comparison of panels d and f, it is evident that $\delta\phi_0$ is lower in graphene than glass at 25 Hz, while, at 450 Hz, it is lower in glass than graphene55

Figure 2.7: (a) Large thermal diffusion length (L_{th}) at low frequency, dominated by the diameter (D_G) of graphene flake, with heat dissipation mainly occurring in glass, and (b) Large thermal diffusion length at high frequency, in which eq. 2.10 holds and heat dissipation mainly occurs in graphene. A smaller phase lag occurs from the medium from which the largest amount of heat is dissipated to air. The dependency of L_{th} on ω leads to the 150 Hz crossover between regimes a

and b, which results in phase images is, respectively, brighter and darker than the glass substrates as in figures 2.6b and d.....57

Figure 2.8. (a) Images of specific heat for the multilayer graphene flake previously reported in figure. 2.6 and independently obtained at (a) $\omega = 75$ Hz, (b) $\omega = 200$ Hz, and (c) $\omega = 450$ Hz.....58

Figure 2.9: Thermal conductivity maps for three different frequencies, (a) 75 Hz, (b) 200 Hz and (c) 450 Hz. Although the images are slightly different, the thermal conductivity is expected to not depend on the modulation frequency of the pump beam since k_{th} is a material property. The discrepancy in k_{th} may be related to slight drift in pump beam power that sometimes occurs and also on possible contribution from convection. The role of convection is however very limited in NeSTRI because air molecule velocity is ≈ 0 near the sample surface when scanning in out of contact but in close proximity to sample surface59

Figure 3.1: SEM images of graphene-based thin films decorated with Cu-NPs. Cu-NPs were deposited at different sputtering times of 2, 3 and 5 minutes, respectively, and annealed at (a) 300°C, (b) 400°C and (c) 550°C. (d) Variation of the average diameter of Cu-NPs decorated on the graphene samples shown in the SEM images. (e) Fraction of graphene surface covered by Cu-NPs obtained after annealing at different times.69

Figure 3.2: UV-visible transmission spectra of a set of samples at (a) increasing area coverage by Cu-NPs, showing a decrease in transmittance and (b) increasing nanoparticle diameter. The dips at ~ 550 nm are assigned to surface plasmon resonance of Cu-NPs. The transmittance of a bare graphene thin film is also included in both plots as a reference.70

Figure 3.3: (a) AFM and (b) SKPFM micrographs of graphene-based thin film decorated with Cu-NPs. (c) Plot of the work function vs. Cu-NP diameter for Cu-NPs on graphene (d) AFM and (e) SKPFM micrographs of Cu-NPs on ITO. (f) Plot of work function vs. Cu-NP diameter for Cu-NPs on ITO. As AFM tend to overestimate NP diameters, the indicated diameter in (c) and (f) was obtained from the height profile of NP's shown in (a) and (d) and similar images obtained during simultaneous AFM/SKPFM measurements. The different trends for ϕ as a function of the diameter are consistent with the fact that electrons are withdrawn by graphene from Cu-NPs.71

Figure 3.4: Electronic density of state (DOS) calculated for a bare graphene flake of dimensions 80x80 rings (black trace) and graphene covered with 59 Cu-NPs with radius $r = 3a$ distributed randomly (red trace). Panels (a)-(d) illustrate the dependence of the DOS on the modified diagonal and off-diagonal matrix elements. (a) $t_{\text{mod}} = 0.5t_0$, generating shallow states near the Fermi level, (b) $t_{\text{mod}} = 2t_0$, generating deep states symmetrically in the valance and conduction bands. (c) Effect of a positive $\Delta\varepsilon = \varepsilon_{\text{mod}} - \varepsilon_0 = 0.3$ eV on the DOS, generating states in the valence band, and (d) Effect of a negative $\Delta\varepsilon = \varepsilon_{\text{mod}} - \varepsilon_0 = -0.3$ eV, generating states in the conduction band. Both situations c and d are breaking the electron-hole symmetry.75

Figure 3.5: Schematic representation of superlattices of (a) 59 Cu-NPs of $D = 0.85$ nm diameter distributed randomly on a graphene lattice and (b) 1 Cu-NP of $D = 6.5$ nm (both with $f_j = 20\%$) (c) Calculated shift in the work function vs. $\Delta\varepsilon$ for the two distributions in panels a (black trace) and b (red). (d) The density of states for the two distributions indicated in panels a (red) and b (black) assuming $\Delta\varepsilon = 0.3$ eV. (e) and (f) show the DOS for the two distribution at $\Delta\varepsilon = 2$ eV..76

Figure 3.6: (a) Comparison of tight-binding (solid lines) and experimental (dots) trends of the work function of graphene as a function of area coverage by Cu-NPs. (b) Model for Cu-NPs with

contact diameter, d , different from the maximum particle diameter.78

Figure 3.7: (a) Relationship between work function and area coverage fraction and (b) relationship between electrical resistivity and area coverage fraction for a set of graphene films decorated by Cu-NPs at a constant diameter $D \approx 20$ nm. (c) Relationship between work function and electrical conductivity obtained by combining the data in panel a and b, which is excellently reproduced by the Poole-Frenkel model as in eq. (3.5). (d) Example of fit of J-V characteristic in using eq. (3.4). (e) Poole-Frenkel model for detrapping at moderate electric fields of π -electrons localized in the proximity of metallic nanoparticles.81

Figure 4.1: (a) AFM topography of graphene based platelets showing regions (A-E) of the platelets of different thicknesses. (b) The height profiles of regions A, C and E of the graphene-based platelets used to determine layer thicknesses. (c) Histogram of the thicknesses of the different regions of the graphene-based platelets indicated in (a) and (d) The calculated number of layers based on inter-layer thickness of $t = 0.35$ nm. The fact that the platelet has varied layer thicknesses makes it ideal for the present study, allowing to investigate interface performance with Cu-NPs.91

Figure 4.2: AFM topography of (a) bare graphene-based platelets with no Cu-NPs (b) the same graphene-based platelets decorated with Cu-NPs and (c) after etching Cu-NPs in conc. HNO_3 . The SNOM transmittance images of graphene-based platelets (d) without Cu-NPs (e) decorated with Cu-NPs and (f) after Cu-NPs etching. The SNOM reflectance images obtained simultaneously during the NeSTRI measurements on the same graphene-based platelets (g) without Cu-NPs (h) with adsorbed Cu-NPs and (i) after Cu-NPs etching.93

Figure 4.3: Simultaneously measured thermal amplitude and phase images of thermoreflectance oscillation. The amplitude images were measured from the same graphene-based platelets (a) without Cu-NPs (b) decorated with Cu-NPs and (c) after Cu-NPs etching. The phase images are from the same sample (d) without Cu-NPs (e) decorated with Cu-NPs and (f) after Cu-NPs etching.95

Figure 4.4: (a) Changes in thermoreflectance oscillation amplitudes as a function of the number of layers. $\Delta\rho_1$ was obtained from the difference between the amplitude of graphene-based platelets decorated with Cu-NPs and the amplitude of same sample without Cu-NPs. $\Delta\rho_2$ is the difference between the amplitude of graphene-based platelets after Cu-NPs etching and the amplitude of same sample prior to Cu-NPs deposition. (b) The variation of the measured changes in the phase of thermoreflectance oscillation with the number of layers of graphene-based platelets. Differences in phase are measured with respect to value of pure graphene-based platelets.96

Figure 4.5: Variation of thermoreflectance amplitude with Cu-NPs diameter. The change in amplitude with the size of NPs is indicative of possible size effects in lowering interfacial thermal resistance at increasing particles size98

Figure 5.1: The memristor architecture used in this study. Sixteen memristors were simultaneously fabricated by spin coating a 10 nm thick layer of P6OV onto four identical prepatterned cathode electrodes, with four orthogonal anodes on top. The work function of the cathode materials is also indicated.106

Figure 5.2: Current density–voltage (J–V) characteristics of a device showing memory effects, in which the write (V_W), read (V_R), and erase (V_E) voltages are indicated. Arrows along the J–V

curves indicate the scanning direction, starting from $V = 0$. Red open dots correspond to the low-conductivity regime (for $V < 0$ until $V = V_W$ is reached). Black solid dots correspond to the subsequent high-conductivity regime (for $V_W < V < V_E$). The system gradually reverts to the low-conductivity regime at $V = V_E$109

Figure 5.3: (a) P6OV absorbance versus photon energy. An intense absorption band at $E_{\pi\pi^*} = 4.6$ eV is observed, which is assigned to $\pi \rightarrow \pi^*$ interband transitions. Two less intense optical absorption bands at 3.1 ± 0.1 eV are assigned to SOMO \rightarrow LUMO and HOMO \rightarrow SOMO transitions. (b) Diagram of optical transition energies. The neutral SOMO level (0) sits close to mid-gap, which is corroborated by the closeness of SOMO \rightarrow LUMO and HOMO \rightarrow SOMO transition energies $E_{(0),(+,\pi^*)}$ and $E_{(0,\pi),(-)}$ (yellow and red lines in (a)). However, $E_{(0),(+,\pi^*)} + E_{(0,\pi),(-)} > E_{\pi\pi^*}$ due to non-negligibility of the Hubbard energy U in the SOMO level. The SOMO becomes positively charged (+) when losing an electron, actually leading to $(0) \rightarrow (+,\pi^*)$ transitions, and becomes negatively charged (-) when gaining one electron, actually leading to $(0,\pi) \rightarrow (-)$ transitions.111

Figure 5.4: (a) AFM (top) and KPFM (bottom) images of P6OV film and nearby Al contact. (b) Histogram of surface potential obtained from KPFM image in (a). The HOMO energy level of P6OV sits at $\epsilon_{\pi} = 6.2 \pm 0.2$ eV below the vacuum level as shown in Figure 5.3b. 114

Figure 5.5: Current density versus voltage characteristics of P6OV thin films as a function of the cathode material in a) high-conductivity and b) low-conductivity regime. Output currents are strongly dependent on the work function of the cathode material. c) High-conductivity and low-conductivity current densities of Al/Ca-P6OV-FLG devices, showing ohmic and Poole-Frenkel behavior in the high and low conductivity regimes, respectively. d) Poole-Frenkel model at moderate electric fields, which leads to hopping in the low-conductivity regime.116

Figure 5.6: Energy band diagram of P6OV-based memristors demonstrating optimized charge transport in (a) low-conductivity and (b) high-conductivity regime. Energy bands in different memristor components are shown. Optimal charge injection in the low-conductivity regime occurs at 4.0 eV for electrons transferred to P6OV from the Al cathode. These electrons hop from monomer to monomer in a Poole-Frenkel transport mechanism (bottom left). In the high-conductivity regime, optimal hole injection occurs at 4.7 eV, when the cathode work function matches the $\epsilon_{(+)}$ level of P6OV, and optimal electron injection occurs at 3.1 eV, when the anode work function matches the $\epsilon_{(-)}$ level of P6OV. Simultaneous optimization of injection of electrons and holes is necessary to maximize extended state charge transport in the high-conductivity regime (bottom right).118

Figure 5.7: Measured output current (top curves) and corresponding applied voltages (red bottom curves) during multiple write–read–erase–read cycles of P6OV-based memristors with different cathode materials: (a) ITO (b) FLG (c) Al, and (d) Ca/Al. High-conductivity and low-conductivity states read at $V_R = +1.0$ V are indicated by black dashed lines, from which the on/off current ratios can be inferred. The work function of the cathode (e.g. FLG and ITO) needs to be 4.5-4.7 eV, comparable to the energy level $\epsilon_{(+)}$ of the positively charged polyradical, in order to produce stable on/off ratios and ensure flash effects. Cathode work functions of the order of $\epsilon_{(0)} \approx 4$ eV, the energy level of the neutral SOMO of P6OV, produce WORM effects, e.g. with Al. No memory effects were observed with symmetric Ca/Al & Al/Ca electrodes....122

Figure 5.8: (a) On/off current ratio vs. device cathode surface potential. A high surface potential of the cathodes matching the positive charge state of P6OV are critical for high performance of the devices as shown in the optimized Al/Ca-P6OV-ITO memristor. (b) Current response (top

curve) and corresponding applied voltage (bottom curve) obtained during the stability test of Al/Ca-P6OV-ITO memristor under constant write-read-erase-read voltage cycles. High on/off current ratios $\sim 10^2$ at 1.0 V reading voltage were achieved in the optimized device, with high reproducibility over several tens cycles of write-read-erase-read.....124

Figure 6.1: Variation of the thickness of P6OV films with the spin coating speed. P6OV was deposited on bare glass substrate for thickness optimization.132

Figure 6.2: Optical images of graphene thin films deposited from different filtration volumes of (a) 5 ml (b) 20 ml, (c) 30 ml and (d) 40 ml. The optical images were processed using image J, an image processing package to obtain the fraction of the substrates covered by the graphene platelets. (e) Variation of graphene area fraction with the filtration volume.134

Figure 6.3: AFM topography of P6OV/graphene composites from different area coverage of graphene of (a) 0.20, (b) 0.46, (c) 0.53 and (d) 0.68135

Figure 6.4: Optical transmittance of graphene thin films and P6OV/graphene nanocomposites measured in the wavelength range $\lambda = 380 - 500$ nm. This wavelength range was specifically selected to cover the previously observed SOMO-LUMO optical absorption peak in P6OV. The fraction of covered area is indicated on the right of the color code.137

Figure 6.5: Change in transmittance, ΔT of graphene thin films without and with P6OV as a function of fraction, f of graphene covered area. ΔT was determined at the wavelength $\lambda = 400$ nm in which P6OV show significantly higher absorption due to SOMO \rightarrow LUMO and HOMO \rightarrow SOMO transitions.138

Figure 6.6: Current – voltage characteristics of graphene thin films and P6OV/graphene nanocomposites for different fraction of graphene covered area of (a) 0.2, (b) 0.46, (c) 0.53 and (d) 0.68.140

Figure 6.7: The conceptual representation of percolation of graphene-based platelets on the glass substrate - (a) about graphene percolation threshold, $f \leq f_0$, the films are mostly insulating and (b) above the threshold f_0 , the platelets form continuous conducting pathway along the substrate surface and the films have high electrical conductivity141

Figure 6.8: (a) Electrical conductivity (K_{el}) as function of the fraction, f of surface area covered by graphene platelets for graphene-based thin films (open dots) and P6OV/graphene nanocomposites (solid dots). Solid lines represent simulation of experimental data according to eq. 6.1. Restructuring of P6OV in a graphene-based film into three regions of (b) below graphene percolation threshold, in which P6OV forms a continuous layer embedding sparse graphene-based platelets, (c) about graphene percolation threshold, in which P6OV tends to aggregate and does not affect the electrical conductivity of the film and (d) quite above graphene percolation threshold, in which P6OV tends to isolate the graphene-based platelets, playing a detrimental role to the electrical conductivity.142

Figure 6.9: AFM topography (a, b), SNOM transmission (c, d) and (e) SNOM reflection images (e, f) of P6OV/graphene nanocomposites comprising of graphene platelet with $f = 0.46$ (top images; a, c, e) and $f = 0.53$ (bottom images; b, d, f). The topography was obtained simultaneously during SNOM measurements.144

Figure 6.10: (a) Mirror image of graphene platelets indicated by rectangular box in Fig. 6.9(c) and (b) heat profile image of P6OV/graphene nanocomposite. Large amount of heat is generated in the correspondence of graphene platelet that can be attributed to more absorption of pump beam146

Figure 6.11: Thermal amplitude (a, b) and Phase (c, d) of P6OV/graphene nanocomposites, comprising of graphene platelet with $f = 0.46$ (top images; a, c) and $f = 0.53$ (bottom images; b, d). These images were obtained during the NeSTRI scan at a pump beam modulation frequency of 105 Hz.148

List of Appendices

Appendix A: Complementary Images to Chapter 2	158
Appendix B: Copyright permissions	161

List of Symbols, Variables and Abbreviations

A. List of symbols and variables

β	Pool-Frenkel coefficient
ϵ_m	Dielectric permittivity relative to vacuum
$\epsilon_{(+)}$	Energy level of positive charge state of P6OV relative to vacuum level
$\epsilon_{(0)}$	Energy level of neutral charge state of P6OV relative to vacuum level
$\epsilon_{(-)}$	Energy level of negative charge state of P6OV relative to the vacuum level
$\epsilon_{(\pi)}$	HOMO of P6OV relative to the vacuum level
$\epsilon_{(\pi^*)}$	LUMO of P6OV relative to the vacuum level
σ	Electrical conductivity
σ_0	Polymer conductivity in the absence of traps
τ	Transmittance of the sample recorded by SNOM
ρ	Reflectance of the sample recorded by SNOM
$\delta\rho$	Amplitude periodic thermoreflectance oscillations
$\delta\varphi_0$	Phase of periodic thermoreflectance oscillations
Φ_{sample}	Work function of sample
Φ_{tip}	Work function of AFM tip
ω	Angular frequency
ω_0	AFM tip resonance frequency
A_0	Absorbance
C	Heat capacity
D	Thickness of absorbing film in NeSTRI experiment
$E_{\pi\pi^*}$	HOMO– LUMO energy band gap
H	Heating profile locally generated in the sample by the pump beam

H_0	Amount of heat locally deposited per sample unit volume
k	Thermal conductivity
k_B	Boltzmann Constant
K_{el}	Sheet electrical conductivity
P_0	Laser power
q	Elementary charge
q^*	Dynamic effective charge of trapped carriers
T	Local temperature difference between sample surface and the environment
U	Hubbard Interaction Energy
V_{CPD}	Local contact potential difference between AFM tip and sample surface

B. List of abbreviations

AFM	Atomic force microscope
Cu-NP's	Copper nanoparticles
CV	Cyclic voltammetry
CW	Continuous wave
DOS	Electronic density of state
FLG	Few layer graphene
F_j	Fraction of covered area
HOMO	Highest occupied molecular orbital (π -bonding)
ITO	Indium–tin oxide
KPFM	Kelvin probe force microscopy
LUMO	Lowest unoccupied molecular orbital (π^* -antibonding)
N	Number of graphene layers
NeSTRI	Near field scanning thermorefectance imaging

ORP	Organic radical polymers
P6OV	poly-[1,5-diisopropyl-3-(cis-5-norbornene-exo-2,3-dicarboxiimide)-6-oxoverdazyl]
RF	Radio frequency
RNA	Ribonucleic acid
ROMP	Ring-opening metathesis polymerization
SEM	Scanning electron microscope
SMA	Subminiature accessory
SNOM	Scanning near field optical microscopy
SOMO	Singly occupied molecular orbital
SThM	Scanning thermal microscopy
UHV	Ultrahigh vacuum
V_E	Erase voltage
V_R	Read voltage
V_W	Write voltage
WORM	Write-once-read-many times

Chapter 1

Thin film materials used in this thesis and their characterization methods

My thesis is about developing and utilizing specific scanning probe techniques to understand the properties of ultrathin film materials at the nanoscale level, with special emphasis on their electronic structure and thermophysical properties. We developed a system to image the thermal properties of ultrathin film materials at sub-micron resolution and we also prepared specific thin film materials for which this type of characterization is relevant. Among the thin films investigated in this work, we have extensively utilized graphene-based thin films, with a number of nanoscale modifications, including their functionalization with copper nanoparticles. We studied the influence of metal nanoparticles on the electronic and thermal properties of graphene-based thin films. Other thin film materials investigated in this thesis include oxoverdazyl-based organic polyradicals to demonstrate the design criteria for achieving ultrathin memory devices, graphene-copper nanoparticles and graphene – polymer nanocomposites. This chapter offers a general overview of the materials and the associated properties will be discussed in the following sections, as well as the characterization techniques adopted to study the properties of these materials.

1.1. Objectives and background

With the increasing miniaturization and development of electronic devices and concurrent increase of processing power, heat generation and nanoscale heat propagation in integrated chips and other optical and electronic components is becoming increasingly important. Consequently, nanoscale imaging of electronic and thermal properties should be equally developing. Efficient

thermal management at nanoscale is of both scientific and industrial interest and requires fabrication of components from materials with high thermal conductivity. Materials that are being developed to this end are both nano-structured [1, 2] and heterogeneous, and include composites [3], bilayers [4] and multilayers [5]. Thermal properties of these nanomaterials are expected to be strongly dependent on the microscopic thermal properties of interfaces and grain boundaries [6]. Interfacial thermal resistance, a well-known macroscopic phenomenon, is expected to also occur at nanoscale level when nanomaterials are produced for the purpose of heat evacuation from devices. Therefore, development of specific investigative techniques for studying nanoscale thermal properties is absolutely essential.

Some methods for measuring thermal conductivity at the nanoscale have already been developed. Scanning Thermal Microscopy (SThM) [7, 8] is a technique which utilizes self-heated thermal sensors, constructed from atomic force microscopy (AFM) tips, in contact with the studied sample to determine the thermal properties of materials at nanoscale. However, interfacial thermal resistance, weak thermal coupling between the sensor and the sample, as well as fluctuations of this coupling due to nanoscale features of sample geometry significantly reduce the performance of SThM in nanoscale thermal measurements. In order to overcome these problems, researchers have been developing modulated thermoreflectance technique [9, 10] as contactless method of choice for thin film thermal conductivity measurements. While the modulated thermoreflectance method is well suited for thermal imaging of materials with negligible interfacial effects, the technique is however limited by diffraction and therefore is inadequate to discriminate between different materials when used for imaging nanoscale objects.

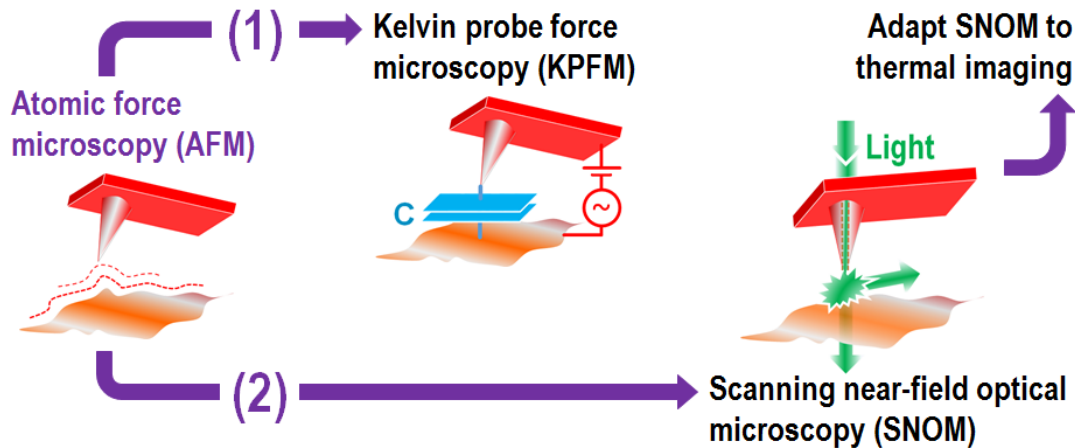


Figure 1.1: Scheme of the characterization apparatus utilized for nanoscale investigation of surface electronic and thermal properties of specific ultrathin materials and devices studied in this thesis. Kelvin probe force microscopy (KPFM), an atomic force microscopy (AFM) – based technique is used for nanoscale mapping surface electronic properties. Scanning near-field optical microscopy (SNOM) is adapted and modified for thermal imaging.

In this thesis, we developed a new nanoscale imaging technique based on modulated thermoreflectance method using atomic force microscopy coupled scanning near field microscopy (SNOM) system. This is intended to combine the best attributes of SThM (nanoscale imaging capability) and thermoreflectance (contactless) techniques in a single thermal imaging procedure that overcome the diffraction limits inherent in thermoreflectance method. **Figure 1.1** gives the scheme of the characterization apparatuses utilized in our new thermal imaging technique, which relies on the operation of atomic force microscopy. The spatial resolution of AFM is expected to be high enough to enable nanoscale imaging of surface electronic properties of ultrathin film materials using Kelvin probe force microscopy (KPFM) as we describe in details in the following sections. Our newly developed high-resolution modulated

thermoreflectance imaging enables precise detection of photo-induced effects on sample surface. This new thermal imaging technique, which is built on existing SNOM system is described in details in chapter two of this thesis.

1.2 Characterization techniques used in this work

1.2.1 Atomic force and scanning near field optical microscope

Atomic force microscope system consists of probes, laser diode, four quadrant detector, feedback loop and piezoelectric scanner [14]. For controlling the different parts and for collation of data, the AFM is interfaced with a desktop computer, which also provides means of controlling the modes of operation of the system. As shown in **Figure 1.2**, three modes of AFM operations can be identified which differ mainly by the amount of the interaction force between an AFM tip and sample surface [12]. When the AFM tip is within a few angstroms from sample surface, non-negligible repulsive force appears between the tip and the sample due to the overlap of electronic orbitals at atomic distances. The repulsive force increases and becomes stronger as the tip gets closer to the sample as shown in Figure 1.2. In this regime, the tip is assumed to be in contact with the sample surface. For imaging surface morphology of solid samples, such as those reported in this thesis, AFM contact mode can be utilized to produce good quality topography images of samples. High quality optical images using SNOM can also be achieved using contact mode configuration. However, in specific measurement conditions where tip-sample interaction force is to be minimized, imaging in a non-contact configuration can be carried out by lifting the tip up a few microns from sample surface. As we explain in more details in chapter two, this measurement condition is required to overcome the thermal sinking problems inherent in SThM due to tip-sample contact [13] On the other hand, operation in

tapping mode is based on a feedback mechanism of constant oscillation amplitude with the tip – surface force defined in the region shown in Figure 1.2. This is the ideal configuration for KPFM operation in amplitude modulation.

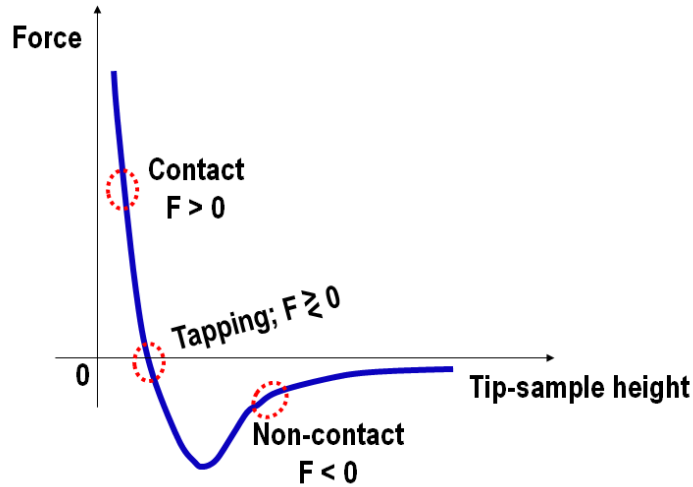


Figure 1.2: Atomic interaction forces between the AFM tip and the sample surface, which define the modes of AFM operation into contact, non-contact and tapping modes.

Nanoscale investigation and materials characterization presented in this thesis was carried out using an AFM customized for aperture-type scanning near field optical microscopy measurements. A Witec Alpha 300S AFM/SNOM system available in Fanchini's group laboratory in the Department of Physics and Astronomy at Western University was used in our work. This system can be used to investigate a variety of samples because of its flexibility to perform a wide range of imaging and spectroscopic experiments based on AFM, SNOM, confocal imaging and electrostatic and capacitive force microscopies [14]. A schematic of the Witec Alpha 300S system is shown **Figure 1.3**, together with a magnified view of the parts dedicated to SNOM measurement. During normal operation, the system is sensitive to mechanical vibrations, electromagnetic waves as well as acoustic noise. In order to minimize the

effects of the noise, the system which is contained in an anti-damping box with an air-pressured based and aluminum foil protection is placed on an optical table, a passive anti-vibration table during all of the measurements.

In this thesis, we will use our Witec Alpha 300S system both in AFM and AFM/SNOM operation modes, for specific characterization techniques. AFM/SNOM allow simultaneous topographic and near field optical imaging of our samples for the purpose of obtaining relevant information as we discuss them in the following section. In the next sections, we will describe SNOM operation more in detail and we will show how the system can be integrated with Kelvin probe force microscopy accessories that allow nanoscale investigation of electronic properties of graphene thin films decorated with copper nanoparticles.

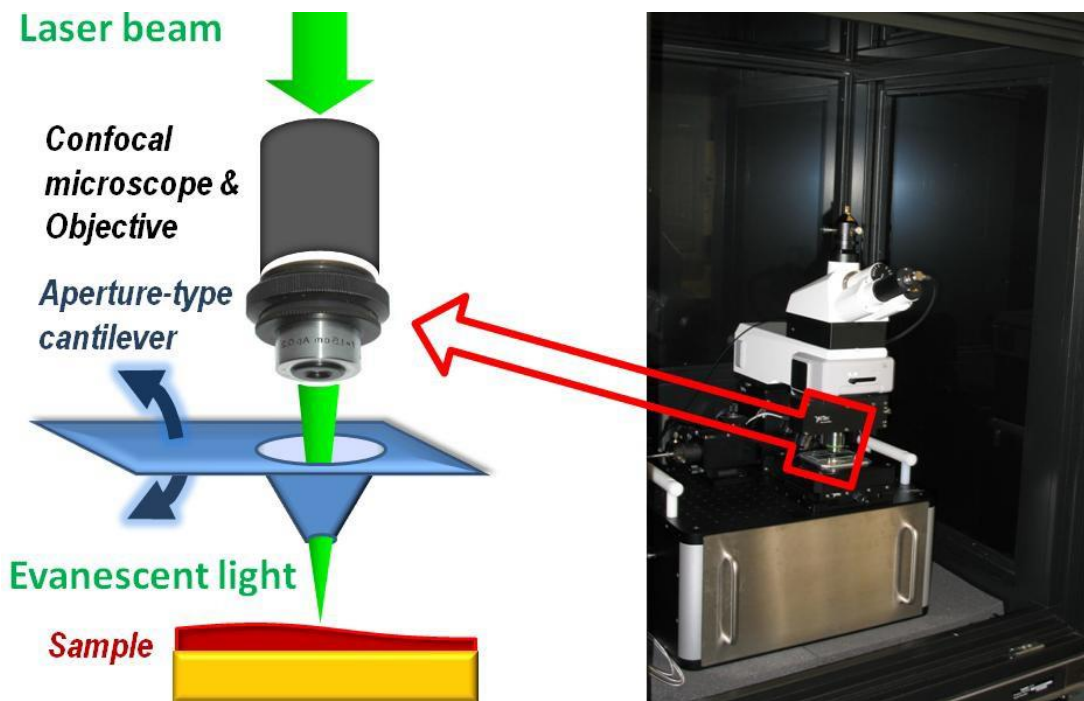


Figure 1.3: Schematic of the Witec Alpha 300S atomic force microscope (right) used in this work [15]. On the left is a magnified image of a confocal microscope and hollow AFM cantilever that permit near field optical imaging of the studied sample.

1.2.2 Scanning near field optical microscopy operation

SNOM is a nano-optical imaging technique that exploits light–matter interaction for the purpose of extracting relevant information about nanoscale objects. It is used to overcome the diffraction limit inherent in conventional optical microscopes [14]. To achieve subwavelength spatial resolution, SNOM uses evanescent wave generated or scattered in the proximity of a nano-object to probe other nano-objects, such as graphene-based thin films or copper nanoparticles studied in this thesis. For this reason, SNOM is classified based on the type of the probe generating the evanescent waves into apertureless SNOM and aperture-type SNOM [14]. In the case of apertureless SNOM used in this thesis, evanescent light scattered from nano-hole of diameter, $d \sim 80 \pm 10$ nm is used as the probe to achieve high spatial resolution during all of our measurements. **Figure 1.4** shows the position of evanescent waves which resides in the near field at the position much less than the wavelength of light. The scattered wave region comprised of propagating component of the wave at distances of the order of the wavelength of light.

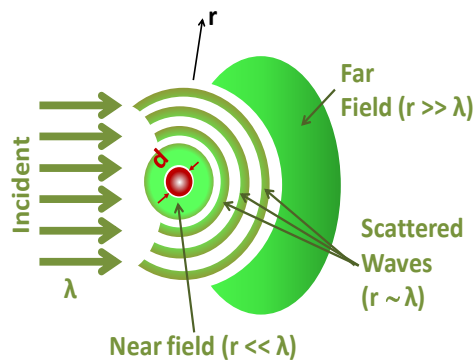


Figure 1.4: Far field and near field obtained when incident probe light is scattered from nano-hole of diameter, d machined at the end of an atomic force microscope cantilever. Scattered wave is observed at distances that are of the order of the wavelength of the light. (Figure courtesy of ref. 14)

With our AFM/SNOM system, light from a laser is directed, by a system of optical fibers, into a high-resolution confocal optical microscope that focuses the laser light inside a nanohole ($d \approx 80$ nm) machined at the end of an atomic force microscope cantilever depicted schematically in **Figure 1.5**. The sample is positioned on a $100 \times 100 \mu\text{m}$ piezo-scanner that has a maximum excursion of $10 \mu\text{m}$ in the z -direction. Sample scan can be done in contact, noncontact and tapping mode similar to normal operation of AFM [14], thus allowing for easy recording SNOM images and, simultaneously, AFM topographic images of a sample. In addition, the mechanical arm on which the confocal microscope is mounted can also be moved in z -direction for optimizing the focal plane at the level of the AFM hollow tip.

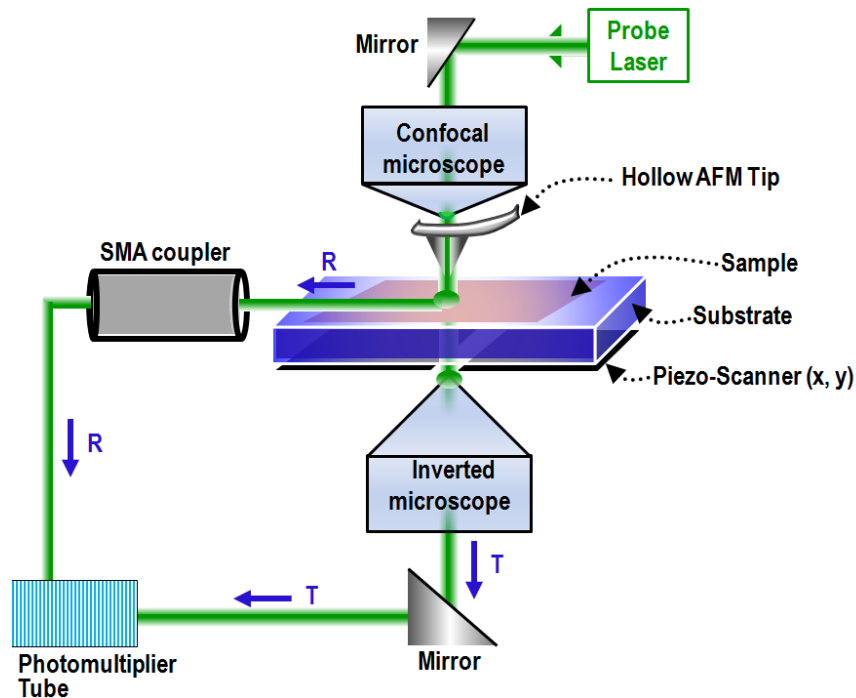


Figure 1.5: Schematic of AFM/SNOM system showing the collection of probe laser light for operation in transmission and reflection modes.

As shown in Figure 1.5, the system can record SNOM images in ‘transmission mode’ and in ‘reflection mode’ (indicated respectively with the letter ‘T’ and ‘R’ in this figure) that differs

in the way the laser light is collected after interaction with the sample. In transmission mode operation, an inverted microscope below the sample stage is used to collect the light transmitted through the sample. The transmitted light is subsequently launched into an optical fiber that is connected to a photomultiplier tube (U-68000, Hamamatsu) operating in photon-counting mode. In the case of the reflection mode operation also described in **Figure 1.5**, evanescent waves locally generated at the tip aperture, and scattered by the sample are subsequently collected at grazing angle by a subminiature accessory (SMA, Witec). In our SNOM mode operation, the sample surface can be scanned along the (x, y) plane at $z = \text{constant}$, in order to obtain relevant information about the amount of light scattered or transmitted through a sample at a nonzero distance from its surface. With this optical imaging procedure, we designed a thermal imaging technique to study the thermal properties of low dimensional materials at nanoscale as we describe in details in the following chapter.

1.2.3 Atomic force microscopy/Scanning Kelvin Probe force microscopy system

Kelvin probe force microscopy (KPFM), is a technique based on a scanning probe cantilever, which allows for the measurement of local surface potential difference between a reference metallic electrode at known work function and the sample surface [16]. If this technique is coupled with AFM, in a way that the reference electrode is a conducting scanning probe cantilever, the local surface potential difference at the contact between the tip and the sample can be mapped with high spatial resolution and thereby the work function of a sample.

In this thesis, the Witec Alpha 300S atomic force microscope was used in a particular configuration that was previously modified for surface potential and work function imaging. [16]. The integrated Kelvin-probe force accessory includes an AC generator, a stabilized direct

current (DC) voltage supply, a lock-in amplifier (Stanford Research Co.) and a proportional-integral-differential feedback control loop. The system is interfaced with a desktop computer for controlling the different parts and, for collating data. The schematic diagram of this system is shown in **Figure 1.6**, for which the laser beam is used primarily for the surface topography map [14].

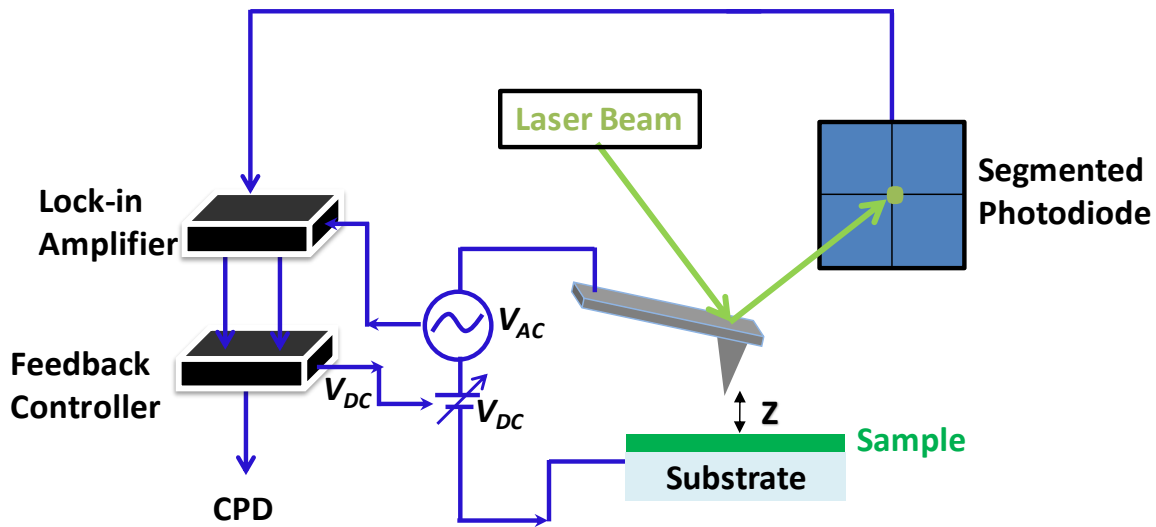


Figure 1.6: Schematic diagram of Kelvin Probe Force Microscopy. A lock in amplifier used at the second resonance frequency of the cantilever is operated in amplitude modulation mode. In this mode, the tip-sample electrostatic force is measured directly from the amplitude of the cantilever using a lock-in amplifier referenced to the AC potential signal by a function generator.

The functionality of SKPFM is based on small electrostatic forces that are created between the conducting AFM tip and the sample when the two systems are in close proximity of the order of few microns. During the operation of KPFM, the local contact potential difference V_{CPD} between the tip and the sample surface can be expressed as [17]:

$$q \cdot V_{CPD} = \varphi_{tip} - \varphi_{sample}, \quad (1.5)$$

where $q = 1.6 \times 10^{-19}$ C is the elementary charge and φ_{tip} and φ_{sample} indicate the work functions of the tip and the sample, respectively. Hence the right hand side of eq.1.5 corresponds to the difference between the Fermi levels within the two systems. For our KPFM experiments, a platinum-coated AFM tip with $\omega_0 \approx 75$ kHz resonance frequency (Nano Sensors Inc.) was used.

The tip-sample electrostatic force F can be expressed as a function of the energy accumulated inside the capacitor formed by these two objects (that is, tip and sample) as a function of their separation Z [17]:

$$F = \frac{dE}{dZ} = \frac{1}{2}(\Delta V)^2 \frac{dC}{dZ}. \quad (1.6)$$

In eq. 1.6, E indicates the electrostatic energy and C is the capacitance of the tip-sample system, with the two objects kept at a potential difference ΔV . To measure the contact potential difference indicated in eq. 1.5, a nullifying voltage V_{DC} is applied between the tip and the sample in conjunction with a small modulating AC signal, $V_{AC} \cdot \sin(\omega_2 t)$, which oscillates at the second-order resonance frequency of the tip, $\omega_2 \approx 4\omega_0$. The total voltage,

$$\Delta V = (V_{DC} - V_{CPD}) + V_{AC} \cdot \sin(\omega_2 t), \quad (1.7)$$

consists of DC and AC components. By substituting eq. 1.7 into eq. 1.6, we obtain the following expression for the force between the tip and the sample:

$$F = \frac{1}{2} \cdot \frac{dC}{dZ} (\Delta\phi)^2 + \frac{1}{4} V_{AC}^2 + \frac{dC}{dZ} (\Delta\phi) \cdot V_{AC} \cdot \sin(\omega_2 t) - \frac{1}{4} \frac{dC}{dZ} V_{AC}^2 \cos(2\omega_2 t), \quad (1.8)$$

where $\Delta\phi = q \cdot (V_{DC} - V_{CPD})$. In eq. 1.8, the first term is a DC component and the second and third terms are AC components at angular frequencies ω_2 and $2\omega_2$, respectively. Eq. 1.8 indicates that F is proportional to $\Delta\phi$. Consequently, the value of the nullifying voltage that minimizes the

measured tip-sample force corresponds, at each point of our scan, to the Fermi energy difference between the two objects, from which the work function of the sample can be determined upon tip calibration.

1.2.3.1 Tip calibration and work function determination

In order to determine the absolute work function of a sample, the AFM/KPFM tip is calibrated using a material whose work function is known. Specifically, KPFM measurement was performed on p-type and n-type silicon. Their work functions are respectively, $\varphi_{\text{Si-p}} = 4.52$ eV and $\varphi_{\text{Si-n}} = 3.41$ eV [19]. From the relation, $\Delta\varphi = \varphi_{\text{tip}} - \varphi_{\text{sample}}$ the work function of the tip can be extract by substituting the φ_{sample} with the work functions of the silicon-based samples. Consequently, if the work function of the tip is known, either directly from knowledge of work function of the coating material, or indirectly from the work function of the silicon substrate which acts as reference, the work function of a sample can be determined via eq. 1.7. Both methods, direct and indirect, yield the same result in our case, with uncertainties of ± 0.05 eV or less.

1.3 Materials used in this thesis

1.3.1 Graphene and graphene-based thin films

Graphene is two-dimensional (2D) solid with a honeycomb structured lattice comprising a single layer carbon atoms [19]. It is two-dimensional, and therefore the building block of three-dimensional graphite through the stacking of many layers of graphene. These stacks are held together by weak van der Waals forces. **Figure 1.7** shows the schematic of carbon atoms arranged in a honeycomb lattice forming $N = 1$ layer of graphene and $N \sim \infty$ in graphite. Since its

discovery [20], graphene has attracted much attention in both academia as well as industry due to its many remarkable properties [21-22]. For instance, room temperature thermal conductivity value for single layer graphene can be as high as $5000 \text{ W m}^{-1}\text{K}^{-1}$, in addition to high optical transparency in near UV and the visible [1]. Graphene also exhibits high mechanical strength, extraordinary electrical properties and good flexibility, making it excellent material for use in flexible electronics. One outstanding electrical property of graphene is its mobility, with $\mu \sim 200,000 \text{ cm}^2/(\text{V}\cdot\text{s})$ at low temperature [23]. This value is substantially more than the mobility of electrons in Si, which at room temperature is about $1400 \text{ cm}^2/(\text{V}\cdot\text{s})$ [24] and that of carbon nanotubes, with $\mu \sim 100,000 \text{ cm}^2/(\text{V}\cdot\text{s})$ at room temperature [25]. Hence, free standing graphene has the highest carrier mobility among all semiconductor materials. Because of this and other remarkable properties there are increasing and compelling need to graphene for a diverse array of application.

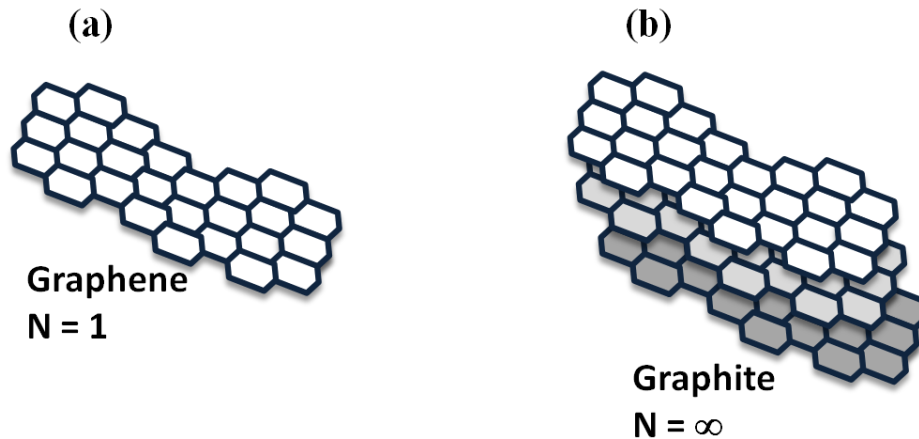


Figure 1.7: The schematic structure of (a) graphene and (b) graphite. Graphene is one atom thick planar sheet while graphite consists of stacked layers ($N \sim \infty$) of graphene weakly bonded by van der Waals forces.

Despite the above fascinating properties, the fabrication and manipulation of single-layer nanosheets represents an uphill challenge and limits extensive applications of graphene in devices. Some of the methods in use for fabricating single- and few-layer graphene includes chemical vapor deposition on metal foils [26], epitaxial growth [27] and plasma enhanced chemical vapor deposition [28]. These fabrication methods are well established and can be used to produce single- and few layer graphene. However, the methods rely on specialized equipment with high energy requirements, thus making it difficult for scalability and mass production at low cost. The fabrication of graphene and graphene-based materials at low cost is essential in order to enhance its competitiveness with the existing Si technology which has dominated electronic industries for a very long time.

Over the past couple of years, research on graphene and graphene-based materials has increased significantly because of new and low cost methods to produce and study graphene-based platelets, comprising of few- and many-layers [29-34]. The procedure, which is based on graphene grown via liquid phase exfoliation method, includes spin coating, spray coating, drop casting and vacuum filtration techniques [21]. While these techniques are generally accessible to many researchers due to the simplicity and low cost, the use of vacuum filtration affords a more controlled set-up for reproducibility. Moreover, the production of graphene dispersion used for graphene thin film fabrication in these methods is achieved via controlled surfactants-assisted solution processing of exfoliated graphite [35]. The use of ribonucleic acid (RNA) as a non-ionic surfactant to exfoliate few layer graphene flakes [29] has recently been employed for fabricating large-area thin films of contiguous, multi-domain graphene. Once exfoliated and vacuum filtrated unto a sacrificial membrane, graphene flakes can be transferred to diverse substrates, thus making the method versatile for many applications, processability on plastics substrates and

high scalability. In the following section we will describe the solution growth technique adopted for the fabrication of graphene-based thin films studied in this thesis.

1.3.1.1 Preparation of graphene-based thin films

Transparent and conducting graphene-based thin films used at various stages of our work were prepared using the vacuum filtration method. This method was originally invented by Wu et al. [36] for single wall carbon nanotubes and later adapted by Eda et al. [32] for graphene oxide fabrication. Sharifi et al. [29] further developed the method for surfactant exfoliated thin films based on few-layer graphene platelets. The fabrication steps leading to the deposition of graphene thin films on the desired substrate is shown in **Figure 1.8**. Graphite powder (Aldrich, 332461) and Ribonucleic acid (RNA) are used as the starting materials for this fabrication process and to obtain graphene-based suspensions in water. RNA promotes graphite exfoliation and also helps to stabilize the exfoliated graphene and few layer graphene flakes against re-aggregation, a major problem with most frequently used surfactants such as sodium dodecylbenzene sulfonate [37].

In order to be exfoliated and produce few-layer graphene platelets, graphite was ultrasonicated for 24 h in a 3:1 $\text{H}_2\text{SO}_4:\text{HNO}_3$ mixture, then mildly oxidized in Piranha reagent ($\text{H}_2\text{SO}_4:\text{H}_2\text{O}_2 = 4:1$) and subsequently dried prior to further use. Due to the very low degree of oxidation, this process yields material that is significantly less oxidized than “reduced” graphene oxide commonly prepared using the Hummers' or similar methods [21,32,38]. 6 mg of the resulting material were suspended for 4 h in a 0.6 g/L aqueous solution of RNA extracted from *torula utilis* (Aldrich) which acts as a non-ionic surfactant and promotes graphite exfoliation [29]. The slurry was left to sediment overnight at 2°C in a beaker. The top three-quarters of the beaker content were then centrifuged at 6000 rpm for 1 hour and the supernatant, largely

consisting of well dispersed single- and few-layer graphene flakes, was collected and used for graphene-based thin-film deposition.

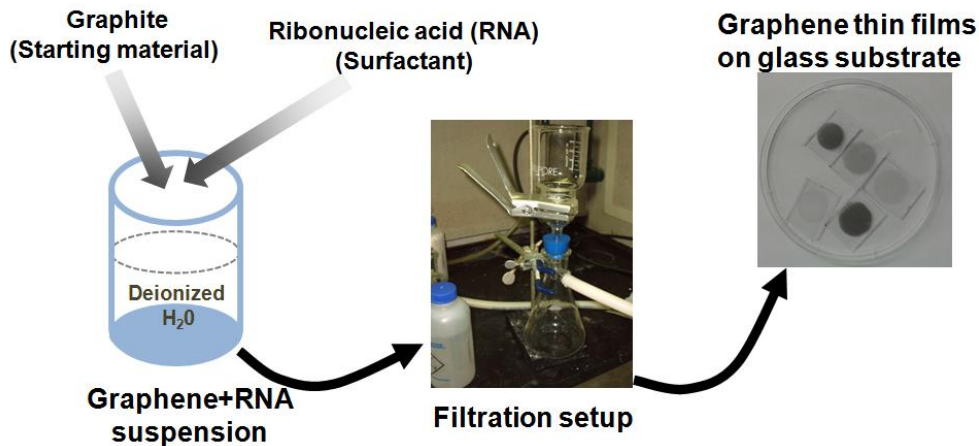


Figure 1.8: Preparation steps for the fabrication of graphene thin films. Graphene is prepared in solution based on exfoliation of graphite using RNA as surfactant. The resultant graphene layer in solution is vacuum-filtrated on a membrane and subsequently transferred on desired substrate. The middle image is the picture of filtration setup in Fanchini's group laboratory in the Department of Physics and Astronomy at Western University. The last image is the picture of graphene thin films on glass substrate of different thicknesses obtained from different filtration volumes of graphene/RNA suspension.

The thin-film deposition, which is the last part of the fabrication process, consists of the following steps. 5 ml of water suspension of graphene flakes and RNA were filtrated through a 220-nm pore size sacrificial membrane (Millipore). Small amounts of diluted suspensions are used to prevent re-aggregation of the suspended flakes during deposition on the filtration membrane. Membranes loaded with graphene flakes are subsequently transferred to the requisite substrates, and dried in a vacuum desiccator. The sacrificial membrane is then etched using acetone baths in petri dishes, thus obtaining random distributions of graphene domains on their

substrate. A final methanol bath is used to remove the last traces of the membrane. The samples are annealed at 550 °C for 4 hours to remove RNA and, also, completely reduce them. This fabrication procedure yields graphene-based thin films very similar to those being currently investigated for several large-area applications in electronics and sustainable energy [39] and, therefore, offers a realistic benchmark for fundamental studies. Specifically, their electronic and thermal properties were investigated to determine the doping mechanisms and the effect on thermal conductivity of Cu-NP's depending on NP diameter and the number of layers of graphene.

1.3.2 Organic Polyradicals (OPR)

As the need for higher conductivity, better stability and greater processability of conducting polymers increases, more attention has been given to stable organic radical polymers (ORP). These are special class of functional macromolecular materials in which the pendant side groups consist of stable organic radicals. Some of their properties, including electronic, optical, magnetic, etc stem from the weakly interacting unpaired electrons of the radical monomers. The structural disparity of ORP manifests itself in the number of atomic centres bearing the unpaired electrons in the polymer, so that we can have diradicals, triradicals, tetraradicals, and even higher radicals [40]. Ployradicals, which is the subject of this section, consist of a polymer backbone with many stable organic radical side groups. Due to these side groups, polyradicals contains many atomic centres with unpaired electrons that can influence their properties by acting as trap centres.

Figure 1.9 shows a possible classification of organic polyradicals according to Ref. 41, into nitrogen-centered radicals, carbon-centered radicals, nitroxide-based radicals and oxygen-

centered radicals. Among these groups, divalent nitrogen-centered verdazyl radicals are of particular importance because of their stability. Stability in the context used here implies that the polyradical can be isolated, manipulated and stored as a pure compound [42, 43].

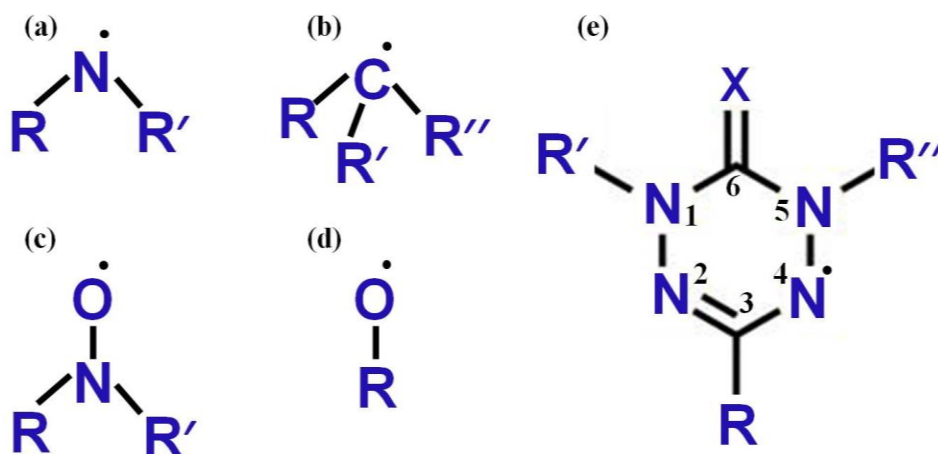


Figure 1.9: Classification of organic radicals based on the atom centres into (a) nitrogen-centred radicals, (b) carbon-centred radicals, (c) nitroxide based and (d) oxygen-centred radicals [41]. The dot on each atomic centre represents a singly-occupied electronic orbital (e) The general structure of verdazyl radicals. A family of verdazyl based polyradicals are developed by replacing the X group with atoms or groups such as carbonyl group or thiocarbonyl group.

The chemical stability in this group of polymers is achieved through delocalization of the unpaired electrons across the nitrogen atoms of the cyclic hydrazyl structure [41]. Because of their stability, verdazyl radicals are now considered one of the larger families of stable radicals. Their general chemical structure shown in panel (e) of **Figure 1.9** consists only of phenyl ring (C_6H_5) at the R, R' and R'' sites. The X group in this figure is generally different for different

categories of verdazyl-based radical polymers, such as ‘Kuhn verdazyls with a saturated carbon at C6 (R-C6-R’), thiocarbonyl containing verdazyle (S=C6) and oxoverdazyl polyradicals that contains a carbonyl group (O=C6) at the C6 ring. In this thesis, the functionality of stable oxoverdazyl based polyradical will be demonstrated through their application in memory devices.

1.3.2.1 Synthesis of stable organic radical polymers

Much effort has been put into synthesis of stable ORP [44-46] with the aim of enhancing their functionalities. Some of the synthetic procedures for ORPs include a wide range of polymerization techniques such as free radical polymerization, [46] Ring-opening metathesis polymerization (ROMP), [45,47] olefin metathesis polymerization, [48] selective polymerization [49] and ionic polymerization [50]. Ring-opening metathesis polymerization represents an ideal method for the synthesis of ORPs because it can be used to synthesize stable radical polymers with high degree of radical content along the polymer backbone [47]. In the last decades, the utility of ROMP has expanded significantly because of the development of new and well-defined catalysts that allow for control over molar mass and architecture in the resultant polymers [51].

1.3.2.2 Preparation of poly-[1,5-diisopropyl-3-(cis-5-norbornene-exo-2,3-dicarboxiimide)-6-oxoverdazyl]

ROMP was used to synthesis poly-[1,5-diisopropyl-3-(cis-5-norbornene-exo-2,3-dicarboxiimide)-6-oxoverdazyl] (P6OV), the nitrogen-centred poly-radical used in our thesis. The synthesis was carried out by Gilroy’s group in the Department of Chemistry at Western University. The preparation process of P6OV can be divided into sequential synthesis steps, which are shown schematically in **Figure 1.10**. First, a white microcrystalline powder of 1,5-di-

isopropyl-3-(4-carboxyphenyl)-6-oxotetrazane (or simply tetrazane) is synthesized by slow condensation reaction in which a solution of 4-carboxybenzaldehyde (1.21 g, 8.09 mmol) and sodium acetate (0.66 g, 8.1 mmol) in methanol (50 mL) was added drop wise to a refluxing solution of 2,4-di-isopropylcarbazide (2.00 g, 8.09 mmol) and sodium acetate (1.33 g, 16.2 mmol), also in methanol (50 mL) [47].

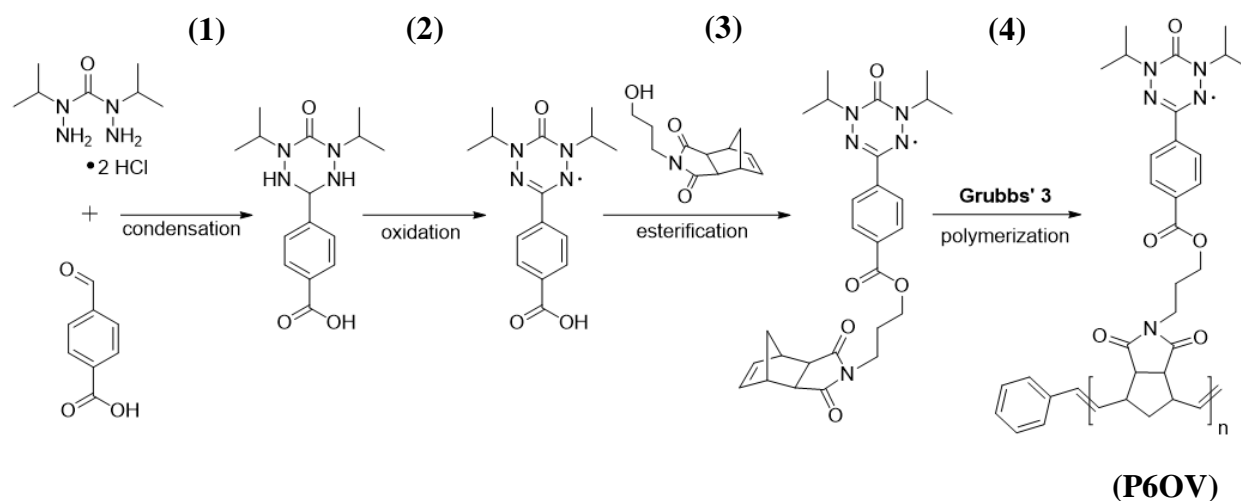


Figure 1.10: Synthesis steps for the production of poly-[1,5-diisopropyl-3-(cis-5-norbornene-exo-2,3-dicarboxiimide)-6-oxoverdazyl] – polymer 13 (P6OV), the polyradical used in this thesis work for the fabrication of organic memory device. The synthesis steps consist of (1) condensation, (2) oxidation, (3) esterification and (4) polymerization reactions. Figure courtesy of Ref. 52.

The second step of the preparation involves the production of verdazyl using tetrazane as the starting materials. The reaction mixture is composed of deionised H₂O:tetrahydrofuran (2:1, 45 mL), tetrazane (2.34 g, 7.64 mmol) and sodium hydroxide (0.31 g, 7.6 mmol) in which solution of sodium periodate (2.45 g, 11.5 mmol) is added drop wise for a period of about 30

minutes. This oxidation reaction produces dark-red precipitate of 1,5-Di-isopropyl-3-(4-Carboxyphenyl)-6-Oxoverdazyl (verdazyl) upon reduction of the pH level to ~ 3 with the addition of 1 M hydrochloric acid and subsequent removal of tetrahydrofuran (CH₂)₄O in vacuo. In order to synthesize 1,5-diisopropyl-3-(cis-5-Norbornene-exo-2,3,- dicarboxiimide)-6-oxoverdazyl, a solution of N,N'-dicyclohexylcarbodiimide (DCC) (0.75 g, 3.6 mmol) and 4-dimethylaminopyridine (DMAP) (0.48 g, 4.0 mmol) in dry dichloromethane (CH₂Cl₂) (20 mL) was added verdazyl (1.00 g, 3.30 mmol) before the mixture was stirred for 10 min at room temperature. To this solution was added N-(3-hydroxypropyl)-cis-5- norbornene-exo-2,3-dicarboximide 11 (0.73 g, 3.3 mmol) and a further 10 mL of dry CH₂Cl₂ (for rinsing). Room temperature stirring and further purification by column chromatography yielded about 51.18 g of Oxoverdazyl [31].

The final preparation step involves direct polymerization of the radical monomers to produce a stable polyradical. The reaction is initiated with the 6-oxoverdazyl monomer in a Schlenk flask, which is treated with 8.73 ml of Grubbs' third generation catalyst, a transition metal carbene complexes, dissolved in dichloromethane. The polymerization reaction continues for about 1 hour before using ethyl vinyl ether to controllably terminate the reaction. After purification in THF and cold hexane, the resulting polymer with the structure shown in right most part of **Figure 1.10** is an orange powder of poly-[1,5-diisopropyl-3-(cis-5-norbornene-exo-2,3-dicarboxiimide)-6-oxoverdazyl] (P6OV). This radical polymer dissolves easily in a variety of different solvents including chlorobenzene and toluene. As a result the polymer can readily be formed into smooth thin films from solution through spin coating onto requisite substrate. This is ideal condition for application of materials, especially polymeric materials in devices and were

utilized for the fabrication of memory device in which P6OV is the active memory element and will be presented in chapter 5 of this thesis.

1.3.2.3 Application of organic polyradicals in memory devices

Electronic memristors can be classified into volatile and non-volatile depending on whether the memory element requires a constant supply of power to retain the stored information. Volatile memory devices lose the stored information if it is not provided with a constant power supply or refreshed periodically with a pulse [53]. Conversely, non-volatile memory can provide the means to write and retain information long after the power to write them is switched off. Among these types of electronic memory, write-once-read-many times (WORM) memory are the most widely reported polymer memory devices in the literature [54-55]. Although no power is needed to maintain the information stored in WORM memory, its usage is limited by the inability to erase, reprogram or rewrite its stored information. Another example of non-volatile memory is the flash. Flash memory has attracted much attention, because not only that no power is needed to maintain the information stored in flash memory but also has additional advantage that the stored data can be erased and rewritten many times. Despite these benefits, there are only few reports demonstrating flash effect with ORP. In chapter five of this thesis, we will show that efficient design architecture and better understanding of the mechanism of operation are necessary for the integration of radical polymer into flash memory.

Even prior to our thesis, stable ORPs have been explored as potential active materials in resistive memory devices (memristors) for data storage and data-driven computation [56, 57]. There are also many instances in which organic and other polymeric materials have featured as memory elements in devices [58-59]. Different from silicon, the polymeric materials have the advantages of easy processability, scalability, low-cost potential and capability of 3D stacking

[53]. ORP based memory devices has additional advantage of simplicity and miniaturization of device structure through the use of ultrathin active memory element [56]. The mechanical flexibility of these materials makes them compatible with plastic substrates for lightweight and flexible device design. Thus, ORP offers the possibility of realizing nanoscale data storage which will lead to increased density of data memory, fast speed, low power consumption and lightweight [54]. As a result, ORP are targeted as possible substitute for silicon-based conventional memory devices in which stability and reliability are a big challenge as the thickness of the memory elements are reduced to below 22 nm [53].

The organic and polymer electronic memristors store data through the triggering of their electrical conductivity between high and low conductivity states when an external voltage source is applied to it. This property, known as electrical bistability, is different from conventional silicon-based memory device, in which data are stored based on the amount of charge accumulated in the memory cells [53]. **Figure 1.11** shows typical I-V characteristics of ORP based memristor. The figure represents the I-V characteristics of a device that was initially in a high resistance state, which subsequently was tuned into high conductivity state (line /AEBC/ in Figure 1.11) when a negative voltage larger than threshold voltage (V_{write}) is applied to the electrodes. At this threshold voltage, large output current can be observed in the I-V curved as indicated by line /AE/ in the figure. However, a positive voltage larger than another threshold voltage (V_{erase}) switches the device back to low conductivity state (line /CDE/ in Figure 1.11). The device state is not affected if the applied bias is within the threshold voltage, V_{read} , enabling the low-voltage read process. In this way, ORP based-memristors can provide the means for storing and accessing binary digital data sequences of “1’s” and “0’s” through the functionality

of their electrical bistability. The Boolean “1” and “0” are activated when the device is respectively in high and low conductivity state.

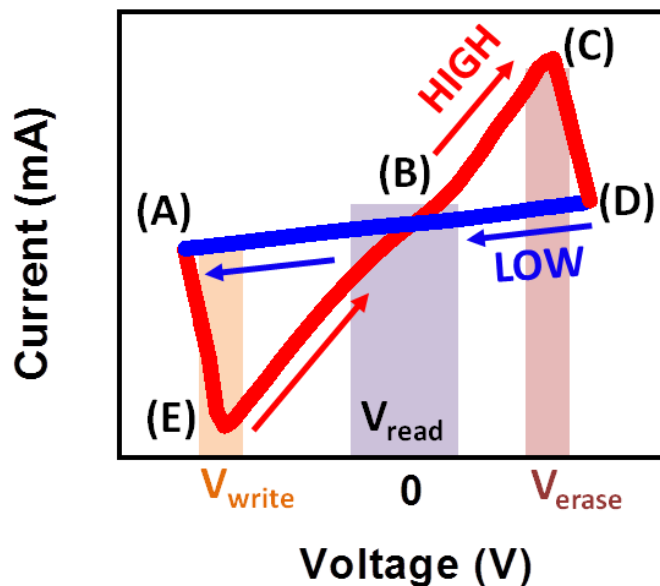


Figure 1.11: Resistive switching in a typical radical polymer based memory device. The device which was initially in a low conductivity state (/DA/) is activated to high conductivity state at the threshold voltage, V_{write} . The high conductivity state persists during a positive biasing (/AEBC/) until another threshold voltage, V_{erase} which returns the device to low conductivity state. The voltage range at which no transition occurs, V_{read} , can be used to read and understand the state of the device.

The most optimal architecture for exploiting these memory effects is the sandwich configuration [47, 56]. This configuration allows for the memory effect to be activated through the electrical bi-stability of the radical polymeric thin films in response to the applied electric field. The fabrication of the device consists in spin coating of the active memory element, the polyradicals on the bottom electrode, followed by thermal evaporation of the top electrodes in an ultrahigh vacuum chamber. In this way, ORP thin films are interposed between the bottom and

top electrodes so that the area covered by the two electrodes forms the active device area. The most widely used electrode materials are aluminum, gold, copper, p- or n-doped silicon, few-layer graphene thin films and indium thin oxide. The choice of one electrode over the other can be made based on the surface potential of the electrodes [56]. Wrong choice of electrode materials may constitute a potential barrier that can substantially affect the operation of the device by restricting the transfer of charges from the radical polymer to the electrodes. In chapter five of this thesis, we will show that the choice of the electrode materials can change the operation of the radical polymer-based memory device from flash to WORM.

1.4 Electrical transport in polymer materials

In this section, we will briefly examine the effect of electric fields on the electrical transport properties of polymer films. In particular, we will discuss the transport mechanisms associated with free carrier and hopping conduction in polymers. Carrier hopping and drifting of free carriers through polymer filament are the two main transport processes that, respectively, characterize the low and high conductivity states of the polyradical studied in chapter five of this thesis. These processes can be aptly discussed using the Poole-Frenkel and Ohmic models.

1.4.1 Poole Frankel transport

A prominent theory of electric field dependent conduction mechanism which is applicable to polymers is the Poole-Frenkel transport model [60, 61]. This transport mechanism became important in polymers due to the effects of trap levels in polymer conductivity. It has been suggested that traps can be caused by a variety of factors, including the presence of radicals in a polymeric material [61]. For a polyradical which is the subject of chapters 5 and 6 of this thesis,

the traps produce localized states in each monomer of the polymer that can be positively charged when empty or neutral when filled [47, 56]. In this situation, Coloumbic barrier results when electrons interact with the positively charged states. The lowering of the barrier by the external electric field, \mathbf{E} leads to Pool-Frenkel field-dependent conductivity, generally expressed as [52]:

$$\sigma = \sigma_0 \exp\left[\frac{\beta E^{1/2}}{2k_B T}\right] \quad (1.1)$$

Where σ_0 is the steady state equilibrium conductivity in the absence of an applied electric field, $\beta = (q^3 / \pi \epsilon_0 \epsilon_r)^{1/2}$ is the Pool-Frenkel coefficient, q is the elementary charge and $k_B T = 0.025$ eV at room temperature.

Figure 1.12 is a typical I-V curve of a Pool-Frenkel type electrical transport that can be obtained in a highly insulating polymeric thin film under low external field. To better understand the I-V characteristic of insulating polymers of this type, we can reformulate the Poole-Frenkel model as follow. Starting with eq. 1.1, which gives conductivity in terms of the applied electric field, and substituting for the conductivity, $\sigma = (I/A).E$, the electric field, $E = V/d$ and expanding the Pool-Frenkel coefficient gives the expected Poole-Frenkel expression in terms of current density ($J = \sigma.E$) and the electric field E [47]:

$$J = \sigma_0 E \exp\left[\frac{-q^* \Delta\varphi + q^{*3/2} \pi^{-1/2} (E / \epsilon_m)^{1/2}}{k_B T}\right] \quad (1.2)$$

where σ_0 corresponds to the polymer conductivity in the absence of traps, q^* is the dynamic effective charge of trapped carriers, ϵ_m is the dielectric permittivity of the polymer relative to vacuum and $k_B T = 0.025$ eV in our case for room temperature.

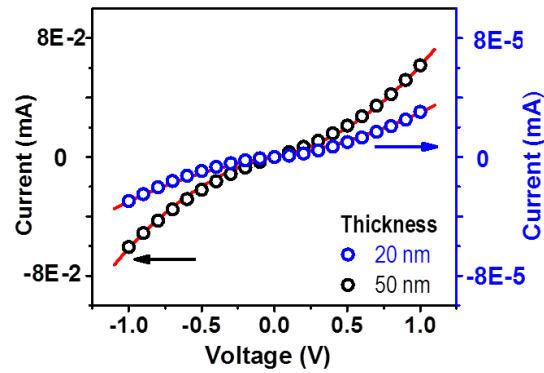


Figure 1.12 (a) I-V curves of highly insulating polymer thin film showing non-ohmic, Poole-Frenkel-like behavior [47]. The polymer used in ref. 30 is poly-[1,5-diisopropyl-3-(cis-5-norbornene-exo-2,3-dicarboxiimide)-6-oxoverdazyl]. (Figure is reprinted from “Synthesis, Characterization, and Thin-Film Properties of 6-Oxoverdazyl Polymers Prepared by Ring-Opening Metathesis Polymerization”, A. Paquette, S. Ezugwu, V. Yadav, G. Fanchini and J. B. Gilroy; *J. Polym. Sci. Part A: Polym. Chem.*, 2016, 54, 1803, Copyright (2016), John Wiley and Sons [47].)

Poole-Frenkel-like transport mechanism observed in Figure 1.12 for polymeric thin films sandwiched between two metallic electrodes is assigned to hopping between localized states situated at specific charged monomers along a polymer filament [47]. The hopping conditions may be strongly dependent on the degree of alignment of the polymer filaments along the substrate, as previously observed in polythiophenes [62]. If all of the polymer chains are aligned parallel to the substrate, hopping along the z-direction must occur through localized states situated on different polymer chains. This consideration may account to why the thinner films, presumably containing polymer filaments more aligned along the substrate, are also more electrically insulating as we observe in Figure 1.12. In chapter 5 of this thesis, we will show that Poole-Frenkel model describe accurately the low conductivity state of memristor fabricated from thin polyradical films.

1.4.2 Ohmic transport processes

Ohmic processes are found in metals, heavily doped semiconductors and even polymer materials at very low applied field. In Ohmic processes, the electrical current flowing through a solid is determined by the carrier drift velocity, which is independent of the applied electric field and determines the electrical conductivity, σ , a material property independent of the geometry of the material. Therefore, in first Ohm's law the electrical current density J is linear in the applied electric field:

$$J = \sigma E, \quad (1.3)$$

A polymer based device which gives approximately linear current – voltage characteristics as shown in **Figure 1.13** is known as ohmic, and can be accurately described by ohmic model (eq. 1.1). The film resistivity (ρ) can be inferred from the I-V characteristics through the relationship,

$$\rho = \frac{R \cdot A}{t}, \quad (1.4)$$

where A is the area of the region in which the top and bottom electrodes overlap and t is the film thickness. Accordingly, a reduction in the film's thickness will lead to a decrease in the resistance of the film at constant A since ρ in an ohmic system is an inherent property of the material, independent of the thickness of the thin film that is being considered [47]. With thicker films, the measured output current will decrease significantly as shown in Figure 1.13.

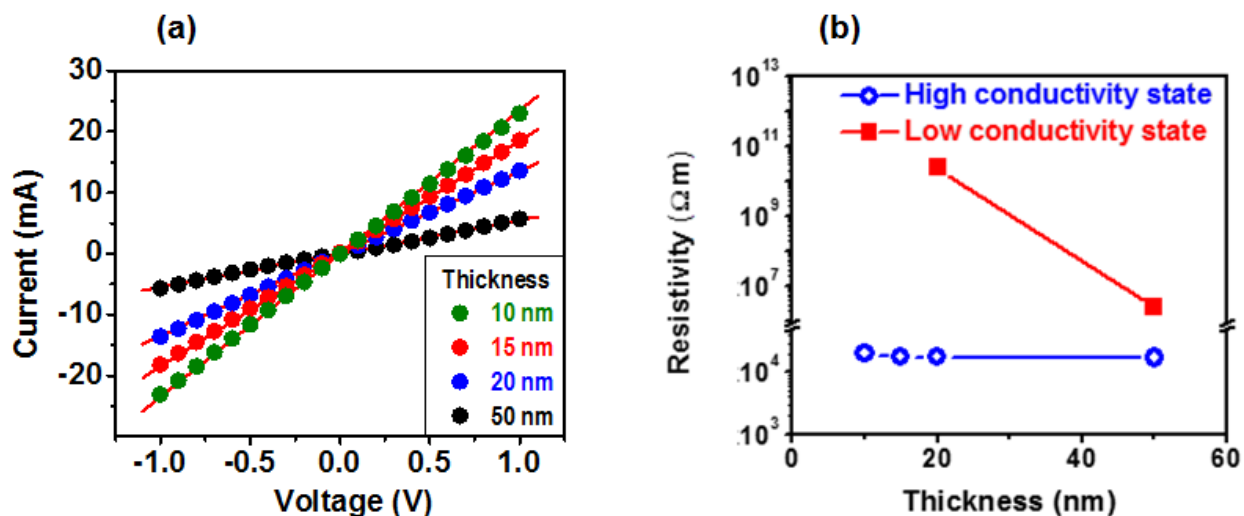


Figure 1.13: (a) The current – voltage curves of a polymer-based thin films at four different thicknesses in high conductivity state, which were fitted with straight lines to demonstrate ohmic transport [47]. (b) Film resistivity values obtained from the low-voltage portions of I-V curves. Resistivity is thickness-independent in the high conductivity state, while it dramatically increases at decreasing thickness in the low-conductivity state, possibly due to preferential alignment of polymer filaments along the substrate. (Figure is reprinted from “Synthesis, Characterization, and Thin-Film Properties of 6-Oxoverdazyl Polymers Prepared by Ring-Opening Metathesis Polymerization”, A. Paquette, S. Ezugwu, V. Yadav, G. Fanchini and J. B. Gilroy; *J. Polym. Sci. Part A: Polym. Chem.*, 2016, 54, 1803, Copyright (2016), John Wiley and Sons [47].)

1.5 Conclusions

In this introductory section, we gave a general overview of the materials studied in this thesis which includes graphene-based thin films and oxoverdazyl-based organic polyradicals. We presented the fabrication procedure for our graphene-based thin films and showed that our solution processed graphene-based thin films is versatile enough for many applications. In chapter 1, we will study in details, the thermal properties of these graphene-based thin films

using a measurement technique, NeSTRI developed specifically in this thesis. In chapter 4 and 6, we will present, respectively the result of our NeSTRI measurements on graphene-based thin films decorated with copper nanoparticles and graphene/polymer composites. In chapter 3, we will present the results of our study: the influence of metal nanoparticles on the electronic properties of graphene-based thin films and in chapter 5, we will demonstrate the design criteria for ultrathin memristors based on organic polyradicals

References

- [1] A. A. Balandin, *Nature Materials* **2011**, 10, 569
- [2] H. Kim, I. Kim, H. J. Choi, W. Kim, *Appl. Phys. Lett.* **2010**, 96, 233106
- [3] M. J. Biercuk, M. C. Llaguno, M. Radosavljevic, J. K. Hyun, A. T. Johnson, *Appl. Phys. Lett.*, **2002**, 80, 15
- [4] R. M. Costescu, D. G. Cahill, F. H. Fabreguette, Z. A. Sechrist, S. M. George, *Science* **2004**, 303, 989
- [5] V. Rawat, Y. K. Koh, D. G. Cahill, T. D. Sands, *J. Appl. Phys.* **2009**, 105, 024909
- [6] A. Chernatynskiy, D. R. Clarke, S. R. Phillpot, Thermal Transport in Nanostructured Materials in Handbook of Nanoscience, Engineering, and Technology
- [7] A. Majumdar, *Annu. Rev. Mater. Sci.* **1999**, 29, 505
- [8] L. Shi, S. Plyasunov, A. Bachtold, P.L. McEuen, A. Majumdar, *Appl. Phys. Lett.* **2000**, 77, 4295
- [9] A. J. Schmidt, R. Cheaito, M. Chiesa, *Rev. of Sci. Instrum.* **2009**, 80, 94901
- [10] W.J. Parker, R.J. Jenkins, C.P. Butler, G.L. Abbot. *J. Appl. Phys.* **1964**, 32, 1679

- [11] G. Langer, J. Hartmann, M. Reichling, *Rev. Sci. Instrum.* **1997**, 68(3), 1510
- [12] G. Binnig, C.F. Quate, C. Gerber, *Phys Rev Lett* **1986**, 56, 930
- [13] Cahill and Goodson, *J. Heat Transfer* **2002**, 124, 223
- [14] S. Ezugwu, Synthesis and Characterization of Copper Nanoparticles and Copper-polymer Nanocomposites for Plasmonic Photovoltaic Applications, MSc Thesis, Univ. of Western Ontario, London ON Canada, 2012. See also, <http://ir.lib.uwo.ca/etd/1025>.
- [15] Web resource: <http://www.physics.uwo.ca/~gfanchin/equipment.shtml>, accessed on September 12, 2016
- [16] F. Sharifi, *Kelvin Probe Force Microscopy on Graphene Thin Films for Solar Cell and Biosensing Applications*, PhD Thesis, Univ. of Western Ontario, London ON Canada, **2014**, <http://ir.lib.uwo.ca/etd>.
- [17] J. Park, D. Bang, K. Jang, S. Haam, J. Yang, S. Na, *Nanotechnology* **2012**, 23, 365705
- [18] A. Novikov, *Solid-State Electronics*, **2010**, 54(1), 8
- [19] A. A. K. Geim. The rise of graphene. *Nature materials*, **2007**, 6(3), 183
- [20] K. S. Novoselov, A.K. Geim, S.V. Morozov, et al. *Science* **2004**, 306
- [21] R. Bauld, F. Sharifi, G. Fanchini, *IJMPB*, **2012**, 26, 1242004.
- [22] A. H. Castro Neto, N. M. R. Peres, K. S. Novoselov, A. K. Geim, *Rev. Mod. Phys.* **2009**, 81, 109
- [23] K.I. Bolotin, K.J. Sikesb, Z. Jiang, M. Klima, G. Fudenberg, J. Hone, P. Kim, H.L. Stormer, *Solid State Communications*, **2008**, 146, 351
- [24] F. Stern, *Phys. Rev. Lett*, **1980**, 44(22), 1469

- [25] T. Dulrkop, S. A. Getty, E. Cobas, M. S. Fuhrer, *Nano Lett.*, **2004**, 4(1), 35
- [26] X. Li, Y. Zhu, W. Cai, M. Borysiak, B. Han, D. Chen, R. D. Piner, L. Colombo, R. S. Ruoff, *Nano Lett.*, **2009**, 9, 4359
- [27] P. W. Sutter, J. Flege, E. A. Sutter, *Nat. Materials*, **2008**, 7, 406.
- [28] A. Dato, V. Radmilovic, Z. Lee, J. Phillips, M. Frenklach, *Nano Lett.*, **2008**, 8, 2012
- [29] F. Sharifi, R. Bauld, M. S. Ahmed and G. Fanchini, *Small*, **2012**, 8, 699.
- [30] M. Kato, K. Uki, S. Harako, X. Zhao, *Microelectronic Engineering*, **2014**, 121, 96
- [31] J. S. Park, S. M. Cho, W. J. Kim, J. Park, P. J. Yoo, *ACS Appl. Mater. Interfaces*, **2011**, 3, 360
- [32] G. Eda, G. Fanchini, M. Chhowalla. *Nature Nano* **2008**, 3, 270
- [33] X. Lin, P. Liu, Y. Wei, Q. Li, J. Wang, Y. Wu, C. Feng, L. Zhang, S. Fan, K. Jiang, *Nat. Commun.*, **2013**, 4, 2920.
- [34] F. Pashaei, F. Sharifi, G. Fanchini, F. Lagugne-Labarthet, *Phys. Chem. Chem. Phys.*, **2015**, 17, 21315.
- [35] A. Yu, P. Ramesh, M. E. Itkis, E. Bekyarova, R. C. Haddon, *J. Phys. Chem. C*, **2007**, 111, 7565
- [36] Z. Wu, Z. Chen, X. Du, J.M. Logan, J. Sippel, M. Nikolou, K. Kamaras, J. R. Reynolds, D. B. Tanner, A. F. Hebard, A. G. Rinzler, *Science* **2004**, 305, 1273.
- [37] M. S. Ahmed, S. Ezugwu, R. Divigalpitiya, G. Fanchini. *Carbon*, **2013**, 61, 595
- [38] S. Pei, H.M. Cheng, *Carbon*, **2012**, 50, 3210
- [39] J. Park, D. Bang, K. Jang, S. Haam, J. Yang, S. Na, *Nanotechnology* **2012**, 23, 365705

- [40] A. Rajca, *Chem. Rev.* **1994**, 94, 871
- [41] K. Zhang, M. Monteiro, Z. Jia, *Polym. Chem.*, 2016, DOI: 10.1039/C6PY00996D
- [42] J. B. Gilroy, *The Design, Synthesis, and Chemistry of Stable Verdazyl Radicals and Their Precursors*, PhD thesis, University of Victoria, British Columbia, Canada, **2003**
- [43] R. G. Hicks, *Verdazyls and Related Radicals Containing the Hydrazyl [R₂N-NR] group*, in *Stable Radicals, Fundamental and Applied Aspects of Odd-Electron Compounds*, Edited by Robin G. Hicks. **2010**, John Wiley & Sons Ltd.
- [44] T. Sukegawa, H. Omata, I. Masuko, K. Oyaizu, H. Nishide, *ACS Macro Lett.* **2014**, 3, 240
- [45] T. Jahnert, B. Haupler, T. Janoschka, M. D. Hager, U. S. Schubert, *Macromol. Rapid Commun.*, **2014**, 35, 882
- [46] T. Janoschka, A. Teichler, A. Krieg, M. D. Hager, U. S. Schubert, *J. Polym. Sci. Part A: Polym. Chem.* **2012**, 50, 1394
- [47] J. A. Paquette, S. Ezugwu, V. Yadav, G. Fanchini, J. B. Gilroy, *J. Polym. Sci. Part A: Polym. Chem.*, **2016**, 54, 1803
- [48] P. Nesvadba, L. Bugnon, P. Maire, P. Novak, *Chem. Mater.* **2009**, 22, 783
- [49] T. Ibe, R. B. Frings, A. Lachowicz, S. Kyo, H. Nishide, *Chem. Commun.* **2010**, 46, 3475
- [50] M. Suguro, S. Iwasa, Y. Kusachi, Y. Morioka, K. Nakahara, *Macromol. Rapid Commun.* **2007**, 28, 1929

- [51] S. Sutthasupa, M. Shiotsuki, F. Sanda, *Polymer Journal*, **2010**, 42, 905
- [52] Dr. Joseph A. Paquette, private communication
- [53] B. Zhang, Y. Chen, K. G. Neoh, E. Kang, *Electrical Memory Materials and Devices* in RSC Polymer Chemistry Series No. 18, Edited by Wen-Chang Chen. The Royal Society of Chemistry **2016**
- [54] S. Moller, C. Perlov, W. Jackson, C. Taussig, S.R. Forrest, *Nature* **2003**, 426, 166
- [55] A.D. Yu, T. Kurosawa, Y.C. Lai, T. Higashihara, M. Ueda, C.L. Liu, W.C. Chen, *J. Mater. Chem.* **2012**, 22, 20754
- [56] S. Ezugwu, J. A. Paquette, V. Yadav, J. B. Gilroy, G. Fanchini, *Advanced Electronic Materials*, **2016**, DOI: 10.1002/aelm.201600253
- [57] J. Lee, E. Lee, S. Kim, G. S. Bang, D. A. Shultz, R. D. Schmidt, M. D. E. Forbes, H. Lee, *Angew. Chem. Int. Ed.* **2011**, 50, 4414
- [58] R. G. Hicks, *Nat. Chem.* **2011**, 3, 189
- [59] A. Bandyopadhyay, A. J. Pal, *Adv. Mater.* **2003**, 15, 1949
- [60] L. A. Dissado, J. C. Fothergill, *Electrical Degradation and Breakdown in Polymers*, IEE Materials and Devices Series 9, Edited by G.C. Stevens, Peter Peregrinus Ltd, **1992**, London UK. pp 207-223
- [61] J. G. Simmons, *Physical Review*, **1967**, 3, 55
- [62] A. M. Nardes, M. Kemerink, R. A. J. Janssen, J. A. M. Bastiaansen, N. M. M. Kiggen, B. M. W. Langeveld, A. J. J. M. van Breemen, M. M. de Kok. *Adv. Mater.* **2007**, 19, 1196

Chapter 2

Nanoscale Thermal Imaging of Graphene-based Thin Films

2.1 Scanning Near-Field Thermoreflectance Imaging

2.1.1 Existing thermal imaging techniques

Submicrometric devices for next generation information technology require very large scale component integration and high power density. To evacuate extremely high heat loads locally generated within these devices, it is essential to fabricate and characterize thin heat spreaders at high performance [1]. Understanding heat evacuation in thin films and low dimensional systems is vital to design heat spreaders for efficient thermal management in next-generation information technology [1]. Despite such a vast demand, experimental techniques capable of imaging thermal conductivity at the high lateral resolution demanded by state-of-the art electronic components, pose a tremendous challenge to both academia and industry. Most of the methods used to determine the thermal conductivity of thin solid films, including the 3- ω method, [2] laser flash techniques [3] and others, [4, 5] are macroscopic in nature and average the thermal properties over large areas. They are unable to recognize the local fluctuations in sample composition and in the local variations of the thermal properties at the nanoscale.

To date, nanoscale thermal measurements mostly rely on scanning thermal microscopy (SThM), [6–13] a family of contact-mode scanning probe microscopy techniques that utilize thermal sensors integrated with cantilever probes. In SThM architectures that have been proposed to date, either the cantilever acts as the thermal sensor and simultaneously as a heat generator, [8,12] or the heat generated by electrical

current flowing through the scanning probe cantilever and the sample is detected by local thermometers based on infrared spectroscopy, [13] thermoelectric effects [7,9] or a combination of these methods. Unfortunately, in all these cases, relatively voluminous scanning probe cantilevers are required to be in contact with the sample. The measuring probe acts as an important thermal sink and the strong coupling between the probe and the sample cannot be neglected. Significant interfacial thermal resistivity also affects SThM measurements.

Thermal sinks and interfacial thermal resistivity effects associated to SThM probes are largely irreproducible due to the irreproducibility of the distance and thermal contact between the probe and the sample, an issue that is particularly problematic in samples with nanoscale roughness. In an effort to improve the thermal contacts, SThM measurements in which the cantilever is immersed in a fluid have been attempted [11]. However, fundamental studies have shown that a solid-liquid interface also constitutes a large thermal barrier [14,15]. Subsequently, liquid-immersion SThM is unlikely to mitigate many of the thermal sink issues commonly associated with SThM techniques. Different approaches are required to overcome the constraints of SThM.

Modulated thermorefectance [16-20] is a contactless technique commonly used to determine the thermal conductivity of solids, but is macroscopic in nature. With this technique, the sample is periodically heated at the surface, and heat transfers to air, or another fluid at the interface, which experiences periodic changes in density and refractive index due to the subsequent periodic oscillations in temperature. The phase lag at which changes in the fluid refractive index occur depends on the thermal properties of the sample, which can thus be measured by means of a light beam. The use of light

eliminates the necessity of physical contact between the sample and the probe. Thermoreflectance measurements are contactless and alleviate many of the thermal sinking problems commonly associated with other contact-based thermal measurements. Micro-thermoreflectance was used to accurately map the thermal properties of micrometer-thick gold films [20]. However, differently from SThM, this technique suffers from inherent limitations in terms of lateral resolution. Light, the thermal probe used in thermoreflectance measurements, is limited by diffraction in its capability to characterize nanometer size objects. Optical methods that are not diffraction-limited and combine the advantages of SThM and thermoreflectance will be vital to enable contactless thermal imaging at the nanoscale.

2.1.2 A new thermal imaging technique

Scanning near-field optical microscopes (SNOM) are optical instruments that exploit the properties of evanescent waves generated by scattering of light in the proximity of a nanostructured sample to enable sub-wavelength resolution beyond the diffraction limit [21]. SNOM measurements rely on the interaction of two distinct nanometer-size objects: a nanoscale feature in the illuminated sample and a nanometer-size probe. Apertureless SNOM utilizes nanoparticles as probes, while nanometer-size openings are used to detect the optical signal in aperture-type SNOM. With modern aperture-type instruments, the near-field optical signal is generated and detected by hollow scanning probe cantilevers and the sample topography is simultaneously scanned by atomic force microscopy (AFM). If visible light is used for SNOM experiments, the sample-probe distance can be extended up to several ten nanometers during optical

measurements, [22] thus enabling SNOM imaging in non-contact mode, with negligible mechanical and thermal interaction between the cantilever and the sample.

In this chapter, we demonstrate that an aperture-type SNOM system operating out of contact with the sample can be utilized to detect modulated thermorefectance signals from a nanostructured thin film, thus enabling contactless thermal imaging with nanoscale resolution. Due to the combination of SThM and thermo-reflectance methods, the technique we are here introducing for the first time can be termed near-field scanning thermorefectance imaging (NeSTRI). The NeSTRI apparatus implemented in this thesis will include two distinct microscopes from which specimen under investigation can be illuminated: an inverted optical microscope from which the sample can be uniformly irradiated and heated by an intense time-modulated “pump” laser, and an upright, aperture-type SNOM microscope, from which the surface irradiated from the inverted microscope can be scanned at sub-wavelength resolution by a low-intensity “probe” laser beam at different wavelength. In addition of illuminating the sample with the probe laser beam, the SNOM system will be used to collect the pump laser light that traverses the sample and to measure its intensity. In this way, the optical absorption coefficient of the sample can be locally determined. The SNOM instrument is complemented by a grazing-angle detector to collect and quantify the amount of “probe” laser light reflected by the sample. From the periodic modulation of the reflectivity of the probe beam, and its phase delay with respect to the modulation of the pump beam, the amplitude and phase of the temperature oscillations in the proximity of the sample can be determined.

Due to the flexibility of the NeSTRI apparatus, two distinct sets of images are obtained for each sample: i) the heating profile $H(x,y,t)$ locally generated in the sample from periodic

illumination by the pump beam, and ii) the amplitude $\delta\rho_0(x,y)$ and phase $\delta\phi_0(x,y)$ of periodic thermorefectance oscillations experienced by the “probe” beam in the proximity of the periodically heated sample. From a combination of these two pieces of information, the Fourier equation governing the diffusion of heat will be numerically solved using a finite difference method, and images of the thermal conductivity and thermal capacity will be obtained, without any need of contacting the sample with a heat sink. Thermally conducting domains of multilayer graphene on glass will be used to test our setup. To the best of our knowledge, this is the first report in which modulated thermorefectance methods are coupled with SNOM, to achieve simultaneous contactless imaging of thermal conductivity and thermal capacity at the nanoscale.

2.2 NeSTRI apparatus

The NeSTRI setup presented in this thesis has been implemented using a Witec Alpha 300S aperture-type AFM and SNOM system, equipped with non-contact hollow cantilever tips (SNOM-NC, NT-MDT Co.) [24, 27-29]. Tip apertures at 80-100 nm diameter are machined in these cantilevers using a focussed ion beam. The Witec Alpha 300S instrument is capable of scanning in the near-field the optical response of a sample in reflection or transmission mode and, simultaneously, probing the sample topography via AFM

Near-field optical response is obtained by illuminating the SNOM tip aperture through an upright confocal optical microscope. For reflection-mode SNOM imaging, evanescent waves locally generated at the tip aperture, and scattered by the sample, were collected at grazing angle by a subminiature accessory (SMA, Witec). The SMA was coupled by means of an optical fiber to a photomultiplier tube operating in photon counting regime (U64000, Hamamatsu). For transmission-mode SNOM, evanescent

waves locally generated at the tip aperture and scattered through the sample were collected by an inverted optical microscope and conveyed to the photomultiplier tube. In this way, continuous wave (CW) reflection-mode and transmission-mode SNOM images of the sample were obtained by illuminating the cantilever aperture with a 405 nm, diode-pumped laser (500 mW, Apinex) launched into a single-mode optical fiber coupled with the upright confocal microscope. Combination of reflection and transmission SNOM images were acquired with this assembly, shown in **Figure 2.1a**, and provided maps of the sample absorbance, $A_o(x,y)$ via the relationship

$$A_o(x,y) = I - \tau(x,y) - \rho(x,y) \quad (2.1)$$

where $\tau(x,y)$ and $\rho(x,y)$ are, respectively, the transmittance and reflectance of the sample recorded by SNOM at 405 nm. Information on the absorbance, in conjunction with knowledge of the laser power P_o , were used to determine the sample heating profile upon uniform illumination.

To record modulated thermoreflectance images, we used the setup shown in **Figure 2.1b**. Picture showing all the pieces of apparatus assembled to achieve our new thermal imaging is also shown in **Figure 2.2**. With this assembly, the above mentioned 500-mW laser at 405-nm is coupled with the inverted optical microscope situated below the sample, equipped with a 20x long working distance objective complete of glass-substrate correction ring. Large sample areas ($\sim 500 \mu\text{m}^2$) could be uniformly illuminated at $P_o = 50 \mu\text{W}/\mu\text{m}^2$ power. The laser beam is intersected with a mechanical chopper (SciTec Instruments) operated at angular frequencies from $\omega = 75 \text{ Hz}$ to 450 Hz. In this way, we obtain a pulsed “pump” beam that illuminates the sample and generates, at any time t , a periodic heat profile accordingly to the equation.

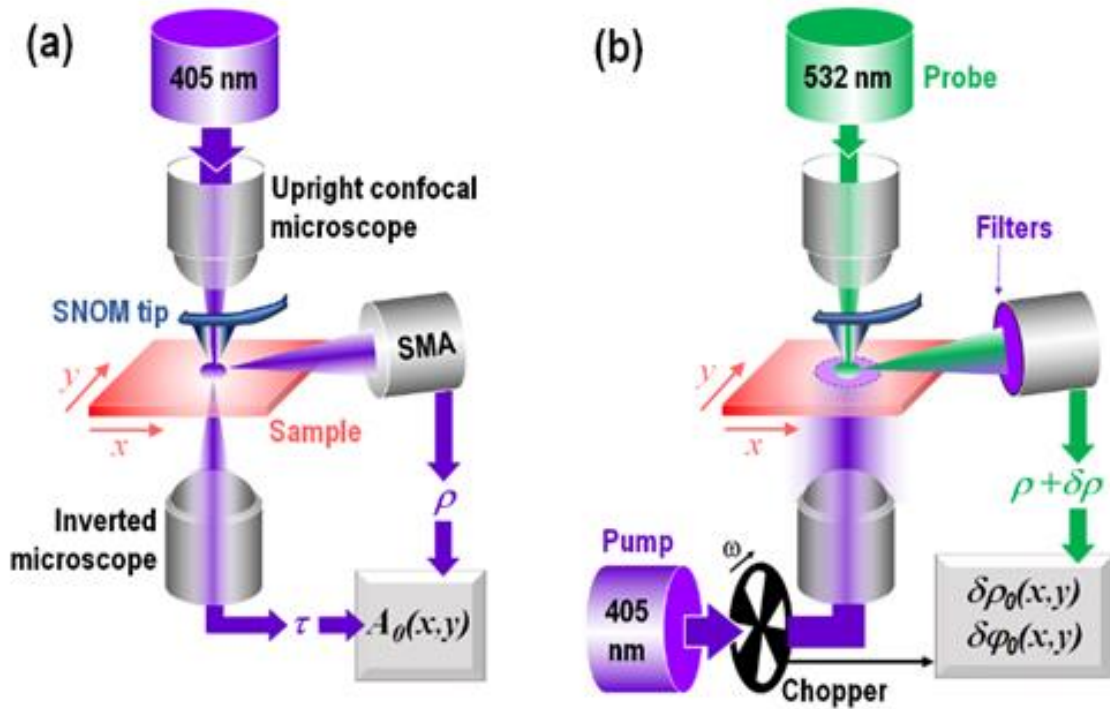


Figure 2.1: (a) Setup used for recording transmission (τ) and reflection (ρ) SNOM images, from which $A_{\theta}(x,y)$, the absorbance of the sample can be obtained and used to determine the heat generation profile according to eq.(2). (b) NeSTRI setup used for scanning near-field thermoreflectance images in phase ($\delta\phi_0$) and amplitude ($\delta\rho_0$). A 405-nm pump beam, modulated at frequency ω , heats the sample over a large area from the inverted microscope. Heat, after diffusing along the thin film surface, is transferred to air. Air changes in volume and thus experiences, at a certain phase lag, periodic changes in refractive index that induce small oscillations in reflectance at the air-sample interface. Such oscillations are probed, in amplitude and phase, by a CW 532-nm probe beam originating from the upright SNOM microscope and detected in lock-in mode via the SMA coupler. A set of filters at the SMA coupler eliminate 405-nm light scattered from the pump beam.

$$H(x,y,t) = P_0 \cdot A_0(x,y) / D(x,y) \cdot \exp\{i\omega t\} = H_0(x,y) \cdot \exp\{i\omega t\}, \quad (2.2)$$

where $D(x,y)$ is the thickness of the absorbing film, determined from AFM topography referenced to the glass substrate, and $H_0(x,y) = P_0 \cdot A_0(x,y) / D(x,y)$ represents the amount of heat locally deposited per sample unit volume. During pulsed heating from the pump beam, the sample surface was locally scanned in the near-field by evanescent light originating from a continuous “probe” laser (50 mW, Spectra Physics) at 532 nm wavelength and significantly lower power than the pump beam. The probe laser was coupled with the SNOM tip aperture by means of the upright confocal optical microscope. The amount of 532-nm evanescent radiation reflected at each point (x,y) of the surface was detected by the Witec SMA reflection SNOM accessory. A 405-nm holographic notch filter (Witec) and a 530-nm long-pass filter (Melles-Griot) were positioned in series with the SMA coupler to completely reject stray light from the pump beam and ensure that reflected light reaching the photo-multiplier tube originates entirely from the probe beam.

Upon sample heating, heat is transferred from the sample to air. Air increases in volume and experiences a consequent decrease in refractive index. The change in refractive index of the sample is negligible over the change in refractive index in air, because thermal dilatation is significantly higher in liquids than solids [23]. The amplitude $\delta\rho_0(x,y)$ of thermorefectance oscillations, experienced by the CW probe beam due to periodic heating of air from sample heating, is proportional to the temperature oscillations at the sample surface.

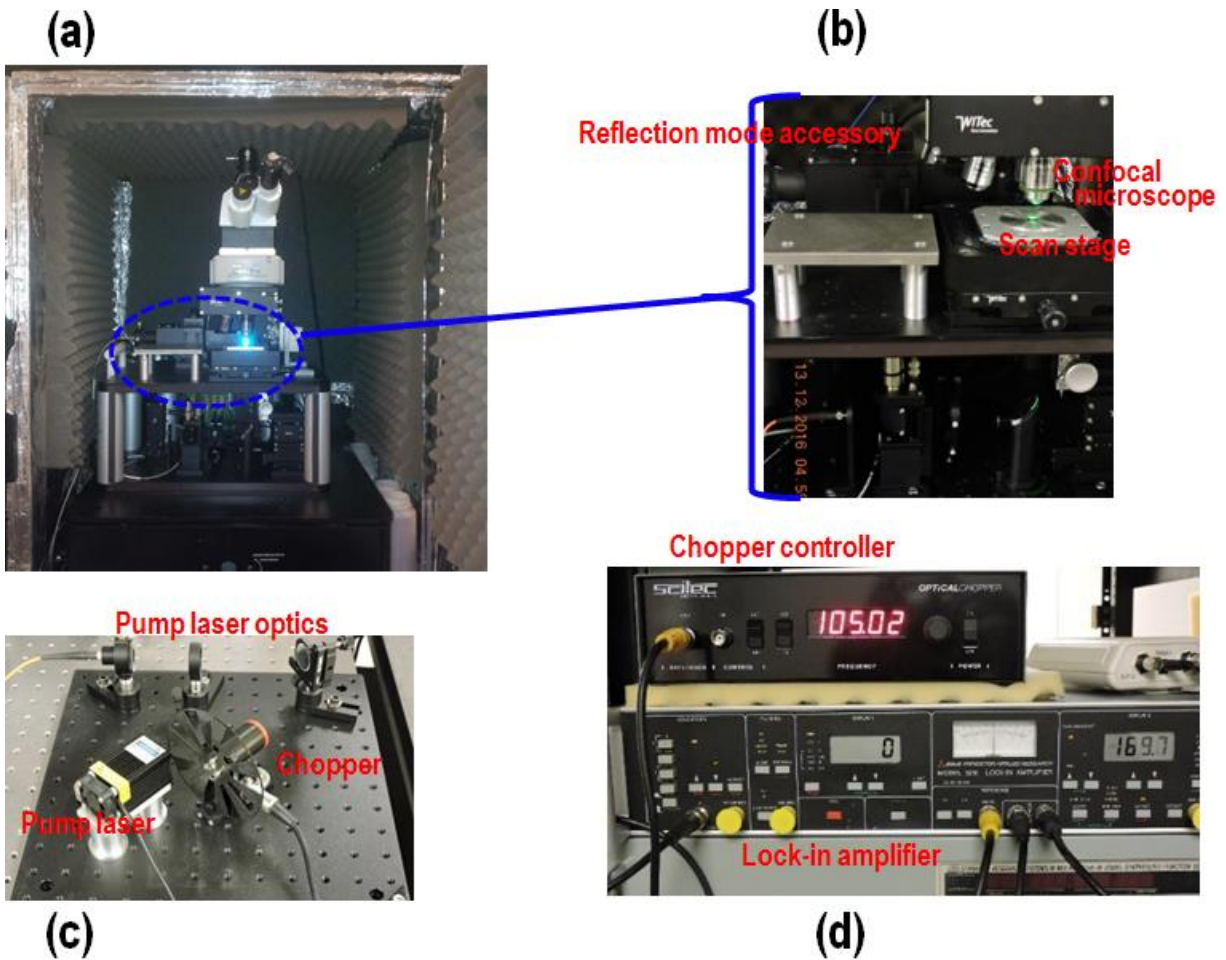


Figure 2.2: Picture of different pieces of apparatus coupled used to achieve our NeSTRI measurement. (a) Witec Alpha 300S aperture-type AFM/SNOM system in Fanchini's group laboratory in the Department of Physics and Astronomy at Western University (b) A magnified view of the system showing the upright confocal microscope for focusing the probe green laser onto the hollow AFM tip, scan stage and the reflection mode accessory. The inverted microscope used to focus the pump beam laser is not visible in this picture. (c) The pump beam laser, mechanical chopper for frequency modulation of pump beam and the pump beam optics for focusing and alignment. (d) The controller of the mechanical chopper and dual phase lock-in amplifier.

The phase lag $\delta\varphi_0(x,y)$ relative to the pump beam depends on the average mean free path of the thermal waves reaching each point (x,y) from the surrounding region. The complex thermorefectance at the sample surface is thus given by

$$\delta\rho(x,y,t) = \delta\rho_0(x,y) \cdot \exp\{i[\omega t + \delta\varphi_0(x,y)]\}. \quad (2.3)$$

In NeSTRI, $\delta\rho_0(x,y)$ and $\delta\varphi_0(x,y)$ can be separately recorded at each point by connecting the photomultiplier tube with a lock-in amplifier (3207, Princeton Instruments) referenced by the chopper. The output of the lock-in amplifier was subsequently coupled to the controller of the WiTec Alpha 300S instrument to produce 512x512 pixels in the scanned area. Phase and amplitude images of the complex thermorefectance at the sample-air interface could then be obtained.

2.3 Materials

Samples used to test our NeSTRI setup are multilayer graphene films, exfoliated from graphite using a surfactant-assisted method and deposited on transparent and thermally insulating glass substrates (BK7, Corning). Graphene-based thin films were chosen as test samples due to the strong interest displayed by the scientific and technological community on the thermal properties of this material. [24] Multilayer graphene in water was exfoliated from pyrolytic graphite by a surfactant-based process previously developed by Sharifi et al. [25,26] and described in details in chapter 1. A distinct advantage of this process is that the starting material obtained for exfoliation is less oxidized and less defective than graphite oxide prepared by the Hummers' method, [27] with significantly higher thermal conductivity [28]. Briefly, 6 mg of graphitic

material, pretreated in acid mixture and Piranha solution as discussed in chapter 1, was ultrasonicated for 4 hours in a 0.6 g/l aqueous solution of RNA, which promoted exfoliation. The resulting slurry was left to sediment overnight at 2°C in a beaker. The top three-quarters of the beaker content were centrifuged at 6,000 rpm for 1 h. The supernatant, consisting of N-layer graphene flakes, ($N = 1-200$ [25]) was used for the deposition multilayer graphene thin films by vacuum filtration.

For graphene-based thin film deposition, 5 ml of RNA-based suspension of N-layer graphene flakes in water were filtrated through a 220-nm pore size sacrificial membrane (Millipore). Small amounts of diluted suspensions are used to prevent re-aggregation of the suspended flakes during deposition on the filtration membrane. Membranes loaded with graphene flakes are transferred to the requisite substrates, and dried in a vacuum desiccator. The sacrificial membrane is etched using acetone baths in Petri dishes, thus obtaining random distributions of graphene domains on their substrate. A final methanol bath is used to remove the last traces of the membrane. Samples were annealed at 540°C for 5 h in a nitrogen-loaded glove box to completely remove any traces of RNA [25] prior to thermal measurements. The films are formed by sparse domains of light-absorbing and heat-conducting multilayer graphene on uniform, transparent, and thermally insulating surfaces of glass.

2.4. Numerical model

A numerical model was developed by Sina Kazemian in a collaboration within our research group with the objective to calculate the thermal conductivity $k(x,y)$ and heat capacity $C(x,y)$ of inhomogeneous thin films from the quantities imaged by NeSTRI: the heat generation profile (eq. 2) and the amplitude and phase of the complex

thermoreflectance at the sample surface (eq. 3). In this model, the substrate is assumed to be transparent and thermally insulating, a reliable assumption for our test samples and many other thin films of practical interest. The model requires a numerical solution of the inverse equation of heat [29] using a finite difference method.

Radiation from the pump beam is absorbed in different amounts at different locations of the thin film under investigation and heat locally generated by photons preferentially diffuses along the film surface, which leads to a thermal profile accordingly to the Fourier equation [29, 30]:

$$c(x, y) \frac{\partial T(x, y, t)}{\partial t} + \nabla \cdot [k(x, y) \nabla T(x, y, t)] = H(x, y, t). \quad (2.4)$$

Equation 2.4 is reminiscent of the conservation of energy in a control region about point (x, y) , in which heat can be accumulated, transferred and generated. It is worthwhile noting that, in our work, $T(x, y, t)$ does not represent the absolute temperature, but corresponds to the local temperature difference between the sample surface at point (x, y) and the environment.

In our experiments, $H(x, y, t)$ is periodic with the same periodicity as the chopper frequency, as seen from eq. 2.2. In this configuration, a solution of eq. 2.4 can be written by considering that the thermoreflectance carries only the Fourier component that is oscillating at such frequency: $T(x, y, t) = T_0(x, y) \cdot \exp\{i[\omega t + \delta\varphi_0(x, y)]\}$. Substitution of this solution into eq. 2.4 leads to the following expression for the equation of heat written in the Fourier domain:

$$i\omega c(x, y) T_0(x, y) \exp\{i\delta\varphi_0(x, y)\} + \nabla \cdot \{k(x, y) \nabla [T_0(x, y) \exp\{i\delta\varphi_0(x, y)\}]\} = P_0 A_0(x, y). \quad (2.5)$$

Equation 2.5 has two components, real and an imaginary, and their physical meaning is associated to the finite thermal diffusivity at which heat propagates along the thin film surface, due to nonzero lateral thermal diffusion length.

Equations 2.4 and 2.5 indicate that, for any given profile of heat generation (x,y,t) depend on the thermal conductivity and heat capacity at any other points on the thin film surface. At very short lateral thermal diffusion lengths, heat is released to air close to the point (x',y') at which it is generated, $T(x,y,t)$ only depends on the value of $H(x',y',t)$ at points situated in the very proximity of (x,y) , and eq.2.5 is real, with $\delta\varphi_0(x,y)\approx 0$. Conversely, at large thermal diffusion lengths, heat travels relatively long distances along the surface, before being released to air. In this way, relatively large heated domains will contribute to $T(x,y,t)$, and eq. 2.5 will be predominantly imaginary, with $\delta\varphi_0(x,y)$ closer to 90° . Since the lateral thermal diffusion length along the surface is inversely proportional to the pump beam frequency, NeSTRI measurements at different values of ω , leading to different phase lags, are needed to exhaustively understand the film thermal properties.

A linear relation exists between $T_0(x,y)$ and the thermorefectance[31].

$$\delta\rho_0(x,y) = hT_0(x,y), \quad (2.6)$$

where h , a negative proportionality coefficient, is independent of x , y and ω . It is convenient to write eq.2.5 in terms of $\delta\rho_0(x,y)$ instead of $T_0(x,y)$ because this is the quantity actually measured by NeSTRI. By replacing eq. 2.6 into eq. 2.5, we can write a complex equation in the Fourier domain, which links the phase and amplitude of the complex thermorefectance with the heat capacity and thermal conductivity at any generic point of the thin film:

$$i\omega c(x, y)\delta\rho_0(x, y)\exp\{i\delta\varphi_0(x, y)\} + \nabla\{k(x, y)\nabla[\delta\rho_0(x, y)\exp\{i\delta\varphi_0(x, y)\}]\} = hP_0A_0(x, y). \quad (2.7)$$

The physical meaning of the real and imaginary parts of eq. 2.7 is the same as in the corresponding components of eq. 2.5. The two components can be separately equated leading to the identities

$$\begin{aligned} \nabla k(x, y) \cdot \nabla \delta\rho_0(x, y) + k(x, y)\nabla^2 \delta\rho_0(x, y) \\ - k(x, y)\delta\rho_0(x, y)[\nabla \delta\varphi_0(x, y)]^2 = hP_0A_0(x, y)\cos \delta\varphi_0(x, y) \end{aligned} \quad (2.8)$$

for the real part, and

$$\begin{aligned} \omega c(x, y)\delta\rho_0(x, y) \\ + k(x, y)[\delta\rho_0(x, y)\nabla^2 \delta\varphi_0(x, y) + 2\nabla \delta\rho_0(x, y) \cdot \nabla \delta\varphi_0(x, y)] \\ + [\nabla k(x, y) \cdot \nabla \delta\varphi_0(x, y)]\delta\rho_0(x, y) = -hP_0A_0(x, y)\sin \delta\varphi_0(x, y) \end{aligned} \quad (2.9)$$

for the imaginary part. The solution of the real equation (eq. 2.8) provides $k(x,y)$, a map of the thermal conductivity of the thin film, which can then be replaced into eq. 2.9. $c(x,y)$ can thus be explicitated. In this way, the solution of the imaginary equation (eq. 2.9) provides a map of the film heat capacity.

Due to the nonanalytic nature of $\delta\rho_0(x,y)$, $\delta\varphi_0(x,y)$ and $A_0(x,y)$, the known quantities recorded by NeSTRI experiments, the solution of eq. 2.8 must be obtained numerically, using a finite difference method [32, 33]. The generality of this solution makes it suitable to analyze a large variety of thin films measured by NeSTRI. The numerical computer routine used to solve eq. 2.8 is described in detail in ref. 31. Boundary conditions for the numerical problem are the known values of $k(x_b, y_b)$ at $(x, y) = (x_b, y_b)$, the boundaries of the NeSTRI image, at which the

surface is made of glass and the thermal conductivity is known. In the specific case of our test samples, the thermal conductivity of glass was set at $k(x_b, y_b) = 1.1 \text{ W/m/K}$ [34]. The quantity $k(x, y)/h$ can be extracted from the numerical solution of eq. 2.8, and represents the thermal conductivity in specific arbitrary units that depend on the geometry of the used NSOM tip and its distance from the surface, via the proportionality coefficient of eq. 2.6. Due to the difficulty to estimate the tip-sample distance, the actual value of h involved in the right-hand term of eq. 2.8 needs to be determined experimentally. This can be done via eq. 2.9 because the specific heat capacity of glass, $c(x_b, y_b) = 860 \text{ J/Kg/K}$, is also known [34]. In this way, solution of eqs. 2.8 and 2.9 was implemented using a MatlabTM computer program available in ref. 31 and leads to the determination of $k(x, y)$ and $c(x, y)$.

2.5. Results

2.5.1 Sample absorbance

Figure 2.3 demonstrates that the phase and amplitude images measured using the NeSTRI setup shown in Figure 2.1b are from genuine thermorefectance phenomena originating from thermally-induced oscillations of the probe beam reflectivity at the air-sample interface. To demonstrate this, we carried out a set of measurements in which the pump and probe beams were alternatively switched off during the scan. These measurements show that NeSTRI images can only be observed when both the pump beam and the probe beam are impinging the sample. When either laser is turned off, the NeSTRI signal vanishes. These tests were carried out on a multilayer graphene flake which topography, measured by AFM, is shown in panel a of Figure 2.3. The corresponding CW reflectance image is shown in **Figure 2.3b**. Filters rejecting 405-nm purple light from the pump beam were in place, as shown in Figure 2.1b. In these conditions, it is

expected that the signal is entirely coming from 532-nm green light from the probe beam. As expected, it can be observed that, without any heating from the pump laser, the amplitude of the thermoreflectance image is below the detection limit, as demonstrated by **Figure 2.3c**. However, even in the absence of heating, a small phase lag is still observed in the correspondence of the graphene flake in Figure 2.3d, but this is no more than 2% of the phase shifts observed in the second and fourth quarter of the scan, when the sample is heated. This background phase lag can be assigned to limited sample self-heating from the probe beam. In summary, Figure 2.3c and 2.2d show that phase images are more sensitive than amplitude images in detecting small thermoreflectance oscillations, but undesired effects associated to weak self-heating from the probe beam are negligible at the pump power levels used in our experiments.

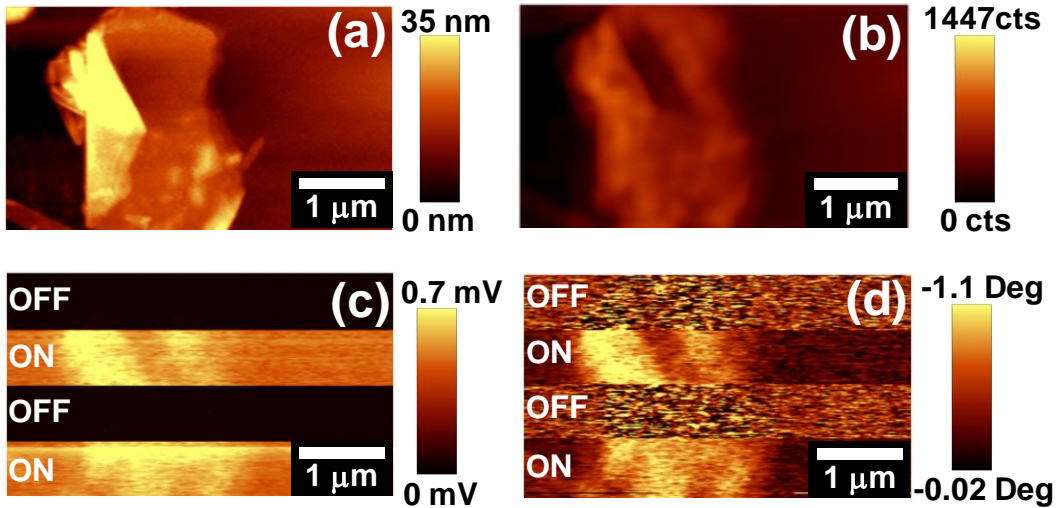


Figure 2.3: (a) AFM topography, (b) SNOM CW reflectance, and (c) amplitude and (d) phase of thermoreflectance modulations recorded from a multilayer graphene flake. The pump laser, modulated at $\omega = 150$ Hz, was switched off and on every 128 lines of a 512-line sample scan. Pump laser modulation has no effects on the topography and CW reflectance images, but it is essential for observing thermoreflectance images.

Although sample illumination from the pump beam is uniform, the value of $H(x,y,t)$ at a specific point also depends on the local value of the absorbance. Specifically, $H(x,y,t) = 0$ at any points on bare glass, at which $A_0(x,y) = 0$, while is more significant, up to $0.09 \text{ mW}/\mu\text{m}^2$, at points on relatively thick multilayer graphene. To quantify $A_0(x,y)$ from eq. 2.1 we imaged the reflectance and transmittance of the test sample using the SNOM setup shown in Figure 2.1a. The result of these measurements is presented in **Figures 2.4a–2.4c** that show, respectively, AFM topography, transmittance and reflectance images of the test sample. To determine the absolute intensities of the transmittance and reflectance from the photomultiplier counts shown in panels b and c of Figure 2.4, we considered $\tau(x_b, y_b) = 92\%$ and $\rho(x_b, y_b) = 8\%$ for glass [36], while zero counts correspond to 0% of both transmittance and reflectance. In this way, SNOM images can be normalized and the heat deposited at each point can be estimated from eq. 2.2.

Figure 2.4d shows the variation of $A_0(x,y)$ in multilayer graphene platelets as a function of the number of graphene layers. From the transmittance image shown in Figure 2.4b, it can be observed that the glass substrate is always significantly more transmitting than multilayer graphene. On the other hand, from Figure 2.4c, it can be noticed that the reflectance of glass and graphene are both relatively small and comparable, except at a few locations in which graphene flakes are particularly wrinkled and rich in ridges, and become highly reflecting with ρ up to 30%. There is a wide range of thicknesses and number of layers in the platelets shown in Figure 2.4. Nine different regions with relative thickness variations of no more than $\pm 10\%$ were selected from panel a and their transmittance and reflectance were determined from panels b and c, respectively.

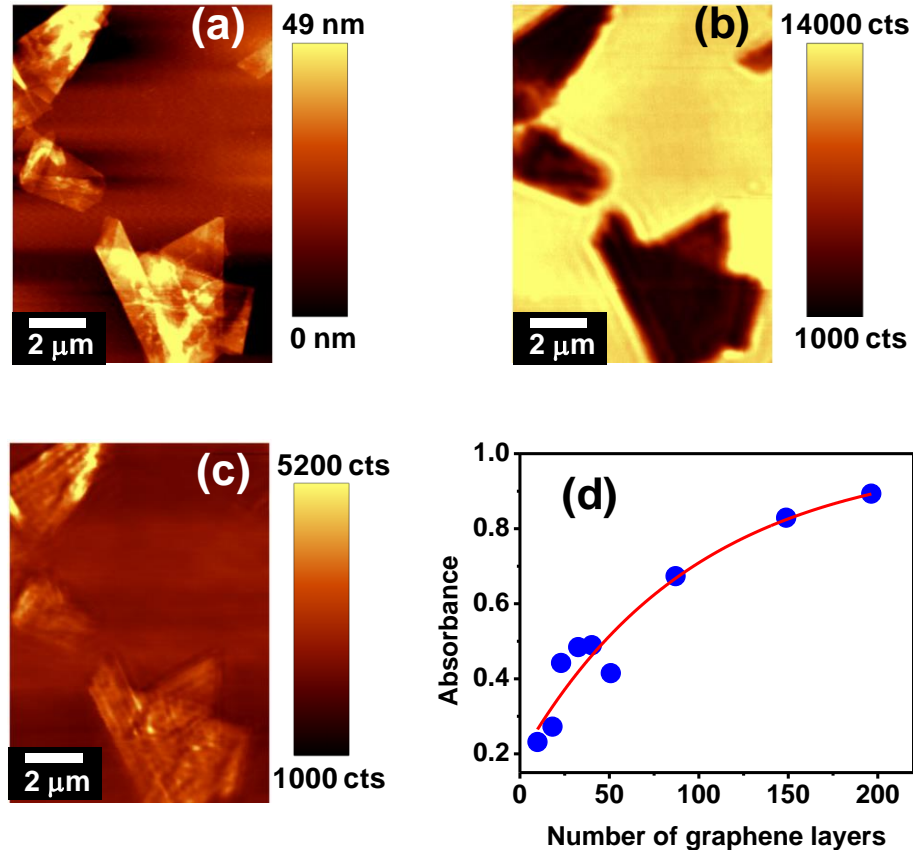


Figure 2.4: (a) AFM topography, (b) Transmission mode and (c) Reflection mode SNOM images of graphene platelets comprising of different number of layers. The topography was obtained simultaneously during SNOM measurements. (d) Absorbance, A_0 versus number, N of graphene layers. The absorbance was determined from the transmittance and reflectance data obtained from the SNOM images in (b) and (c). Multilayer graphene platelets are highly absorbing, while few-layer are semi-transparent. All of them are weakly reflecting.

From the thicknesses (x,y) shown in Figure 2.4a, the number of layers could be calculated for each selected region using the relationship $N = D/c_0$, where $c_0 = 0.3$ nm is the

interlayer spacing in graphene [37]. In this way, the average optical absorbance could be determined for each of the nine selected regions, and is plotted in Figure 2.4d.

Figure 2.4d shows that $A_0(x,y)$ increases at increasing number of layers, consistently with previous macroscopic observations that showed absorbance increase according to the Beer-Lambert law, $A_0 \sim 1 - \exp(-N/M)$ ($M \approx 50$) in multilayer graphene platelets [38]. We can thus infer that this relationship is valid in our system even at the nanoscale level. These results indicate that few-layer graphene platelets with less than 50 layers are locally transparent, with relatively low heat load applied to them. Dark areas in the SNOM transmittance image in Figure 2.4b are highly absorbing, and will also be affected by high thermal load. Due to such unavoidably different levels of heat generated at each point of the sample, knowledge of optical absorbance, calculated from eq. 2.2, will be critical for quantitative estimates of the thermal conductivity and thermal capacity of the test sample, as described in the next section.

2.5.2 Multi-frequency NeSTRI imaging

Figure 2.5 shows NeSTRI images in phase and amplitude of the test sample, recorded at 75 Hz. A close correlation between these images, recorded in non-contact from the sample, and the corresponding SNOM and topography images, recorded in contact with the sample and reported in Figure 2.4, can be observed. The thermal diffusion length along the surface decreases as the pump beam modulation frequency increases. Therefore, thermorefectance measurements at different values of ω lead to different amplitude and phase lags, and decrease the arbitrariness in the determination of the thermal properties [16-20].

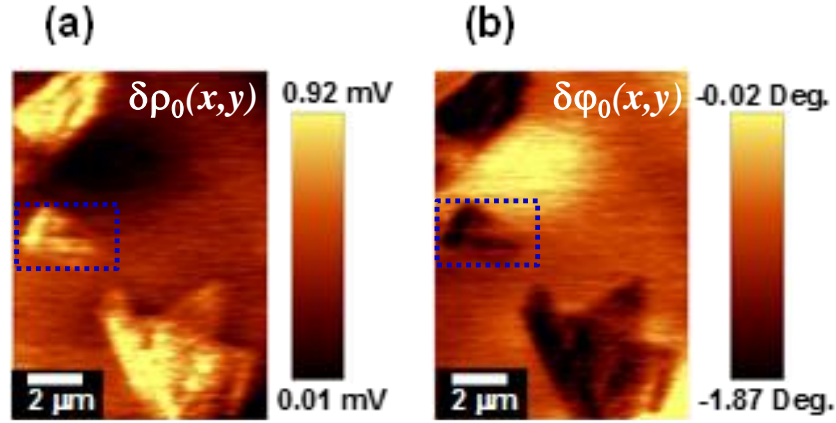


Figure 2.5: (a) NeSTRI amplitude and (b) phase images recorded at 75 Hz pump beam modulation frequency in non-contact from the test sample. Dotted squares highlight the detail that is further investigated in figures 2.6 to 2.8. Negative phase is a consequence of $h < 0$ in eq. 2.6 and is a strong indication of the fact that images are from genuine complex thermoreflectance signals. An excellent correlation between NeSTRI images in the present figure and the corresponding contact AFM and SNOM images from figure 2.4 can be observed.

Figure 2.6 show SNOM and multifrequency NeSTRI measurements on a detail of Figure 2.5. It shows the AFM topography (panel a) SNOM reflectance (panel b) and thermal amplitude and phase of the temperature profile for two different modulation frequencies of the pump beam. The amplitude and phase images at a larger set of frequencies is presented in the Appendix. Typical amplitude and phase of the temperature profile for graphene flake are obtained from the thermal images and fitted using Gaussian function. The peak of the Gaussian curve was taken as the representative amplitude and phase shown respectively in panel (g) and (h) of Figure 2.6.

Panels (c) ($\omega = 45$ Hz) and (e) ($\omega = 450$ Hz) in **Figure 2.6** show that the thermoreflectance amplitude is significantly different between thin and thick regions of the flake on the one hand, and between graphene and the glass substrate on the other hand. These images

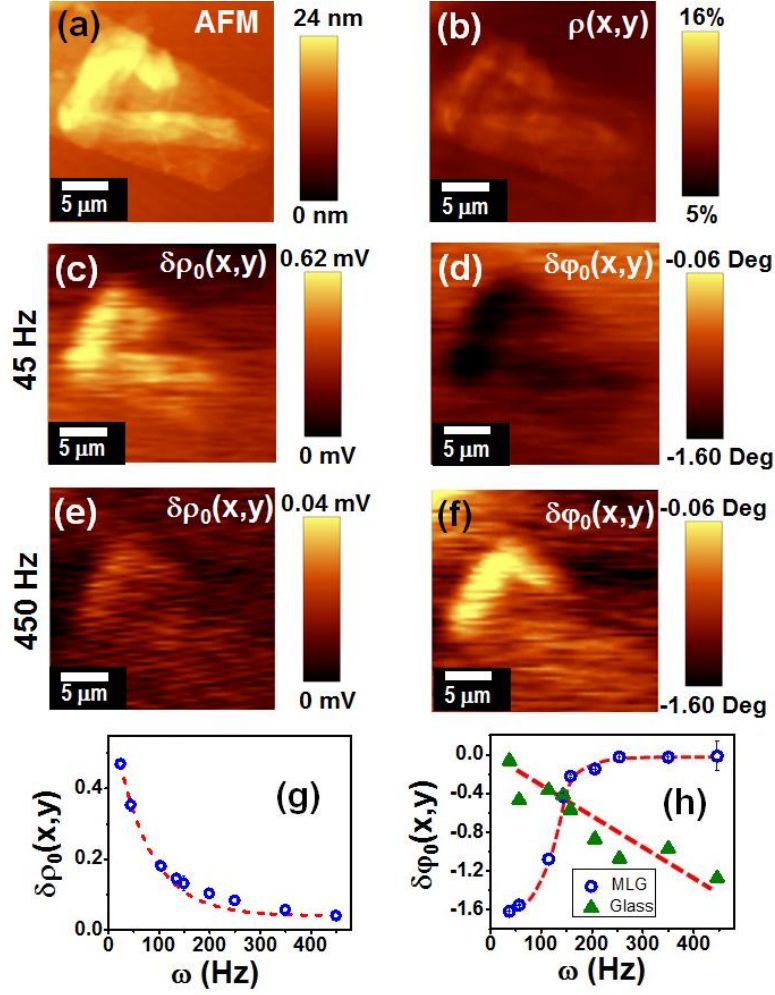


Figure 2.6: (a) Detail of AFM and (b) SNOM reflectance images of multilayer graphene (MLG) flake from figure 2.4. (c) Thermo-reflectance amplitude and (d) phase at $\omega = 45$ Hz frequency and (e) thermoreflectance amplitude and (f) phase at $\omega = 450$ Hz. It is always observed $\delta\phi_0(x,y) < 0$, as a consequence of $h < 0$ in eq. 2.6 (see ref. 31) which means that $\delta\rho(x,y,t)$ and $T(x,y,t)$ are in phase opposition of 180° . (g) The amplitude monotonically decreases as ω increases, as a consequence of shorter thermal diffusion length at increasing frequency. (h) The phase in graphene increases from about -1.6° to nearly zero and, from comparison of panels d and f, it is evident that $\delta\phi_0$ is lower in graphene than glass at 25 Hz, while, at 450 Hz, it is lower in glass than graphene.

represent the small changes in reflectivity of the probe beam directly measured in our setup by collimating the beam on the PMT detector and amplifying the periodic output voltage of the detector in a low noise lock-in amplifier referenced at the frequency, ω of the pump beam. When the changes in the reflectivity are larger due to stronger heat dissipation, the measured amplitude is higher, which leads to bright features in the amplitude images. In general, the magnitude of the amplitude always tends to monotonically decrease as ω increases, due to shorter thermal diffusion length at increasing frequency, as demonstrated in panel (g). The thermal diffusion length [29] can be defined as

$$L_{th} \approx (d/\omega)^{1/2}, \quad (2.10)$$

where $d(x,y) = k(x,y)/c(x,y)$ is the local thermal diffusivity of the sample, and the amplitude of the thermoreflectance signal is controlled by the thermal diffusion length. This is a very general trend in both thermoreflectance [16-20] and photothermal [38] experiments: when heat is delivered in short pulses, the thermal diffusion length is shorter at a constant heat diffusivity and less heat can be collected from a sample surface.

While the amplitude is always decreasing at increasing ω , phase images exhibit a more intriguing trend that also depends on the specific sample location. Panels (d) and (f) of Figure 2.6 show NeSTRI phase images at 45 Hz and 450 Hz, respectively. It is immediate that in panel (d), at low frequency, the graphene flake exhibits a larger phase lag than glass. Conversely, in panel (f), at high frequency, the glass substrate exhibits a larger phase lag than graphene. It is worthwhile noting that heat generation only occurs in graphene, because glass is optically non-absorbing. Instead, thermal dissipation may occur either from glass, which possess a very short thermal diffusion length regardless of the used pump beam frequency, or graphene where the

thermal diffusion length is significantly higher, up to several μm [39] and is determined by eq. 2.10.

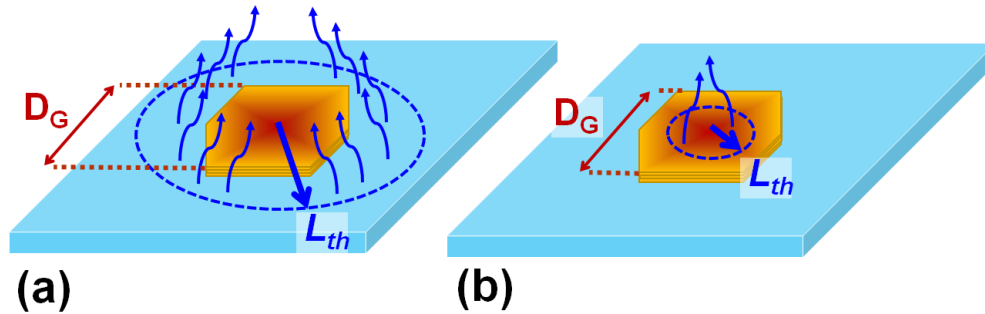


Figure 2.7: (a) Large thermal diffusion length (L_{th}) at low frequency, dominated by the diameter (D_G) of graphene flake, with heat dissipation mainly occurring in glass, and (b) Large thermal diffusion length at high frequency, in which eq. 2.10 holds and heat dissipation mainly occurs in graphene. A smaller phase lag occurs from the medium from which the largest amount of heat is dissipated to air. The dependency of L_{th} on ω leads to the 150 Hz crossover between regimes a and b, which results in phase images is, respectively, brighter and darker than the glass substrates as in figures 2.6b and d.

At low frequencies, the thermal diffusion length in graphene is larger than the size of the flake probed in **Figure 2.7** (i.e. about $10 \mu\text{m}$). Thus, the heat generated within the graphene sample is transferred in significant amounts to glass and a more significant phase lag is observed in graphene than glass, as demonstrated in **Figure 2.7a**. Conversely, at high frequencies, L_{th} is shorter than the flake size and heat generated in graphene is mostly dissipated within the same flake and minimally transferred to glass, as demonstrated in **Figure 2.7b**. The crossover between the high frequency and low frequency conditions can be estimated from Figure 2.6g, to corresponds to about $\omega = 150 \text{ Hz}$. From these considerations, it is evident that multifrequency

NeSTRI will be a very powerful and effective technique to visualize the thermal diffusivity and thermal diffusion length in layered materials.

2.6. Discussion

Figure 2.8 shows the specific heat images obtained by processing the thermorefectance data shown in Figure 2.6 by using eqs. 2.8 and 2.9. It can be observed that, within the experimental errors, the specific heat is independent of the frequency used in the measurements. It can also be observed that the specific heat is not significantly different in glass (860 J/Kg/K) and graphite (720 J/kg/K). At room temperature, Dulong-Petit law holds for a large class of materials for which the thermal properties are determined by lattice properties [40]. Consequently, a slowly varying specific heat along the entire surface is realistic. Local variations can only be observed at locations in which the low-dimensional nature of the thin film is more evident, including graphene edges, defects, and particularly thin regions.

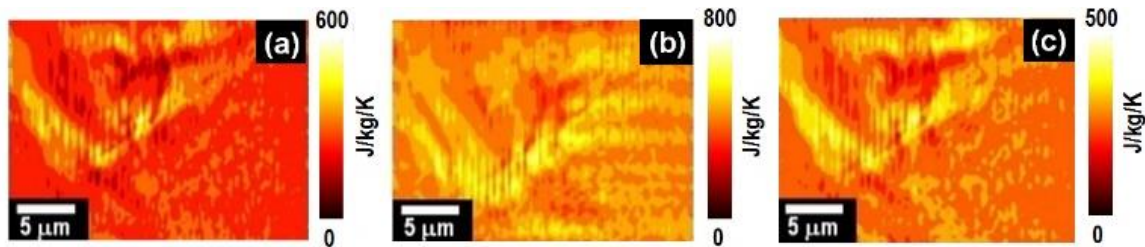


Figure 2.8. (a) Images of specific heat for the multilayer graphene flake previously reported in figure. 2.6 and independently obtained at (a) $\omega = 75$ Hz, (b) $\omega = 200$ Hz, and (c) $\omega = 450$ Hz

Figure 2.9 shows the thermal conductivity maps extracted from NeSTRI thermoreflectance images from the same regions and at the same frequencies as the specific heat images in Figure 2.8. From panel b we notice that the thermal conductivity is higher at certain edges than at the center of the graphene flake. There are two types of edges in graphene, armchair and zigzag. Different atomic spacing along the armchair and zigzag edges results in distinctly different electron and phonon density distributions, with armchair edge atoms forming shorter and stronger bonds [31].

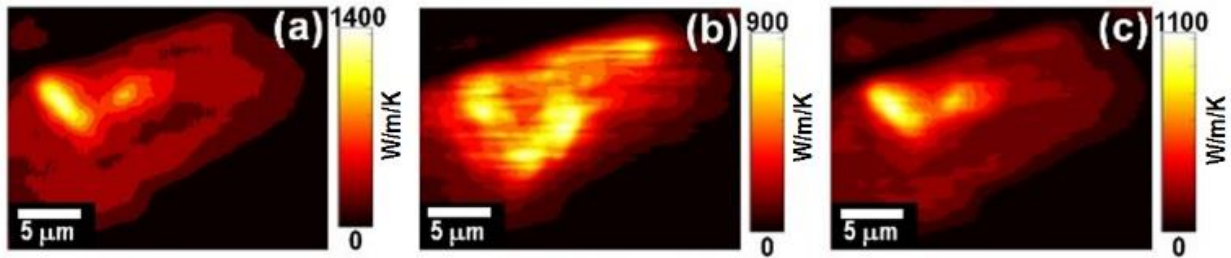


Figure 2.9: Thermal conductivity maps for three different frequencies, (a) 75 Hz, (b) 200 Hz and (c) 450 Hz. Although the images are slightly different, the thermal conductivity is expected to not depend on the modulation frequency of the pump beam since k_{th} is a material property. The discrepancy in k_{th} may be related to slight drift in pump beam power that sometimes occurs and also on possible contribution from convection. The role of convection is however very limited in NeSTRI because air molecule velocity is ≈ 0 near the sample surface when scanning in out of contact but in close proximity to sample surface.

Although the zigzag edges are less dense than armchair edges, the armchair edges have lower energy due to the fact they can form triple bonds [32, 33]. Armchair and zigzag

edges also have different phonon distribution of states with the armchair edges having more zone boundary phonons than zigzag edges. Since Umklapp process [26] is responsible for thermal resistivity effects, it is expected that the edge modes with higher density of states at the zone boundary would have a lower thermal conductivity. Also due to anisotropy in the phonon dispersion for graphene nano layers, zigzag graphene nano layers have higher thermal conductance than armchair graphene nano ribbons of comparable widths [34]. For the flake under consideration we recognize both armchair and zigzag edges, in consideration of its triangular shape. The different thermal conductivity at the edges may be related to different edge nature.

2.7. Conclusion

We measure the phase shift and amplitude of the sample thermoreflectance. We implement them into Fourier heat equation and we derive the thermal conductivity and heat capacity at each point, and therefore we have thermal conductivity and specific heat capacity images for the sample. By using contactless method for developing thermal conductivity maps, we measured the thermal conductivity of the surface of the sample more accurately and reliably than the previously measured data by photothermal deflection microscopy (PDS) [38]. The thermal properties of graphene-based thin films measured by NeSTRI are consistent with the previous measurements by Raman [24], with room-temperature thermal conductivity values between ~ 0 -5000 W/m/K. Our NeSTRI apparatus have allowed the imaging of fluctuations at the nanoscale of the thermal properties of thin films of graphene and other thin film materials and the results prove that a direct relationship exists between the microstructure of thin film materials and their

thermal properties. Our method is suitable to be extended to image the thermal properties of a large class of sparse, layered and thin film materials.

References

- [1] S. E. Liu, J. S. Wang, Y. R. Lu, D. S. Huang, C. F. Huang, W. H. Hsieh, J. H. Lee, Y. S. Tsai, J. R. Shih, Y.H. Lee, K. Wu, *In Reliability Physics Symp.*, **2014** IEEE Int., IEEE: NY, 2014, pp 4A.4.1 – 4A.4.4
- [2] D.G. Cahill, *Review of Scientific Instruments*, **1990**, 61, 802
- [3] W. J. Parker, R. J. Jenkins, C. P. Butler, G. L. Abbot, *J. Appl. Phys.*, **1964**, 32, 1679
- [4] W. B. Jackson, N. M. Amer, A. C. Boccara, D. Fournier, *Appl. Optics*, **1981**, 20, 1333.
- [5] W.J. Parker, R.J. Jenkins, C. P. Butler, G. L. Abbot, *J. Appl. Phys.*, **1964**,32, 1679
- [6] S. Gomes, A. Assy, P.O. Chapuis, *Phys. Stat. Solid.*, **2015** 212, 477.
- [7] T. Borca-Tasciuc. *Annu. Rev. Heat Transfer*, **2013**, 16, 211
- [8] D. Sarid, P. Khulbe, R. Grover, *Solid State Commun.*, 2008**145**, 389
- [9] A. Bontempi, L. Their, D. Teysieux, *High Temp.-High Press.*, **2014**, 46, 321
- [10] G. Hwang, J. Chung, O. Kwon, *Rev. Sci. Instrum.*,**2014**, 85, 114901
- [11] P.D. Tovee, O.V. Kolosov, *Nanotechnology*,**2013**, 24, 465706
- [12] J. Martinek, P. Klapetek, A. C. Campbell, *Ultramicroscopy*, **2015**,155, 55.
- [13] K. Kim, W. Jeong, W. Lee and P. Reddy,*ACS Nano*, **2012**, 81, 114901.
- [14] P. L. Kapitza., *J. Phys. (USSR)*, **1941**,4, 181.
- [15] K. N. Zinoveva., *Soviet Physics JETP*, **1971**,33 (6), 1205.
- [16] L. J. Inglehart, A. Broniatowski, D. Fournier, A. C. Boccara, F. Lepoutre., *Appl. Phys. Lett.*,**1990**, 56, 1749

- [17] L. Pottier, *Appl. Phys. Lett.*, **1994**, 64, 1618.
- [18] B. Li, L. Pottier, J.P. Roger, D. Fournier. *AIP Conf. Proc.*, **1999**,463, 336.
- [19] A. J. Schmidt, R. Cheaito, M. Chiesa, *Rev. Sci. Instrum.*, **2009**,80, 94901.
- [20] G. Langer, J. Hartmann, M. Reichling ,*Rev. Sci. Instrum.*, **1997**, 68(3), 1510.
- [21] E. Betzig, J. K. Trautman, *Science*, **1992**, 257, 189
- [22] S. Ezugwu, H. Ye and G. Fanchini, *Nanoscale*, **2015**, **7**, 252.
- [23] Handbook of Physical Quantities, edited by I. S. Grigoriev, E. Z. Meilikhov, CRC Press, Inc. Boca Raton, FL, USA, **1997**.
- [24] A. A. Balandin, *Nature Materials*, **2011**, 10, 569
- [25] F. Sharifi, R. Bauld, M. S. Ahmed G. Fanchini, *Small*, **2012**, 8, 699.
- [26] F. Pashae, F. Sharifi, G. Fanchini, F. Lagugne-Labarthe, *Phys. Chem. Chem. Phys.*, **2015**, 17, 21315.
- [27] G. Eda, G. Fanchini, M. Chhowalla, *Nature Nano*, **2008**, 3, 270
- [28] Z. Wu, Z. Chen, X. Du, J. M. Logan, J. Sippel, M. Nikolou, K. Kamaras, J. R. Reynolds, D. B. Tanner, A. F. Hebard, A. G. Rinzler. *Science*, **2004**, 305(5688), 1273
- [29] H. S. Carslaw, J. C. Jaeger, *Conduction of Heat in Solids (2nd ed.)*, Oxford University Press, London **1959**
- [30] N. Ashcroft and N. D. Mermin, *Solid State Physics*, Saunders College, Philadelphia, **1976**.
- [31] S. Ezugwu, S. Kazemian, D. W. Choi, R. Bauld, G. Fanchini. *Contactless scanning near-field thermo-reflectance imaging*. Under Review in *Nanoscale* **2016**.

- [32] K. A. Atkinson, *An Introduction to Numerical Analysis (2nd ed.)*, John Wiley & Sons New York, **1989**.
- [33] A. Taflove, S. C. Hagness, *Computational Electromagnetics: The Finite Difference Time Domain Method*, Artech House, Norwood, **2000**
- [34] M. J. Assael, S. Botsios, K. Gialou, and I. N. Metaxa, *International Journal of Thermophysics*, **2005**, 26, 1595
- [35] S. Rudtsch, R. Stosch, U. Hammerschmidt, In *Proc. 16th Europ. Conf. Thermophys. Props.*, London (**2002**).
- [36] Web resource: <http://www.crystran.co.uk/optical-materials/optical-glass-n-bk7-and-others>. Accessed on July 2, 2016.
- [37] K. Spyrou, Petra Rudolf, *An Introduction to Graphene in Functionalization of Graphene, First Edition. Edited by Vasilios Georgakilas*. Wiley-VCH Verlag GmbH & Co. KGaA. **2014**.
- [38] M. S. Ahmed, S. Ezugwu, R. Divigalpitiya, G. Fanchini. *Carbon* **2013**, 61, 59
- [39] D. L. Nika, S. Ghosh, E. P. Pokatilov, A. A. Balandin, *Appl. Phys. Lett.* **2009**, 94, 151911
- [40] J. S. Blakemore, *Solid State Physics*, W. B. Saunders Company, Philadelphia, **1969**.

Chapter 3

Nanoscale investigation of graphene-based thin films decorated with copper Nanoparticles²

3. 1 Introduction

In order to utilize graphene-based materials in nanoelectronics and sustainable energy applications, it is of paramount importance to establish physical relationships between their fabrication conditions and electronic performance. Modeling the effects of the incorporation of specific heteroatoms and impurities in graphene is a typical example of such a requirement. It is well known that the electronic properties of graphene can be tailored via substitutional doping or by chemically bonding specific functional groups to the graphene layer [1-5]. However, substitutional doping and functionalization also lead to additional undesired effects, because the alteration of graphene through chemical bonding significantly affects its electronic structure near the canonical point, which is responsible for the exceptional carrier mobility in graphene-based materials [6]. Chen *et al.* demonstrated that the carrier mobility decreases with increasing dopant density in graphene that was substitutionally doped with potassium, as a result of the scattering of π -electrons in graphene from potassium centers [5].

Controlling the electronic structure of graphene flakes by assembling metallic structures on their surface is another promising direction of research for tailoring their electronic properties, with significant applications in the fabrication of batteries [7], supercapacitors [8], fuel cells [9] and other devices for electronics and energy applications [10, 11]. Using first principle calculations Giovannetti *et al.* [12] showed that the electronic band structure of graphene can be

²This chapter is published: A. Akbari-Sharbat, S. Ezugwu, M. S. Ahmed, M. G. Cottam and G. Fanchini. *Carbon* 61 (2015) 595.

altered by applying metallic layers on its surface. They demonstrated that this effect is strongly dependent on the specific type of metal being used, with the formation of chemical bonds that may significantly alter the band structure of graphene near the Dirac point in the case of some specific metals (such as Co, Ni, and Pd). However, for other metals (Cu, Al, Ag, Au, and Pt), bonding with metals only caused shifts in the Fermi energy of graphene, which resulted in the doping of this material without significant alteration to its band structure. The distinct behavior of different metals was attributed to differences in their work function relative to graphene [12].

While the work of Giovannetti *et al.* pointed out at an attractive avenue for producing doped large-area graphene thin films while limitedly altering their electronic band structure near the Dirac point, assembling metallic layers on top of graphene sheets is not viable for practical applications, for which access to the graphene surface is required [7-11]. To this end, the use of nanoparticles of specific metals, including gold [13] and copper [14-15], has been explored for graphene-based devices. However, the roles of the size, shape and concentration of these nanoparticles in affecting the microscopic properties of the resulting nanocomposite systems have never been investigated in detail. For instance, it is not clear if the increase in electrical conductivity that has often been observed in graphene layers decorated with metallic nanoparticles [16] is due to some form of substitutional doping, like in crystalline materials, or to other effects. Furthermore, it is unclear if the specific location at which a metallic nanoparticle is positioned (e.g. at the center of a graphene flake, or near an edge with a specific conformation) is important in affecting the electronic structure and electrical properties of the system [17-18].

In this chapter, we investigate the influence of metal nanoparticles on the electronic properties of graphene-based thin films formed by collections of few-layer graphene domains that have been decorated with copper nanoparticles (Cu-NPs) [19] at different diameter and

surface area coverage. We developed a theoretical model at the tight-binding level in order to understand the Fermi level shifts and changes in electrical conductivity that we observed using scanning Kelvin-probe force microscopy (SKPFM) and electrical conductivity measurements.

3.2 Experimental

Transparent and conducting graphene-based thin films were deposited onto Si(100) and glass substrates using the vacuum filtration process discussed in section 1.2.1 of Chapter 1. This fabrication procedure yields graphene-based thin films very similar to those being currently investigated for several large-area applications in electronics and sustainable energy [20,21,22] and, therefore, offers a realistic benchmark for realistic theoretical studies of their doping mechanisms. The thin-film deposition process basically consists of three steps: *i)* 5 mL of water suspension of graphene flakes and RNA are vacuum-filtrated through a 220-nm pore size nitrocellulose filtration membrane (Millipore) which leads to the deposition of graphene flakes on the membrane if sufficiently small amounts of diluted suspensions are used to prevent re-aggregation of the flakes; *ii)* the filtration membrane loaded with graphene flakes is subsequently transferred onto the requisite substrate and dried under load in a vacuum desiccator; *iii)* the filtration membrane is etched in consecutive acetone and methanol baths, leaving behind a random distribution of graphene domains and RNA aggregates on their substrate; and *iv)* the samples were pre-annealed at 550°C for 5 hrs to remove RNA and, also, completely reduce them.

To decorate graphene-based thin films with Cu-NPs, we introduced them into an ultra-high vacuum radio-frequency (RF) magnetron sputtering chamber (base vacuum $\sim 10^{-7}$ mTorr) attached to a nitrogen-filled glove box (VAC Nexus II) to allow for storage and manipulation of samples with no oxygen exposure [19,21]. The sputtering system is complete with a process gas

flow meter (Omega F900) and RF matching network (RF VII). RF sputtering of Cu was carried out from a high purity target (>99.99%) and using argon as a process gas. Two different sets of identical graphene thin films were thus decorated with Cu-NPs. The first set, obtained by varying the annealing temperature from 200°C to 550°C at a constant annealing time of 4 hours, yielded to different Cu-NP diameters as shown in **Figure 3.1(a)-(d)**. The second set, obtained by varying the annealing time from 1 hour to 4 hours at a constant annealing temperature of 550°C, resulted in different copper area coverage on the graphene surface. In both cases, non-annealed Cu films formed a semi-continuous system of interconnected Cu particles [21] and the subsequent annealing process in the contiguous glove-box was a critical step for obtaining well-isolated Cu-NPs [19,21]. Control Cu-NP samples were also deposited and annealed on indium tin oxide (ITO) thin films (15 Ω/\square sheet resistance, Aldrich) in the same system described above.

Four-point probe electrical characterization of the samples (Signatone S725 probe station) in planar configuration indicates a strong increase in electrical conductivity of each film upon its decoration with Cu-NPs. Optical transmittance of the samples was measured at normal incidence in a range of wavelengths between 400 nm and 800 nm using a Varian DMS80 spectrometer. SKPFM measurements were performed at room temperature using a Witec Alfa 300S AFM system integrated with a Kelvin-probe force accessory described previously in Section 1.3.2 of chapter 1. The work function and topography of graphene decorated with Cu-NPs were mapped simultaneously using this equipment that is housed in a nitrogen-purged compartment, in which capsules containing the samples are directly transferred from the glove box. During SKPFM, the local contact potential difference V_{CPD} between the tip and the sample surface [22] can be expressed as

$$q \cdot V_{CPD} = \varphi_{tip} - \varphi_{sample}, \quad (3.1)$$

where $q = 1.6 \times 10^{-19}$ C is the elementary charge and ϕ_{tip} and ϕ_{sample} indicate the work functions of the tip and the sample, respectively. Their difference corresponds to the difference between the Fermi levels within the two systems. For our SKPFM experiments, a platinum-coated AFM tip with $\omega_0 \approx 75$ kHz resonance frequency (Nano Sensors Inc.) was used.

3.3 Results

3.3.1 Control of Cu-NP's size and distribution on graphene surface

A unique advantage offered by our RF sputtering system is that it allows us to independently control the average particle diameter and the area of graphene-based films covered by Cu by varying the sputtering time, annealing temperature and annealing time [19, 21]. Figure 3.1 (a)-(c) show the scanning electron microscope (SEM) images of a graphene-based film decorated by Cu-NPs obtained at different thermal treatments in glove box.

At a constant RF power and pressure, samples sputtered for 5 minutes have higher area coverage of nanoparticles on graphene than samples sputtered for lower times (2 min. or 3 min.). Samples with higher concentration of particles also require higher annealing temperature to achieve complete nucleation to obtain copper islands with larger diameter as shown in **Figure 3.1(d)**. By extrapolating the surface area covered by Cu-NPs from AFM micrographs, we find that the annealing time decreases the surface coverage area of our graphene films, as shown in **Figure 3.1(e)**. Using these adjustable experimental variables, samples were produced for a comprehensive parametric study of the effect of Cu-NPs on the electronic properties of graphene films.

3.3.2 Transparency of graphene thin films decorated with Cu-NPs

A clear fingerprint of the incorporation of Cu-np onto graphene thin films is represented by the appearance of a dip (or a peak in case of absorption spectra) situated around 550 - 590 nm,

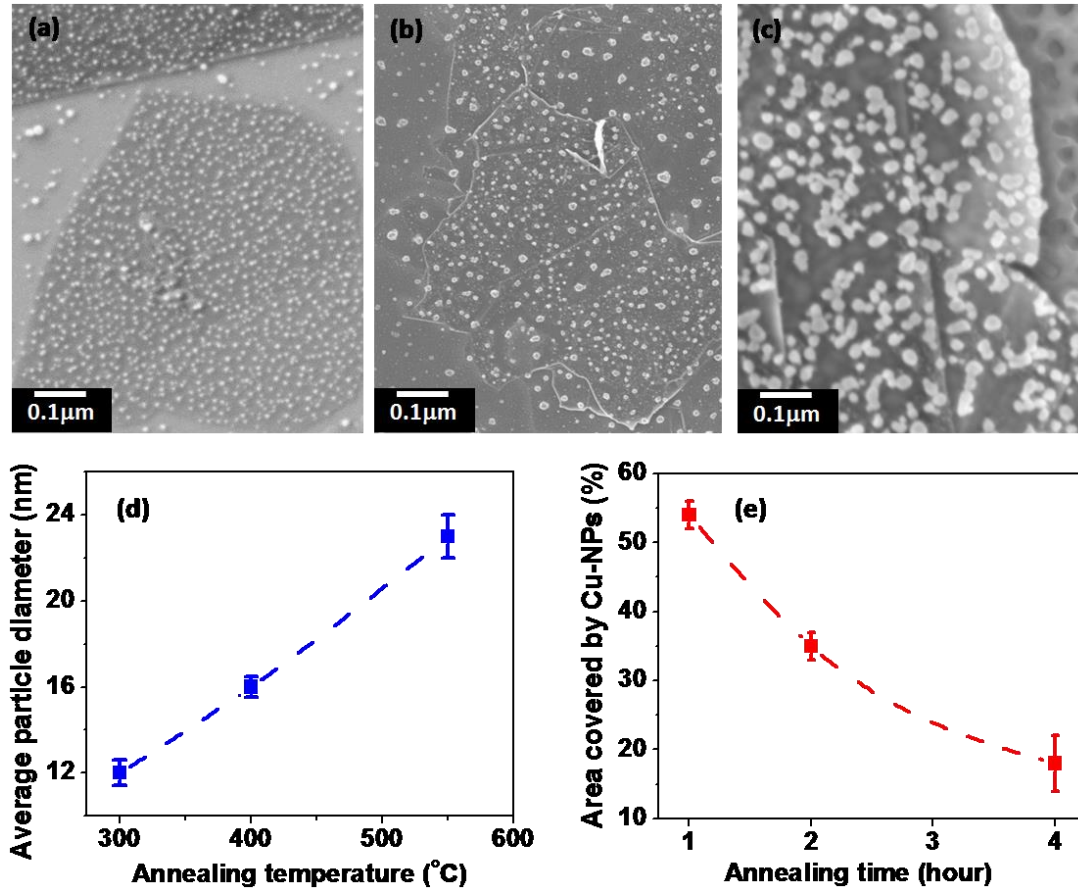


Figure 3.1: SEM images of graphene-based thin films decorated with Cu-NPs. Cu-NPs were deposited at different sputtering times of 2, 3 and 5 minutes, respectively, and annealed at (a) 300°C, (b) 400°C and (c) 550°C. (d) Variation of the average diameter of Cu-NPs decorated on the graphene samples shown in the SEM images. (e) Fraction of graphene surface covered by Cu-NPs obtained after annealing at different times.

which can be assigned to surface plasmon resonance absorption of metallic nanoparticles [23, 24]. The position of the surface plasmon peak maximum can be red-shifted depending on the particle diameters [25]. In **Figure 3.2**, the transmittance spectra are plotted for the bare graphene film and the films decorated with Cu-NP's for a range of particle diameters and surface area coverage.

From both panels of Figure 3.2, it can be observed that the presence of Cu-NPs produces a significant change in the transmittance spectra and position of resonance bands based on the distribution of the particles on the graphene surface. The variation of coverage area from $f_j = 0.18$ to $f_j = 0.54$ results in a decrease in optical transmittance of the samples due to increased concentration of Cu-NPs on the surface of graphene without significantly shifting the wavelength of the copper surface plasmon resonance peak as can be seen in Figure 3.2(a). On the other hand, panel b of Figure 3.2 shows that the transmittance spectra of copper doped-graphene films depend on the size distribution of the Cu-NPs. In this case, the position of the plasmon resonance peak shifts to higher wavelength, from 540 nm to 580 nm, at increasing particles diameter, from $D = 12$ nm to $D = 23$ nm.

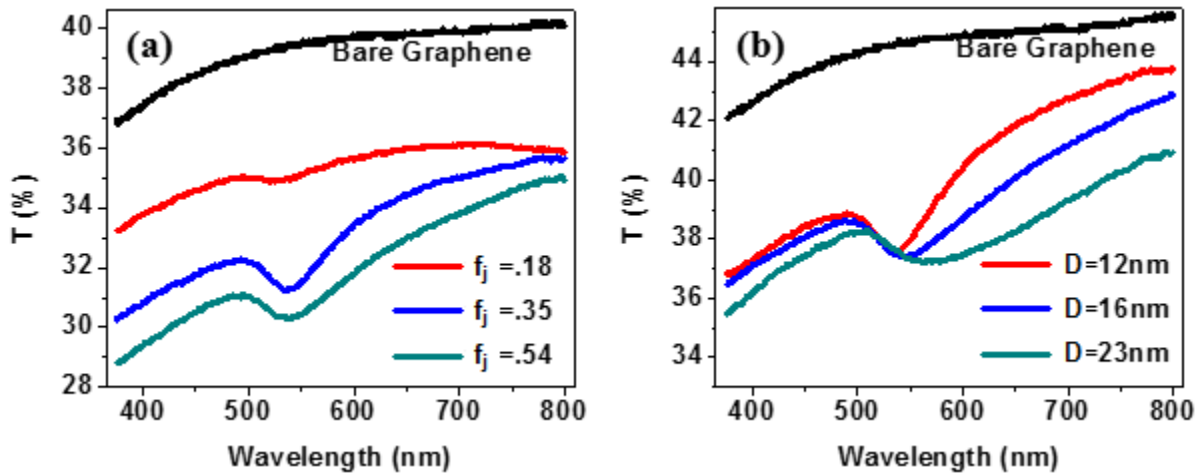


Figure 3.2: UV-visible transmission spectra of a set of samples at (a) increasing area coverage by Cu-NPs, showing a decrease in transmittance and (b) increasing nanoparticle diameter. The dips at ~550 nm are assigned to surface plasmon resonance of Cu-NPs. The transmittance of a bare graphene thin film is also included in both plots as a reference.

3.3.3 The work function of graphene-based thin film decorated with Cu-NPs

AFM and SKPFM micrographs of a transparent and conducting graphene film with $f_j =$

15±5% Cu-NP area coverage by Cu are shown in **Figure 3.3(a) and (b)**, respectively. We observe that the variation in the work function of graphene decorated with Cu-NPs principally depends on the nanoparticle diameter and more limitedly on the area coverage by Cu.

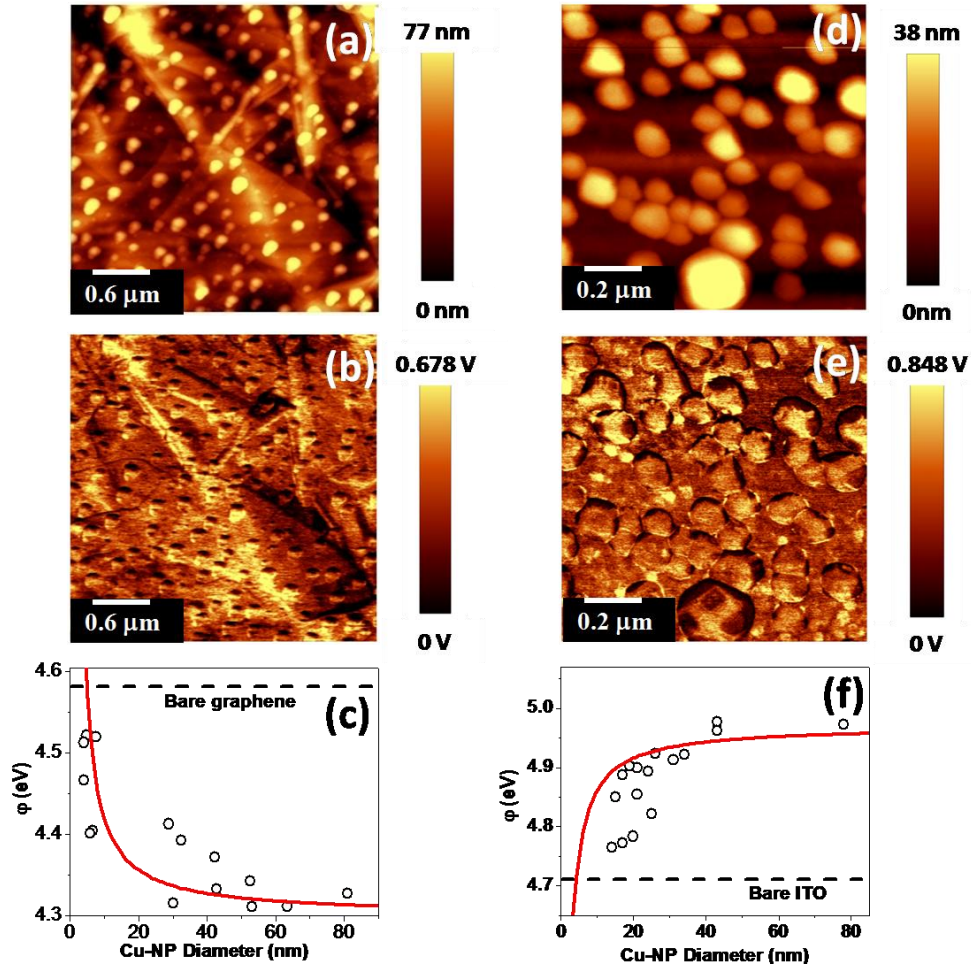


Figure 3.3: (a) AFM and (b) SKPFM micrographs of graphene-based thin film decorated with Cu-NPs. (c) Plot of the work function vs. Cu-NP diameter for Cu-NPs on graphene (d) AFM and (e) SKPFM micrographs of Cu-NPs on ITO. (f) Plot of work function vs. Cu-NP diameter for Cu-NPs on ITO. As AFM tend to overestimate NP diameters, the indicated diameter in (c) and (f) was obtained from the height profile of NP's shown in (a) and (d) and similar images obtained during simultaneous AFM/SKPFM measurements. The different trends for ϕ as a function of the diameter are consistent with the fact that electrons are withdrawn by graphene from Cu-NPs.

The work function of metal nanoparticles decreases at decreasing diameter of the particles, based on a classical description of the image potential for metals: in order to remove an electron from a metal, work need to be done against the image force which increases inversely with the curvature of the metal surface [17]. This classical description for the size dependence of nanoparticles on their work function has been verified experimentally for spherical metallic nanoparticles (with diameters of several nm) based on photoemission measurements [3]. **Figure 3.3(c)** is a plot of the work function of Cu-NPs vs. the particle diameter simultaneously measured by SKPFM and AFM. The diameter of the Cu-NPs was extracted from the AFM topography micrographs. The trace in Figure 3.3(c) comes from the theoretical model based on the method of images [18]:

$$\varphi = \varphi_{\infty} + \frac{1.08}{D} eV, \quad (3.2)$$

where φ_{∞} is the work function of a very large particle in the limit of infinite diameter, and D is the diameter of the metallic nanoparticle in nanometer. This model is in good agreement with our KPFM experiments without any adjustable parameters as demonstrated in Figure 3.3(c).

Figure 3.3(c) also shows that the work function for the absorbed Cu-NPs is lower than the work function of bare graphene, which indicates that the Fermi level of graphene islands shifts into the conduction band. This shift increases the electron carrier density, effectively making graphene *n*-type as doped by Cu-NPs. Analysis of Figure 3.3(c) also suggests that very small Cu-NPs with diameter below ~ 5 nm might have a work function larger than graphene, effectively shifting the Fermi level into the valence band (where the majority carriers become holes), provided these particles retain their metallic character. For comparison, the work function of Cu-NPs on ITO, which is known to be 4.7 eV [11], was also determined. The SKPFM and AFM images of Cu-NPs on ITO are shown in **Figure 3.3(d)** and **(e)** respectively. Their work function

vs. particle diameter extracted from SKPFM is plotted in **Figure 3.3(f)** showing a decreasing trend in the work function of absorbed Cu-NPs with decreasing diameter, contrasting with the behavior for Cu-NP absorbed on graphene. The continuous line in Figure 3.3(f) indicates that the model given by eq. 3.2 satisfactorily fits our data.

3.4 Theoretical results

To gain insight into the effects on the band structure of graphene domains as a consequence of local changes in their work function due to the presence of Cu-NPs, a theoretical framework was developed by Dr. Arash Akbari-Sharbaz in a collaboration between our research group and Prof. M. Cottam's theoretical research group at Western University. Their theoretical model is based on a modified tight-binding model written in second quantization [26]. The tight-binding Hamiltonian describing the π -electron system of graphene in the absence of Cu-NPs is given by

$$H = \sum_{i,s} \varepsilon_i c_{i,s}^+ c_{i,s} + \sum_{i,j,s} t_{i,j} c_{i,\sigma}^+ c_{j,s}, \quad (3.3)$$

where c^+ (c) indicates a creation (annihilation) fermionic excitation operator, ε_i is the ionization energy corresponding to the local work function at a lattice site i , t_{ij} is the hopping integral between nearest-neighbor sites i and j , and s is the spin projection index. Cu-NPs were incorporated in our model by introducing a modified tight-binding potential ΔU_{mod} for sites in contact with the particles. We therefore assume that interaction between C and Cu atoms takes place within a specific contact region in which the tight-binding potential is affected and modifies the diagonal (ε_i) and off-diagonal (t_{ij}) matrix elements of the Hamiltonian. We label these modified diagonal and off-diagonal elements by ε_{mod} and t_{mod} , respectively, which correspond to carbon sites interacting with Cu. The unaffected interactions corresponding to the

local ionization potential and nearest-neighbor interaction energy of bare carbon sites in graphene are labeled with ε_0 and t_0 . The eigenvalues of the modified Hamiltonian matrix were thus determined and the changes in the work function of graphene as a consequence of the modifications of the tight-binding potential were calculated.

Results indicate that the introduction of modified off-diagonal elements in the Hamiltonian matrix generates shallow electronic states for $t_{mod} < t_0$, as seen in **Figure 3.4(a)**, and deep states for $t_{mod} > t_0$, as seen in **Figure 3(b)**. These states appear symmetrically in both the valence and conduction band of graphene domains decorated with Cu. Consequently, the graphene Fermi level is unaffected by the appearance of these states because the electron-hole symmetry is preserved in the band structure. However, when specific diagonal elements are modified with $\varepsilon_{mod} \neq \varepsilon_0$, asymmetric states are generated either in the conduction band, for $\varepsilon_{mod} > \varepsilon_0$ as in **Figure 3.4(c)**, or in the valence band, for $\varepsilon_{mod} < \varepsilon_0$ as in **Figure 3.4(d)**, thereby breaking the electron-hole symmetry and shifting the graphene work function and Fermi level. If all sites on the graphene lattice were modified in the same way, the diagonal matrix elements in the Hamiltonian would be identically equal to ε_{mod} and to the Fermi energy at the Dirac point, with no doping effect and in apparent contradiction with the results of Giovannetti *et al.* [12], indicating that a uniform distribution of Cu on graphene moves the graphene Fermi level into the conduction band, which leads to n-type doping and charge injection. In fact, even for a uniform Cu distribution, graphene doping [12] can be well understood in the framework of our tight-binding model as the result of two different ionization energies, $\varepsilon_i = \varepsilon_0$ and $\varepsilon_j = \varepsilon_{mod}$, for two homogeneously distributed but nonequivalent subsets, $\{i\}$ and $\{j\}$, of C sites interacting and non-interacting with Cu, with a fraction of $\{j\}$ -type sites much lower than $f_j = 50\%$.

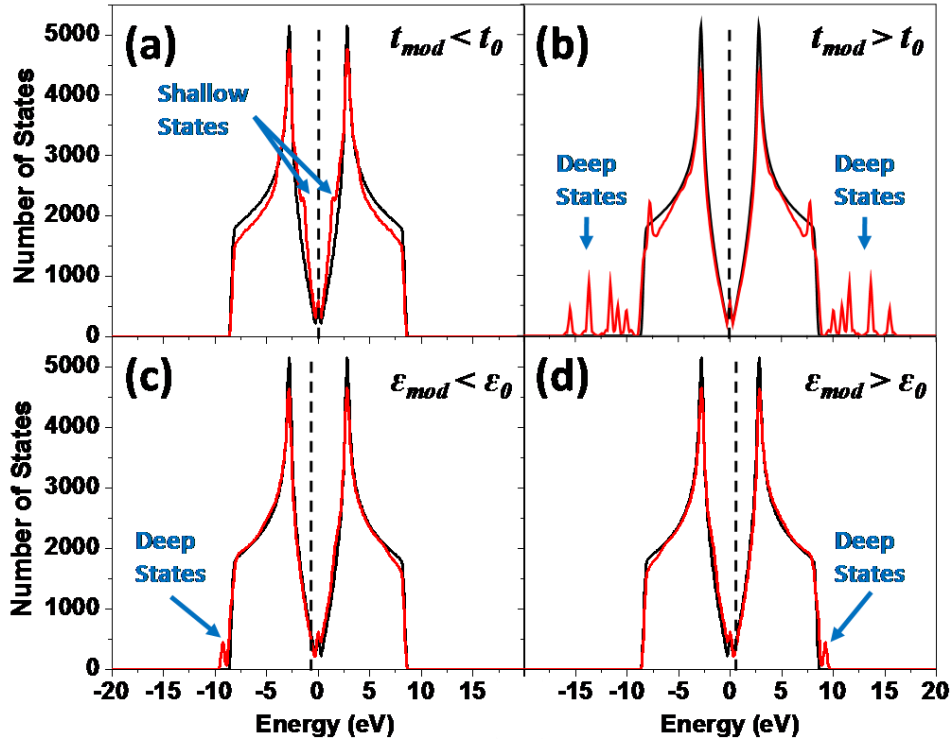


Figure 3.4: Electronic density of state (DOS) calculated for a bare graphene flake of dimensions 80×80 rings (black trace) and graphene covered with 59 Cu-NPs with radius $r = 3a$ distributed randomly (red trace). Panels (a)-(d) illustrate the dependence of the DOS on the modified diagonal and off-diagonal matrix elements. (a) $t_{mod} = 0.5t_0$, generating shallow states near the Fermi level, (b) $t_{mod} = 2t_0$, generating deep states symmetrically in the valence and conduction bands. (c) Effect of a positive $\Delta\varepsilon = \varepsilon_{mod} - \varepsilon_0 = 0.3$ eV on the DOS, generating states in the valence band, and (d) Effect of a negative $\Delta\varepsilon = \varepsilon_{mod} - \varepsilon_0 = -0.3$ eV, generating states in the conduction band. Both situations c and d are breaking the electron-hole symmetry.

In order to investigate the influence of different copper nanoparticle distributions on the work function of graphene, we randomly generated specific small clusters of $\{j\}$ -type C sites on a 200×200 atom graphene layer, as demonstrated in **Figure 3.5(a)** and (b). In the first

distribution, illustrated in panel (a), 59 clusters of C sites interacting with Cu of diameter $D = 0.85$ nm were randomly positioned on the graphene lattice. In the second distribution, illustrated in panel (b), a single, but larger, cluster of radius $D = 6.5$ nm was placed at the center of the same graphene domain.

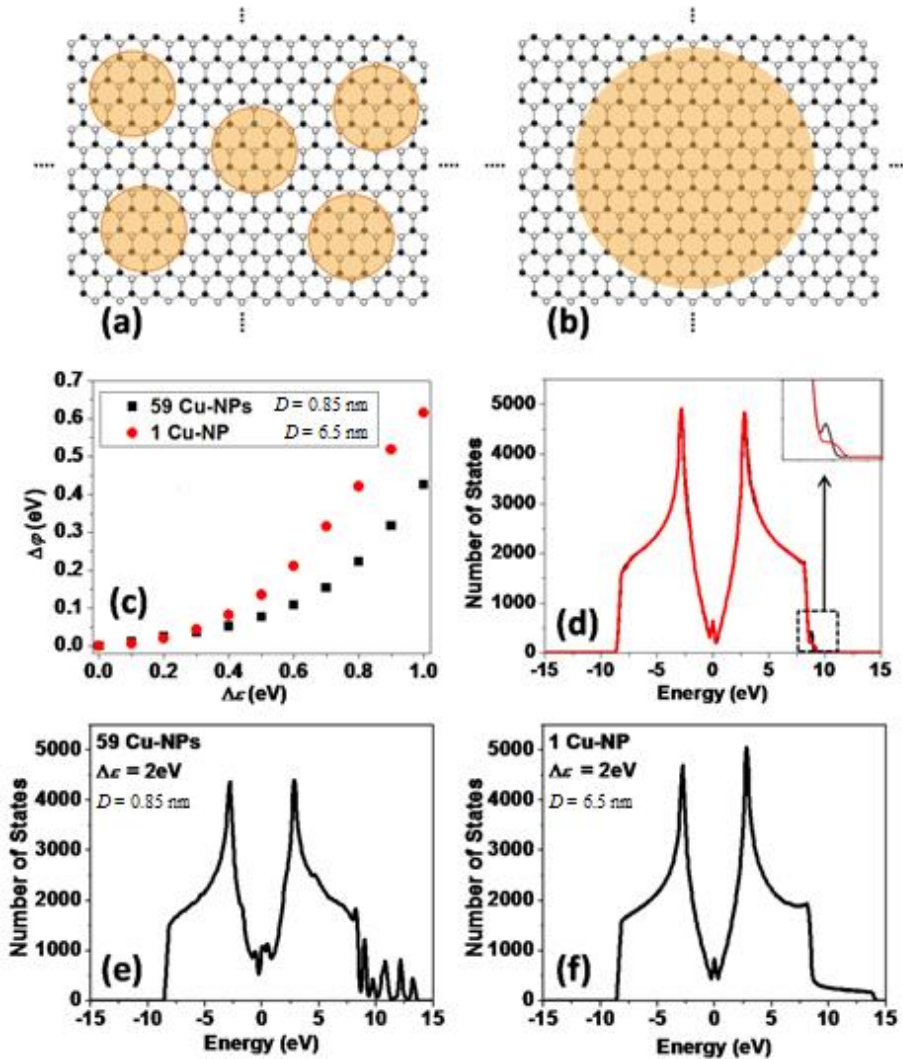


Figure 3.5: Schematic representation of superlattices of (a) 59 Cu-NPs of $D = 0.85$ nm diameter distributed randomly on a graphene lattice and (b) 1 Cu-NP of $D = 6.5$ nm (both with $f_j = 20\%$) (c) Calculated shift in the work function vs. $\Delta\epsilon$ for the two distributions in panels a (black trace) and b (red). (d) The density of states for the two distributions indicated in panels a (red) and b (black) assuming $\Delta\epsilon = 0.3$ eV. (e) and (f) show the DOS for the two distribution at $\Delta\epsilon = 2$ eV.

For the subset of $\{i\}$ -type C sites not interacting with Cu, typical tight-binding parameters for sp^2 C systems ($\varepsilon_0 = 4.58$ eV and $t_{ij} = 2.87$ eV [27]) were assumed. The area fraction covered by Cu-NPs, $f_j = 20\%$, was nearly the same for both distributions in Figures 3.5(a) and 3.5(b). A plot of the work-function shift as a function of the difference, $\Delta\varepsilon = \varepsilon_{mod} - \varepsilon_0$, of the local ionization energy of $\{i\}$ -type and $\{j\}$ -type C sites is reported in **Figure 3.5(c)**. For relatively low energy difference between the Dirac point of graphene and the work function of metallic nanoparticles, thus for $\Delta\varepsilon = \varepsilon_{mod} - \varepsilon_0 < 0.3$ eV, the shift in the work function of graphene away from the Dirac point is about the same for both distributions. For $\Delta\varepsilon > 0.3$ eV, the differences in $\Delta\phi$ between the two systems become more important, which indicates that, at a stronger metal-carbon bonding, the particle diameter plays a more significant role in shifting the work function away from the Dirac point of graphene, in addition to the major role played by the area fraction covered by metallic particles.

3.5 Comparison and discussion of theoretical and experimental results

The role played by the Cu-NP diameter at high values of $\Delta\varepsilon$ can be understood by examining its effects on the π -electron density of states (DOS) of graphene. At small $\Delta\varepsilon$ the DOS is only marginally different for the two distributions of Cu shown in Figures 3.5(a) and 3.5(b), as demonstrated in Figure 3.5(d). Conversely, an important feature of the DOSs at high energy differences between the Dirac point of graphene and the work function of metallic nanoparticles, shown in Figure 3.5(e) and (f), is that they are significantly affected by the particle size. If very small particles are randomly distributed on the graphene lattice, as demonstrated in panel (a), the DOS near the Fermi level is dramatically altered in its profile, compared to pristine graphene. However, even at the largest values of $\Delta\varepsilon$, the DOS profile near the Dirac point is preserved for

large metallic nanoparticles, as demonstrated in panel (b) for $D = 6.5$ nm, and arguably even at larger diameters. This suggests that for particles of $D > 10$ nm, such as those used in our experiments, the metal particle diameter plays a negligible role over the covered area fraction in determining the work-function shifts of graphene domains.

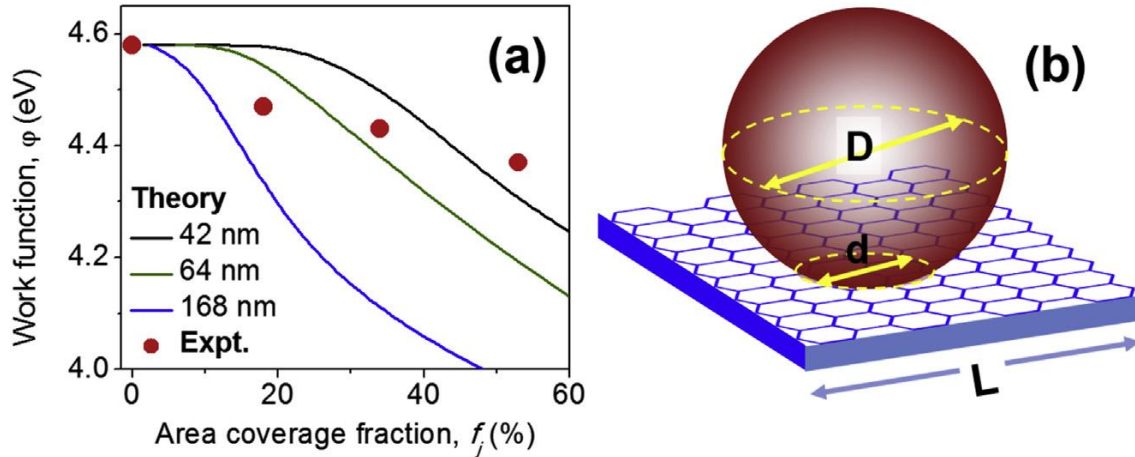


Figure 3.6: (a) Comparison of tight-binding (solid lines) and experimental (dots) trends of the work function of graphene as a function of area coverage by Cu-NPs. (b) Model for Cu-NPs with contact diameter, d , different from the maximum particle diameter.

These theoretical findings corroborate our SKPFM experiments indicating that the Cu-NP diameter has a very moderate, if any, effect on both $\Delta\phi$ and the electrical conductivity, σ , which suggests $\Delta\epsilon < 0.3$ eV. Specifically, our theoretical model [see Fig. 3.5(c)] suggests that work function shifts of $\Delta\phi = 0.2$ eV at $f_j = 20\%$ as shown in **Figure 3.6(a)** are consistent with $\Delta\epsilon = 0.1$ eV, compatible with a relatively weak interaction between Cu-NPs and graphene. Conversely, our experiments show that the graphene area fraction covered by Cu-NPs appears to have a more important effect on $\Delta\phi$, as demonstrated in Figure 3.6(a). Our tight-binding simulations,

performed at $\Delta\varepsilon = 0.1$ eV, indicate that $\Delta\phi$ is decreasing at increasing f_j , even though the decreasing rate is strongly depending on the graphene domain size, L . Three different theoretical curves of $\Delta\phi$ as a function of f_j are shown in Fig. 5(a), for $L = 42$ nm, $L = 64$ nm and $L = 168$ nm, respectively, and show that the decrease is more significant at larger L . Each curve is obtained from the interpolation of a number of simulations. The experimental values of $\Delta\phi$, determined by SKPFM, are also reported in the same figure and show a decreasing trend as a function of the Cu-NP area coverage. Although the flake diameter (up to a few μm) in our graphene based thin films is generally larger than the values of L used in our simulations, it can be observed that several reasons may be invoked to quantitatively reconcile our theoretical predictions and SKPFM data, which both qualitatively indicate the decrease of $\Delta\phi$ with f_j .

One of such reasons is the presence of wrinkles in graphene flakes, which are clearly visible in both panels a and b of Figure 3.3. Wrinkles break the continuity of graphene flakes and limit the delocalization of π -electrons. Consequently, in graphene flakes with wrinkles, it is more realistic to assume that the values of L introduced in our theoretical tight-binding calculations should be compared to the distance between neighbor wrinkles on a graphene flake, instead of the flake side or diameter. Wrinkle distances of a few tens nm appear to be consistent with those that can be experimentally observed in Figure 3.3(a) and decrease as the Cu-NP coverage increase and flakes become more corrugated, which could explain why SKPFM experiments at $f_j = 34\%$ are consistent with theoretical values of L between 42 nm and 64 nm while higher values of L , between 64 nm and 168 nm are required to reconcile our theoretical and experimental values for $f_j = 18\%$. Another reason that may lead to discrepancies between experimentally and theoretically determined values of $\Delta\phi$ is that graphene-based thin films lead to the overlap of few-layered graphene flakes to form a continuous pathway between them, while our set of tight-

binding simulations was performed on single-layer domains. It may be expected that the interaction between Cu-NPs and graphene is stronger for the upper layer of a few-layer graphene stack, while its strength exponentially decays for the underlying layer due to electron screening effects, for which $\Delta\varepsilon$ will be lower in few-layer graphene flakes and when two juxtaposed flakes overlap.

Another key factor that may be invoked to quantitatively reconcile our theoretical and experimental results is the fact that AFM and SKPFM tend to overestimate the Cu-NP diameters. Specifically, the diameter detected by AFM is the maximum diameter of the nanoparticles (referred as D in Figure 3.6(b)) while the area coverage is determined by the contact diameter (indicated as d in Fig. 3.5 (b)). Dewetting of Cu on graphene has been extensively studied [28] and it has been found that, under equilibrium conditions, the contact angle between Cu-NPs and graphene may be up to 150° , with a d/D ratio of 2. We used this value to adjust our theoretical results by determining the area coverage with d as the Cu-NP diameter, with our experimental values of area coverage assuming D as the Cu-NP diameters. The x-axis scale of Figure 3.6(a) refers to the experimentally measured values of f_j with the values of the theoretical calculations adjusted to them. Summarizing our theoretical and experimental findings, it is apparent they concur in indicating that the Cu-NP area coverage is more important than the Cu-NP diameter in affecting the work function of graphene.

Similar trends on both $\Delta\phi$ and σ as a function of the Cu-NP area coverage can be noticed from the comparison of **Figure 3.7(a)** and (b). Consequently, a relationship between $\Delta\phi$ and σ , shown in **Figure 3.7(c)**, can be inferred and may be understood assuming a Poole-Frenkel model [29] for π -electrons of graphene localized in the proximity of Cu-NPs, their detrapping at moderate electric field E , and their subsequent diffusion within the graphene lattice.

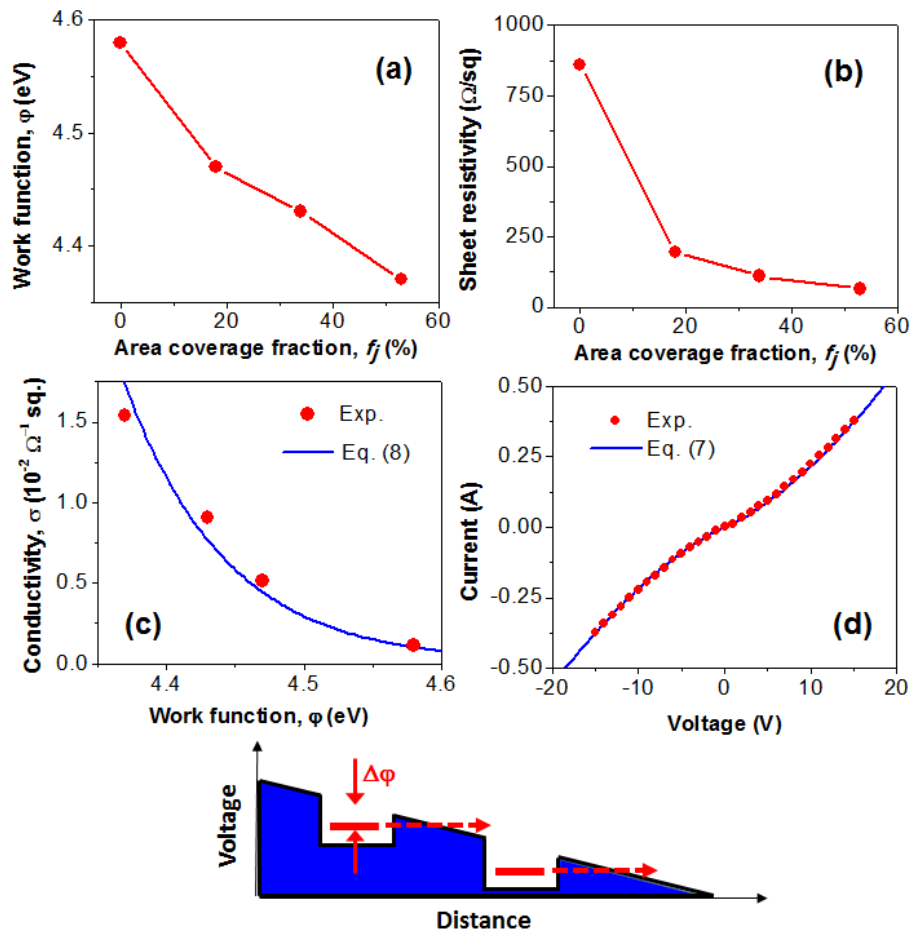


Figure 3.7: (a) Relationship between work function and area coverage fraction and (b) relationship between electrical resistivity and area coverage fraction for a set of graphene films decorated by Cu-NPs at a constant diameter $D \approx 20$ nm. (c) Relationship between work function and electrical conductivity obtained by combining the data in panel a and b, which is excellently reproduced by the Poole-Frenkel model as in eq. (3.5). (d) Example of fit of J-V characteristic in using eq. (3.4). (e) Poole-Frenkel model for detrapping at moderate electric fields of π -electrons localized in the proximity of metallic nanoparticles.

As discussed previously in Section 1.2.4.1 of Chapter 1, Poole-Frenkel model leads to the following relationship between the field and the current density J flowing through a system of electron traps disseminated within a less conducting medium:

$$J = \sigma_0 E \exp\left[\frac{-q^* \Delta\varphi + q^{*3/2} \pi^{-1/2} (E/\varepsilon_m)^{1/2}}{k_B T}\right] \quad (3.4)$$

where σ_0 is a prefactor that corresponds to the sheet conductivity of the bare graphene film without Cu-NPs, for which $\sigma_0 = 0.015 \Omega^{-1} \square$, q^* is the dynamic effective charge of the carriers trapped on graphene in the proximity of a Cu-NP, ε_m is the medium dielectric permittivity and $k_B T = 0.025$ eV in our case for room temperature. **Figure 3.7(d)** shows that eq. (3.4) fits our data extremely well with $q^* = 0.34q$ and $\varepsilon_m = 3.0$ when graphene is decorated with Cu-NPs. Conversely, an ohmic trend was found in the entire ± 15 V range for bare graphene-based films.

The Poole-Frenkel mechanism, depicted schematically in **Figure 3.7(e)**, indicates that the probability of carriers to tunnel between traps is weakly dependent on the local electric field E/ε_m inside the graphene medium, provided that field is sufficiently low. Only under such low-field conditions, which figure 3.7(d) indicates to be fulfilled at less than ± 2 V, the film electrical properties are ohmic even in the presence of Cu-NPs. In this case, the relationship between J and E assumes Ohm's linear form $J = \sigma E$, in which the conductivity can be written as [29].

$$\sigma \approx \sigma_0 \exp(-q^* \cdot \Delta\varphi / k_B T). \quad (3.5)$$

Figure 3.7(c) shows that eq. (3.5) reproduces with no adjustable parameters our set of data recorded on graphene-based thin films at variable area fraction covered by Cu-NPs, since the value used for q^* is the same inferred from Figure 3.7(d). Consequently, the comparison of our theoretical and experimental results suggests that the increase in electrical conductivity obtained upon decoration of graphene thin films by metallic nanoparticles is a mechanism profoundly

different from the process with large and flat metallic contacts, described by Giovannetti *et al.* [12], which requires chemical bonding between carbon and a metal to effectively dope graphene.

Eq. (3.4) shows that decoration of graphene thin films with metallic nanoparticles leads to an electronic process for which only at low enough electric fields an activation energy for the electrical conductivity can be defined via eq. (3.5), equivalently to what is done in ref. [12]. These differences require a completely different theoretical treatment of the interface between metallic objects and graphene at the nanoscale, as thoroughly discussed in section 3.3.2. On the other hand, the superlinear increase in current density as a function of the applied voltage ensured by the Poole-Frenkel mechanism suggests that metallic nanoparticles are more effective than large metallic contacts in improving graphene-based thin films as electrical conductors.

3.6 Conclusion

In this chapter, we developed the physical framework for understanding graphene doping by metallic nanoparticles. We show that large contacts are less effective at modifying the band structure of graphene in comparison with an ensemble of many particles randomly distributed on the graphene surface. A modified tight-binding model has been utilized to complement our experimental results and to investigate the influence of Cu-NPs on the band structure and work function of graphene-based thin films. Local variations in the graphene work function due to the presence of Cu- NPs break the electron-hole symmetry of graphene shifting the Fermi level away from the Dirac point, effectively doping graphene even in the absence of charge transfer or chemical bonding. Theoretical calculations have been reported here for completeness, and are in good agreement with our SKPFM experiments. Our combined experimental and theoretical study

shows that Cu-NP area coverage is the most important factor in controlling the decrease of the work function of graphene in the presence of Cu, as well as the subsequent decrease in electrical resistivity. We also demonstrate that the electrical transport of graphene-based thin films in the presence of Cu-NPs is controlled at room temperature by a Poole-Frenkel mechanism.

A unique advantage conferred by Cu-NP doping is evident when we compare the electrical conductivity of doped and undoped graphene thin films. For a graphene film with $f_j = 18\% \pm 5\%$ area coverage of Cu-NPs, the transmittance reduces by only $\sim 9\%$, while its conductivity increases by more than 400%. In addition to the enhanced conductivity and the preservation of transparency, the presence of Cu-NPs gives rise to surface plasmons, which can be used for wide range of applications, including transparent electrodes in plasmonically enhanced thin film solar cells [19] and surface-plasmon sensors.

References

- [1] S. Bae, H. Kim, Y. Lee, X. Xu, J.S. Park, Y. Zheng. *Nature Nano* **2010**, 5, 574.
- [2] G. Jo, M. Choe, S. Lee, W. Park, Y.H. Kahng, T. Lee, *Nanotechnology* **2012**, 23, 112001
- [3] S.Y. Zhou, D.A. Siegel, A.V. Fedorov, A. Lanzara, *Phys. Rev. Lett.* **2008**, 101,086402
- [4] B. Guo, L. Fang, B. Zhang, J.R. Gong, *Insciencas J.* **2011**, 1, 80
- [5] J.H Chen, C. Jang, S. Adam, M.S. Fuhrer, E.D. Williams, M. Ishigami, *Nature Phys.* **2008**, 4, 377
- [6] K.I. Bolotin, K.J Sikes, Z. Jiang, M. Klima, G. Fudenberg, J. Hone, et al. *Solid State Comm.* **2008**, 146, 351
- [7] D.R. Dreyer, S. Park, C.W. Bielawski, R.S. Ruoff, *Chem. Soc. Rev.* **2010**, 39, 228
- [8] C. Liu, Z. Yu, D. Neff, A. Zhamu, B.Z. Jang, *Nano Lett.* **2010**, 10, 4863

- [9] Z. Yang, Z. Yao, G. Li, G. Fang, H. Nie, Z. Liu, et al. *ACS Nano* **2012**, 6, 205
- [10] Y. Wang, Y. Li, L. Tang, J. Lu, J. Li, *Electrochem. Commun.* **2009**, 11, 889
- [11] G. Eda, G. Fanchini, M. Chhowalla, *Nature Nano* **2008**, 3, 270
- [12] G. Giovannetti, P.A. Khomyakov, G. Brocks, V.M. Karpan, J. Van den Brink, P.J. Kelly, *Phys. Rev. Lett.* **2008**, 101,026803
- [13] A. Venter, M. Hesari, M.S. Ahmed, R. Bauld, M.S. Workentin, G. Fanchini, *Nanotechnology* **2014**, 25, 135601
- [14] F. Sola, J. Niu, Z.H. Xia, *J. Phys. D: Appl. Phys.* **2013**, 46, 065309
- [15] N.A. Luechinger, E.K. Athanassiou, W.J. Stark, *Nanotechnology* **2008**, 19, 445201
- [16] I.V. Lightcap, T.H. Kosel, P.V. Kamat, *Nano Letters* **2010**, 10, 577
- [17] D. M. Wood, *Phys. Rev. Lett.* **1981**, 46, 749
- [18] I.D. Parker, *J. Appl. Phys.* **1994**, 75, 1656
- [19] S. Ezugwu, H. Ye, G. Fanchini, *Nanoscale*, **2015**, 7, 252
- [20] F. Sharifi, R. Bauld, M.S. Ahmed, G. Fanchini, *Small* **2012**, 8, 699
- [21] S. Ezugwu, *Synthesis and characterization of copper nanoparticles and copper-polymer nanocomposites for plasmonic photovoltaic applications*. MSc Thesis, Univ of Western Ontario, London, ON Canada **2012** (see also <http://ir.lib.uwo.ca/etd/1025>)
- [22] J. Park, D. Bang, K. Jang, S. Haam, J. Yang, S. Na. *Nanotechnology* **2012**, 23, 365705
- [23] O. A. Yeshchenko, I. M. Dmitruk, A. M. Dmytruk, A. A. Alexeenko, *Mat. Sci & Eng B* **2007**, 137, 247
- [24] U. Pal, H. A. Bautista, L. Rodriguez-Fernandez, J. C. Cheang-Wong, *J. Non-Cryst Solids* **2000**, 275, 65
- [25] A. H. Castro Neto, F. Guinea, N. M. R. Peres, K. S. Novoselov, A. K. Geim. *Rev Mod*

Phys. **2009**, 81, 109.

- [26] A. Akbari-Sharbat, *Defect-related magnetic and electronic properties of Graphene*. PhD Thesis, Univ of Western Ontario, London ON Canada **2014** (see also <http://ir.lib.uwo.ca/etd/2441/>)
- [27] T. B. Boykin, M. Luisier, G. Klimeck, X. Jiang, N. Kharche, Y. Zhou, et al. *J Appl Phys* **2011**, 109, 104304
- [28] M. Fuentes-Cabrera, B. H. Rhodes, J. D. Fowlkes, A. Lopez-Benzanilla, H. Terrones, M. L. Simpson, *Phys. Rev. E*, **2011**, 83, 041603
- [29] S. M. Sze, *Physics of semiconductor devices*. 2nd ed. Sect. 7.4.4. New York, Wiley **1998**.

Chapter 4

Thermal conductivity of Cu-NP decorated multi-layer graphene platelets

4.1 Introduction

A single-layer graphene sheet exhibits many outstanding properties such as ultrahigh thermal conductivity, high carrier mobility, optical transparency and mechanical strength [1-4]. Despite these remarkable features, the fabrication and manipulation of single-layer nanosheets represents an uphill challenge and limits extensive applications of graphene in devices. Instead, graphene-based thin films, comprising of many layers are attracting more technological interest than mostly single layer CVD graphene due to their low cost, processability on plastics substrates, and high scalability [3, 5-9]. While the use of multi-layer graphene circumvents the difficulty in manipulating a single-layer graphene, it also limits many of the outstanding properties observed only in single- and few-layers. For instance, experimental study revealed the room temperature thermal conductivity, k_{th} value for single layer graphene exceeding 5000 W/mK [10]. This value is substantially more than that of bulk graphite, which at room temperature is about 2000 W/mK. The reduction in the value of thermal conductivity from single to many layers indicates a strong dependence of K_{th} on the number of graphene layers [11]. Hence, there must be some trade-offs in optimizing the number of layers in order to fabricate graphene that could be easily manipulated and still retain, to appreciable levels, the outstanding properties of single layer. Such trade-offs will allow for increased use of graphene for heat evacuation in devices [11].

Recent attempts at enhancing the thermal conductivity of graphene-based thin films has lead to the fabrication of graphene-based composites using metallic nanoparticles and/or thin films to decorate graphene surface [12]. The incorporation of metallic nanoparticles on graphene

surface for the purpose of thermal management application is inspired by the improvement on the electrical properties of graphene-based thin films by metallic nanoparticles [13]. However, thermal transport in graphene-metal nanocomposites is expected to be more complicated and can not be interpreted purely on the basis of its electrical conductivity performance. While electrons are the principal elementary carrier for both the electrical and thermal transport in metals, lattice vibration play a major role in controlling thermal transport in carbon materials such as graphene [14]. As such, interfacial thermal transport between graphene-based thin films and the metallic nanoparticles is expected to play a key role in controlling the overall thermal performance of graphene – metal nanocomposites. While efforts are put into fabricating graphene – metal nanocomposites, it is not yet well understood how the materials parameters such as the number of layers of graphene-based platelets affects the overall thermal behaviour in these materials.

In this chapter, we investigate the influence of the addition of copper nanoparticles on the thermal properties of graphene-based thin films. Our target is to correlate the thermal properties of graphene-based platelet of different layer thicknesses with the thermal performance of the same platelet when decorated with Cu-NPs. This will enable us to study the role of interfacial thermal effects due to absorbed Cu-NPs on graphene-based platelets. The thermal conductivity of graphene-based thin films will be determined independently of copper nanoparticles by means of near-field scanning thermoreflectance imaging (NeSTRI) technique described in details in chapter two. Using this method, the thermal parameters such as the phase and amplitude of temperature profile; the topography and SNOM images are measured and recorded simultaneously. After the first measurement on graphene-based platelets, a second set of measurement is conducted on the same sample with absorbed Cu-NPs. It is expected that our measurement technique is sufficient to understand the influence of the metallic nanoparticles on

the thermal properties of graphene-based thin film at nanoscale level, as well as the impact of the number of layers of graphene on the thermal performance of the sample.

4.2 Methods

Graphene-based thin films were first prepared from 15 ml of suspension of graphene flakes obtained from freshly exfoliated nanographite in Ribonucleic acid (RNA) solution [3]. The film, which was deposited on a cellulose membrane by vacuum-filtration, was then transferred to BK7 glass substrate. The substrate loaded with graphene was baked overnight at 50°C, etched in a consecutive acetone and methanol baths (to eliminate the filter membrane), and subsequently annealed at 540 °C for 1 hr to eliminate residual RNA.

In order to obtain islands of graphene platelets for our thermal conductivity measurements, scotch tape method [15] was employed to transfer patches of graphene-based platelets to a new glass substrate. In our scotch tape method, graphene-based platelets are detached from pre-existing graphene-based thin films described above using adhesive Kapton™ tape. After taking the tape off the film, few- and multi-layer graphene remains on it. Cleaved graphene layers are subsequently attached to newly cleaned glass substrate by pressing the tape gently onto it. This process leaves isolated platelets on the substrate which we used for the thermal measurement. Island of graphene platelets are required in this particular study for easy identification, enabling re-use of same graphene-based platelets even after incorporation of nanoparticles on the surface.

We utilized multi-layered graphene-based platelets as our target sample aimed at assessing the performance dependence of the thermal interface on the number of graphene layers decorated with copper nanoparticles. In **Figure 4.1** (a), we show the AFM topography of a large

area graphene-based platelets that satisfy the requirements of multiplicity of layer and which has been used for our thermal measurements. The sample comprises of stacking of different number of layers on different regions labeled A – E, as indicated in the AFM topography. Figure 4.1 (b) gives the height profiles of some of the regions labeled in panel (a), from where the thicknesses of the layers can be determined, ranging from 5.1 nm to 27 nm. The histogram of the thickness and the associated number of layers are presented, respectively in panels c and d of Figure 4.1.

We carried out thermal measurements on the sample presented in Figure 4.1 using NeSTRI apparatus described in details in chapter two. The topography, SNOM images, thermorefectance amplitude and phase images of this sample were measured simultaneously using this apparatus. Two modulation frequencies of 105 Hz and 350 Hz were used for this study. Prior to the second thermal measurement, thermally evaporated [16]15-nm copper films were annealed at 350 °C for 2 hrs. in glove box which resulted to copper nanoparticles on the surface of graphene-based platelets. The sample, decorated with copper nanoparticles was re-measured in the same condition as without nanoparticles, including laser power, modulation frequencies, etc. In order to investigate defect related contributions to the measured thermal properties, Cu-NPs were etched from the surface of the graphene-based platelets in conc. HNO₃ for 30 minutes. The sample was rinsed thoroughly in deionized water, air-dried and re-measured using the NeSTRI apparatus, again under the same experimental conditions. From the experimental results, we determined the changes in the measured properties as a result of the incorporation/etching of Cu-NP onto/from our graphene-based samples.

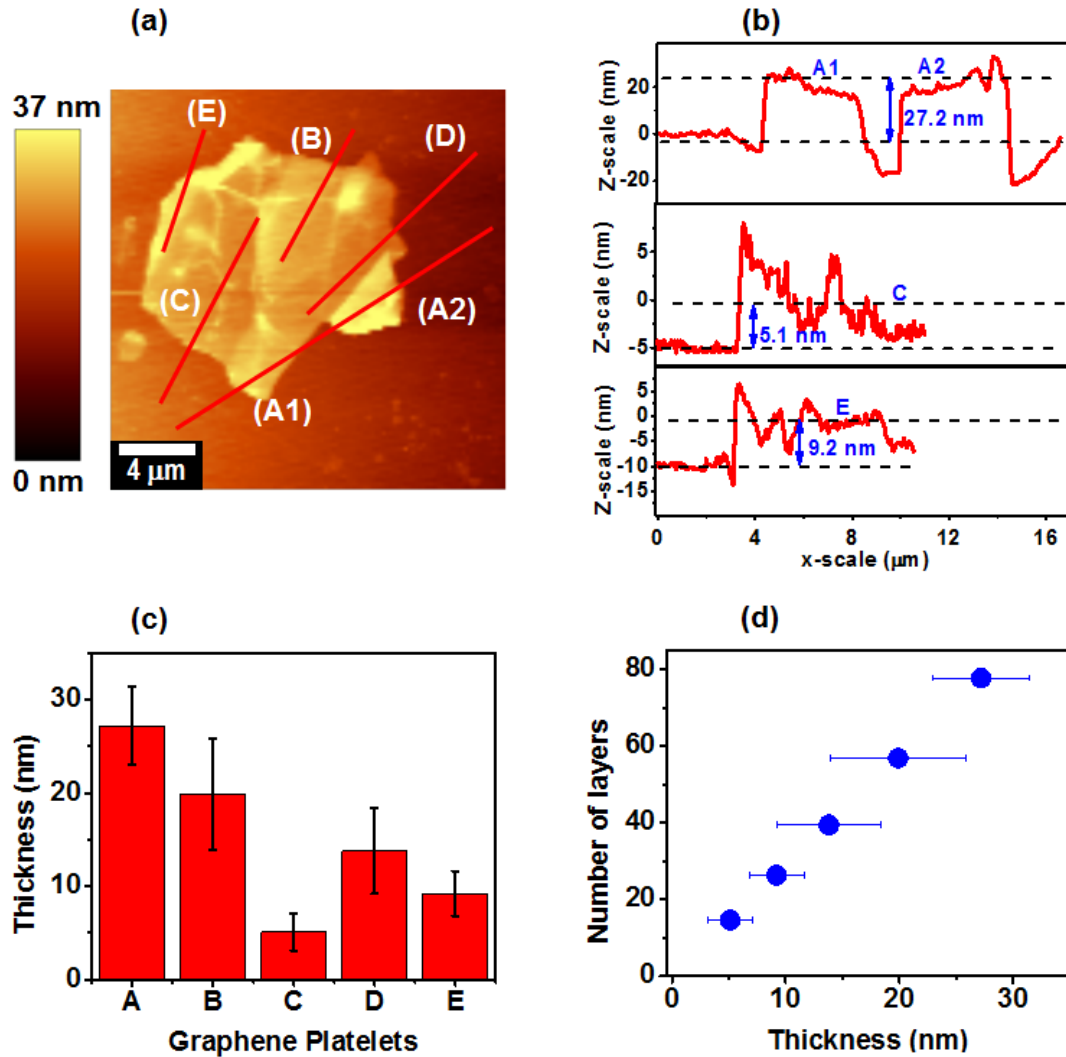


Figure 4.1: (a) AFM topography of graphene based platelets showing regions (A-E) of the platelets of different thicknesses. (b) The height profiles of regions A, C and E of the graphene-based platelets used to determine layer thicknesses. (c) Histogram of the thicknesses of the different regions of the graphene-based platelets indicated in (a) and (d) The calculated number of layers based on inter-layer thickness of $t = 0.35$ nm. The fact that the platelet has varied layer thicknesses makes it ideal for the present study, allowing to investigate interface performance with Cu-NPs.

4.3 Results and Discussion

4.3.1 Topography and SNOM transmittance and reflectance images

In **Figure 4.2**, we present the topography, SNOM transmittance and reflectance images of bare graphene-based platelets without Cu-NPs, with adsorbed Cu-NPs and after Cu-NPs etching. The topography shows that the adsorbed Cu-NPs comprising of different sizes are uniformly distributed on the surface of the platelets. Panel (c) indicates that the nanoparticles were not completely etched after 30 minutes in conc. HNO_3 . The figure also shows un-etched Cu-NPs, possibly copper oxides, exist mainly on the substrates and the graphene edges and very limitedly on the bulk even though a large number of Cu-NPs nucleated on the bulk, as demonstrated in panel (b). The preferential attachment of copper oxides on edges presumably indicates stronger bonding between the oxides and the graphene edges and may play significant role in controlling the thermal properties of the sample.

The SNOM transmittance images presented in panels (d) - (f) show that the transmittance images are clearly different before and after coating with Cu-NPs. Even by visual inspection, we notice a variation in the transparency according to number of layers of graphene domains shown in Figure 4.1, suggesting that SNOM transmittance decreases at increasing number of layers. When decorated with Cu-NPs, panel (e) shows that the transmittance of the substrate also decreases, consistently with light absorption by the nanoparticles nucleated on the substrate. Since we are interested in the region with graphene domains, we quantified the transmittance and reflectance of graphene domains in the SNOM images using the Witec software. We found, on average, that the transmittance from our graphene-based platelets decreases by $\sim 24\%$ with Cu-NPs incorporation, and $\sim 10\%$ after Cu-NPs etching. Similar analysis on the SNOM reflectance

images, shows that the change in the reflectance is only 4% between Cu-NPs coated and uncoated graphene-based platelets and 3% after Cu-NPs etching.

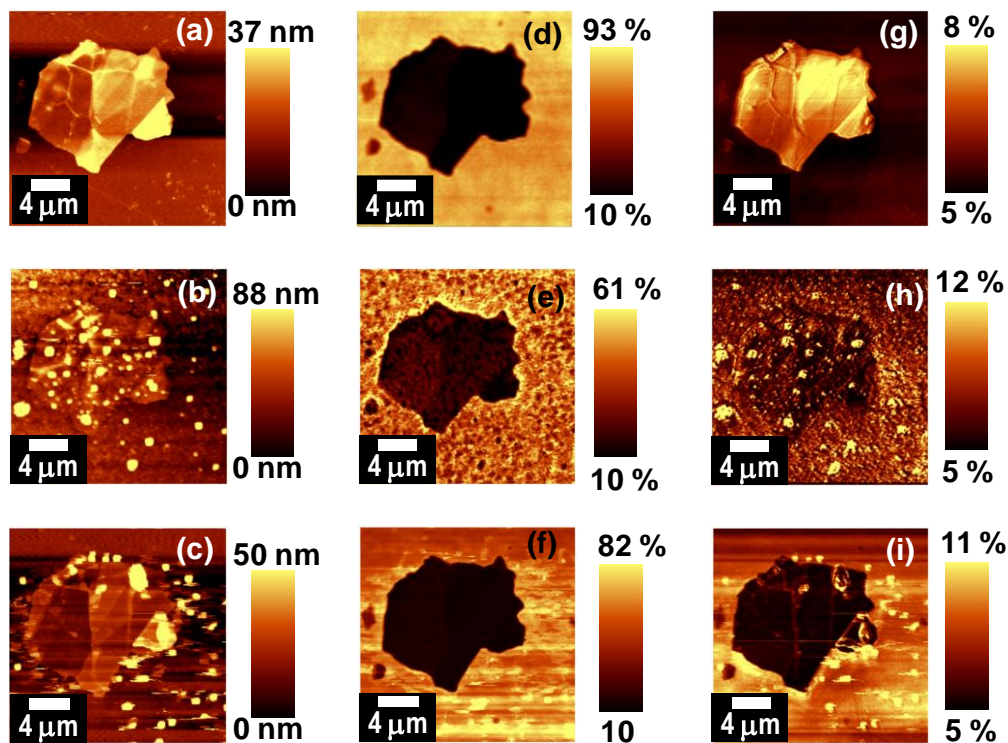


Figure 4.2: AFM topography of (a) bare graphene-based platelets with no Cu-NPs (b) the same graphene-based platelets decorated with Cu-NPs and (c) after etching Cu-NPs in conc. HNO_3 . The SNOM transmittance images of graphene-based platelets (d) without Cu-NPs (e) decorated with Cu-NPs and (f) after Cu-NPs etching. All the samples were deposited on glass substrate. The SNOM reflectance images obtained simultaneously during the NeSTRI measurements on the same graphene-based platelets (g) without Cu-NPs (h) with adsorbed Cu-NPs and (i) after Cu-NPs etching.

Since the differences in the transmittance data cannot be accounted for by the differences in the reflectance data, it can be seen that the incorporation of Cu-NPs on our graphene-based samples increases the absorption of laser light upon illumination. Highly absorbing region will also be

affected by high thermal load according to eq. 2.2 (see Section 2.1.3 in Chapter 2), we expect that heat generation in the sample can be increased by incorporating Cu-NPs on the graphene surface. In the following section, we present the result of our NeSTRI measurement of thermal parameters on the same sample discussed above.

4.3.2: NeSTRI images

Figure 4.3 is the result of our NeSTRI measurement on graphene-based thin films showing respectively, the thermal amplitude (top images) and phase (bottom images) of the thermorefectance oscillations obtained at 105 Hz modulation of pump beam. Although the amplitude image from the sample decorated with Cu-NPs is not as distinct as similar images recorded on pure graphene-based platelets and the same sample after Cu-NPs etching, the z-scale shows that the amplitude of the thermorefectance oscillation that can be measured in the presence of Cu-NPs is significantly high. The fact that we can not distinguish distinctively the graphene domain in the image of panel (c) is an indication that thermal conductivity of graphene platelets decreases with Cu-NPs. In order to better understand the effect of Cu-NPs, we quantified the changes in the thermorefectance oscillation amplitudes and phases, for different graphene layers shown in Figure 4.1, using the following relation:

$$\Delta\rho = \frac{\delta\rho_1 - \delta\rho_0}{\delta\rho_0} \quad \text{and} \quad \Delta\varphi = \frac{\delta\varphi_1 - \delta\varphi_0}{\delta\varphi_0} \quad (4.1)$$

where $\delta\rho_1$ and $\delta\varphi_1$ are respectively the amplitude and phase of thermorefectance oscillations experienced by the probe beam due to periodic heating of air from graphene-based platelets decorated with Cu-NPs, and $\delta\rho_0$ and $\delta\varphi_0$ are the recorded amplitude and phase without Cu-NPs. Similar calculation can be obtained after Cu-NPs etching by replacing 1 in the above

equation with 2. The result of this calculation is present in **Figure 4.4**. $\Delta\rho_I$ show that the amplitude decreases with the number of layers of graphene-based platelets in the presences of Cu-NPs. No clear trend can be obtained in the case of $\Delta\rho_2$ calculated from etched Cu-NPs.

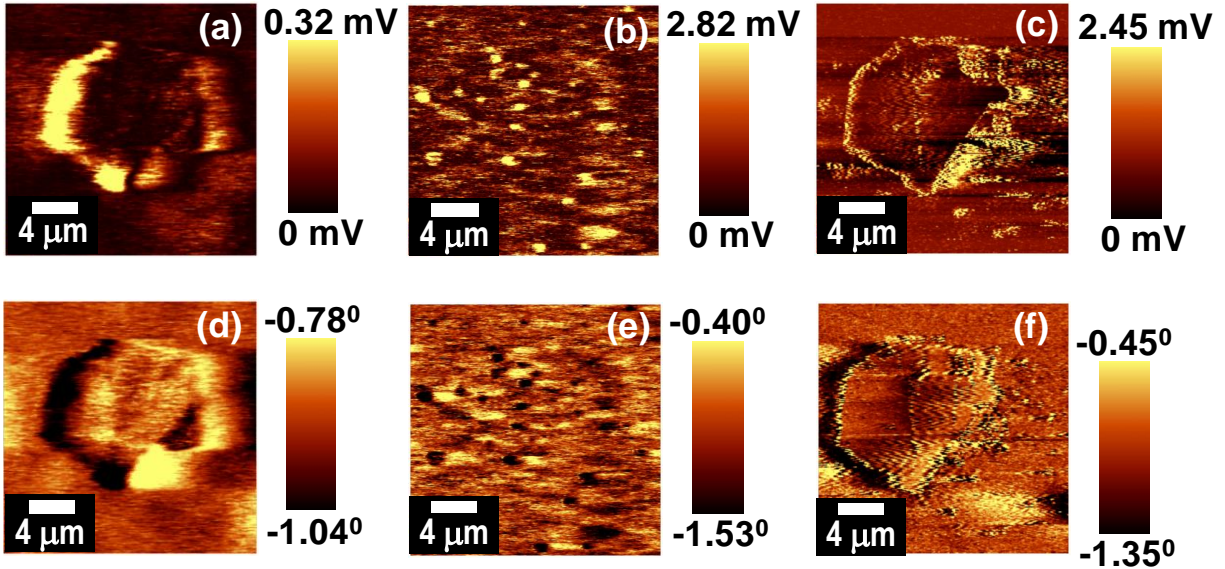


Figure 4.3: Simultaneously measured thermal amplitude and phase images of thermoreflectance oscillation. The amplitude images were measured from the same graphene-based platelets (a) without Cu-NPs (b) decorated with Cu-NPs and (c) after Cu-NPs etching. The phase images are from the same sample (d) without Cu-NPs (e) decorated with Cu-NPs and (f) after Cu-NPs etching.

Since the amplitude data represent small changes in reflectivity of the probe beam directly measured in our NeSTRI setup, the observed changes in $\Delta\rho$ is an indication of the changes in the reflectivity due to dissipation from the sample upon laser illumination. When the changes in the reflectivity is strong due to more dissipation, the measured amplitude is expected

to be higher and the reverse is also true. The decreasing trend of $\Delta\rho_1$ observed in panel (a) of figure 4.4 is a clear manifestation of the contribution to the thermal amplitude due to Cu-NPs. We observe in this figure significantly higher amplitude when the number of layers is, $N \leq 40$ layers. Since the amplitude of NeSTRI signal at a constant absorption coefficient of a sample is proportional to the thermal conductivity, it can be concluded that at $N \leq 40$ layers, Cu-NPs decorated graphene-based platelets is more thermally conducting than defect induced changes in the thermal amplitude after Cu-NPs etching.

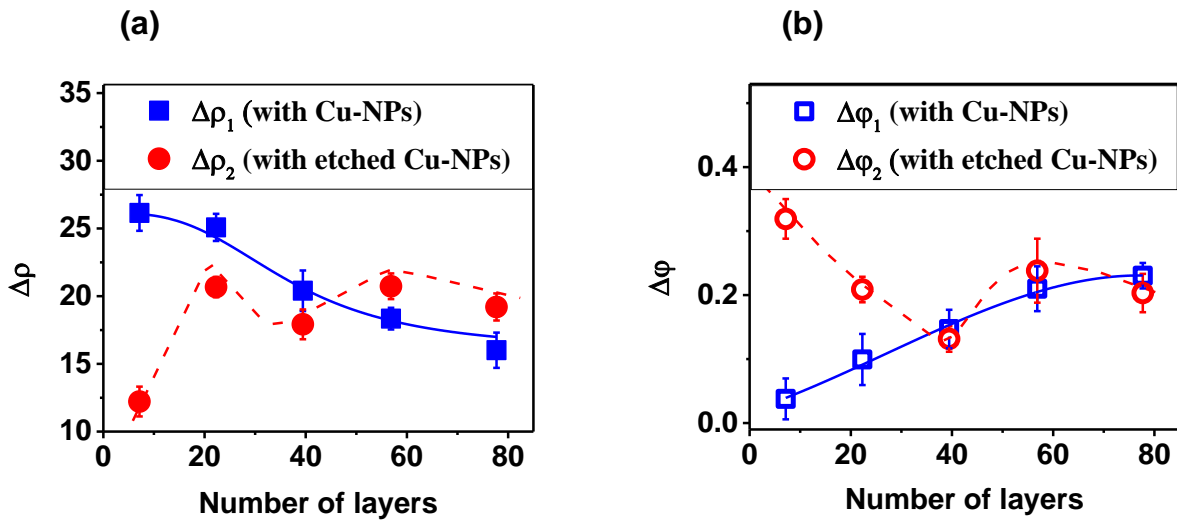


Figure 4.4: (a) Changes in thermorefectance oscillation amplitudes as a function of the number of layers. $\Delta\rho_1$ was obtained from the difference between the amplitude of graphene-based platelets decorated with Cu-NPs and the amplitude of same sample without Cu-NPs. $\Delta\rho_2$ is the difference between the amplitude of graphene-based platelets after Cu-NPs etching and the amplitude of same sample prior to Cu-NPs deposition. (b) The variation of the measured changes in the phase of thermorefectance oscillation with the number of layers of graphene-based platelets. Differences in phase are measured with respect to value of pure graphene-based platelets.

The fact that the sample is more thermally conducting in the presence of Cu-NPs with $N \leq 40$ layers is further confirmed when we consider the change in the amplitude $\Delta\rho_2$ determined after Cu-NPs etching. Although Cu-NPs can interact only weakly with graphene when nucleated on graphene surface [17] Cu-NPs assisted etching has been demonstrated to create pores and defect in graphene-based thin films [18]. Consequently, Cu-NPs etching from the surface of our graphene based platelets is expected to introduce defects such as pinholes and cracks that can strongly influence its thermal properties by acting as trap and scattering centres for phonon [19, 20]. In our sample, these traps lower the thermorefectance oscillation amplitude, and consequently the thermal conductivity of the graphene-based thin films in the region in which the number of graphene layer is less than 40. Low value of $\Delta\rho_1$ observed in the smallest graphene layer ($N \approx 7$) indicates that the pinhole that can be induced on graphene upon Cu-NPs etching is of the order of 6-8 nm. This can be the reason why the effects of defect induced changes is less significant at high number of graphene layer.

In panel (b) of Figure 4.4, the phase of thermorefectance oscillation increases with the number of graphene layer in the case of $\Delta\varphi_1$ suggesting that temperature profile exhibits higher phase delay in the region of higher number of graphene layers. Conversely, $\Delta\varphi_2$ decreases to lowest value at $N = 40$, before increasing with increasing number of layer. These results show that heat diffuses faster, with less phase delay when Cu-NPs is decorated on few layer graphene while the presence of pinhole and defects introduces large phase delay by limiting the heat propagation rate across the sample.

In **Figure 4.5**, we show the variation of the thermorefectance oscillation amplitude due to Cu-NPs decorated graphene-based platelets as a function of the diameter of the nanoparticles. It can be observed from this image that the amplitude increases with the average particle

diameter. This can be attributed to more heat dissipation resulting from higher absorption of pump laser beam. Another explanation can be made of the observed trend in the amplitude data presented in Figure 4.5 by considering the thermal interface effects due to the size of the absorbed Cu-NPs. Better thermal coupling between the graphene-based platelets and the nanoparticles can result in improved thermal conductivity of the composites, which as we indicated above will lead to higher amplitude of the thermoreflectance oscillation. The fact that the measured amplitude increases with the size of the nanoparticles can also be indicative that interfacial resistance could be lowered by increasing the size of the metallic nanoparticles. Thus, by using nanoparticles of sizes of the order of few nanometer, interfacial thermal effects will be significantly higher which will lead to very low thermal amplitude and consequently lower thermal conductivity. This can presumably be responsible for the previously observed decrease in the thermal conductivity of few layer graphene decorated with Au-NPs [21].

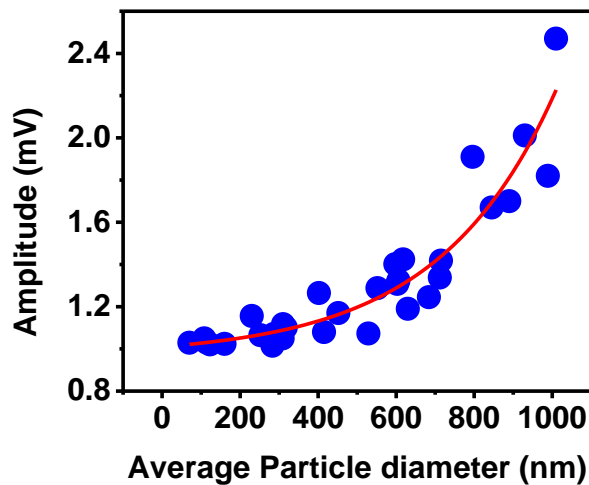


Figure 4.5: Variation of thermoreflectance amplitude with Cu-NPs diameter. The change in amplitude with the size of NPs is indicative of possible size effects in lowering interfacial thermal resistance at increasing particles size.

4.4 Conclusion

In this chapter, we used the NeSTRI set-up to image the amplitude and phase of thermoreflectance oscillation due to heat generated and dissipated by graphene-based platelets consisting of different number of layer, ranging from 7 to 75 layers. The same graphene sample was studied when decorated with Cu-NPs and after Cu-NPs etching in conc. HNO₃ for 30 minutes. The SNOM optical images showed lower transparency of graphene-based platelets in the presence of Cu-NPs that increased significantly upon Cu-NP etching. Our NeSTRI measurements shows that Cu-NPs is more suitable at enhancing the nanoscale thermoreflectance oscillation amplitude than Cu-NPs etching induced defects in the same sample.

Reference

- [1] A. A. Balandin, *Nat. Mater.*, 2011, **10**, 569.
- [2] K.S. Novoselov, A.K. Geim, S.V. Morozov, D. Jiang, Y. Zhang, S.V. Dubonos, I.V. Grigorieva, and A.A. Firsov, *Science*, 2004, **306**, 666.
- [3] F. Sharifi, R. Bauld, M. S. Ahmed and G. Fanchini, *Small*, 2012, **8**, 699.
- [4] Q. Peng C. Liang, W. Ji and S. De, *Phys. Chem. Chem. Phys*, 2013, **15**, 2003.
- [5] M. Kato, K. Uki, S. Harako and X. Zhao, *Microelectronic Engineering*, 2014, **121**, 96
- [6] J. S. Park, S. M. Cho, W. J. Kim, J. Park and P. J. Yoo, *ACS Appl. Mater. Interfaces*, 2011, **3**, 360
- [7] G. Eda, G. Fanchini and M. Chhowalla. *Nature Nano* 2008, **3**, 270

- [8] X. Lin, P. Liu, Y. Wei, Q. Li, J. Wang, Y. Wu, C. Feng, L. Zhang, S. Fan and K. Jiang, *Nat. Commun.*, 2013, **4**, 2920.
- [9] F. Pashaee, F. Sharifi, G. Fanchini and F. Lagugne-Labarthe, *Phys. Chem. Chem. Phys.*, 2015, **17**, 21315.
- [10] A. A. Balandin, S. Ghosh, W. Bao, I. Calizo, D. Teweldebrhan, F. Miao and C. N. Lau, *Nano Letters*, 2008, **8**, 902.
- [11] E. Pop, V. Varshney and A. K. Roy, *MRS Bull.*, 2012, **37**, 1273.
- [12] J. Wang, L. Zhu, J. Chen, B. Li, J. T. L. Thong, *Adv. Mater.* **2013**, 25, 6884
- [13] A. Akbari-Sharbaf, S. Ezugwu, M. S. Ahmed, M. G. Cottam and G. Fanchini, *Carbon*, 2015, **61**, 595
- [14] G. Grosso, G. P. Parravicini, *Solid State Physics*, Academic Press 2000, California, USA.
- [15] K.S. Novoselov, K.S., A. K. Geim, S. V. Morozov, D. Jiang, Y. Zhang, S. V. Dubonos, I. V. Grigorieva and A. A. Firsov, *Science*, 2004, **306**, 666
- [16] S. Ezugwu, *Synthesis and Characterization of Copper Nanoparticles and Copper-polymer Nanocomposites for Plasmonic Photovoltaic Applications*, MSc Thesis, Univ. of Western Ontario, London ON Canada, 2012. see also, <http://ir.lib.uwo.ca/etd/1025>.
- [17] A. Akbari-Sharbaf, S. Ezugwu, M. S. Ahmed, M. G. Cottam and G. Fanchini. *Carbon* 61 (2015) 595 – 601
- [18] J. Park, P. Bazylewski, G. Fanchini, *Nanoscale*, **2016**, 8, 9563

[19] S. Sadeghzadeh, N. Rezapour, *Superlattices and Microstructures* (2016), doi: 10.1016/j.spmi.2016.09.009.

[20] P. Bazylewski, A. Akbari-Sharbaf, S. Ezugwu, T. Ouyang, J. Park and G. Fanchini (2016). *Graphene Thin Films and Graphene Decorated with Metal Nanoparticles*. In Crystalline and Non-Crystalline Solids, Edited by Pietro Mandracci. InTech Publication, 1-16

[21] Z. Wang, R. Xie, C. T. Bui, D. Liu, X. Ni, B. Li, J. T. L. Thong, *Nano Lett.*, **2011**, 11(1), 113

Chapter Five

Physical Properties of Organic Polyradical P6OV and Its Bistability³

5. 1 Introduction

Memory devices are a critical component in the field of information technology [1,2]. They can be divided into volatile and non-volatile, depending on the time for which they can retain the stored information [2]. Volatile memory devices, including dynamic and static random access memory components, require stored data to be refreshed every few milliseconds. They cannot store data after the removal of the voltage used to write them. Most electronic systems require non-volatile memory components for bootstrap and persistent data storage. To date, the most common non-volatile memory components used in information and communication technology are devices that are writable once and readable multiple times (WORM). Flash memories that are writable, readable and erasable multiple times are more attractive, because they can be reused, but their costs are still high [3]. Silicon-based flash devices consisting of a metal–oxide–semiconductor field effect transistor, with high k-dielectric oxides [4] and an additional floating gate in each memory pixel, have been dominating the market of non-volatile devices writable and erasable multiple times, [5] but suffer from limited margins of improvement and high fabrication costs. Inorganic floating gates used to store the information cannot be less than 32 nm thick in such components [6].

Organic memristors, memory devices based on organic thin films with multistable resistivity characteristics, are being explored as possible substitutes for volatile, WORM and flash inorganic memory devices [7–9]. They have the advantage of low fabrication costs and can

³This chapter is published: S. Ezugwu, J. Paquette, V. Yadav, J. Gilroy and G. Fanchini. *Adv. Electron. Mater.* **2016**, 1600253

be processed from organic compounds in solution. Although continuous organic thin films with thicknesses down to 10 nm have been demonstrated, [10] the minimum thickness that can be reached by organic “flash” memristors is still too high, at more than 15 nm [11]. Proposed systems for organic memory devices include polyimide containing moieties, [12] polymers containing metal complexes [13] and nonconjugated polymers incorporating other organic materials (e.g., fullerenes, graphene oxide, carbazoles) directly [14,15] and blended with polymers [16]. In most of these devices, two or more layers or phases are required, which poses insurmountable limitations to the ultimate thinness of the device. Flash memory devices comprising only a single layer of polymer are essential to keep their thickness to a minimum, and have been proposed [17,18]. However, no devices thinner than 50 nm have been reported to date due to lack of general design criteria for these devices. Another significant issue with organic memristors is to obtain stable flash effects, devices that are reproducibly writable and erasable a very large number of times. Although memory devices based on radical polymers have been proposed, [19,20] their stability so far have been limited to a few writing cycles, in spite of the excellent quality of the active layer, which indicates that more fundamental knowledge of the physics of these devices is required.

In this chapter, we present the result of our work on single-layer organic flash memristors fabricated from poly-[1,5-diisopropyl-3-(cis-5-norbornene-exo-2,3-dicarboxiimide)-6-oxoverdazyl] (P6OV), a recently synthesized polyradical, [21]. P6OV is here presented as an alternative to semiconducting, π -conjugated organic polymers [10–16] which are more commonly used in memristors. We show that a decisive advantage of P6OV is that it exhibits three tunable and switchable charge states (positive, neutral and negative) [21] while the few previous examples of polyradicals incorporated into memristors exhibited no more than two

charge states [19,22,23]. The chapter includes a discussion on the physical model for optimizing single-layer polyradical memristors. We will show that the energy levels of the positively and negatively charged states of the radical polymer need to align, respectively, to the cathode and anode work functions of the radical polymer in order to offer efficient non-volatile “flash” memory effects. Our model explains why, in previous works, [19,20,22,23] combinations of multiple different polyradicals were required to observe memory effects, either in layered battery- like structures, [19] or by combining a pendant radical and an ion containing block copolymer, [20] but often led to WORM devices, with no bistable flash memory effects.

5.2 Experimental

5.2.1 Device Fabrication

P6OV, the polyradical used in this thesis work as a case study for memristor optimization, was synthesized via ring-opening metathesis polymerization (ROMP) by Gilroy’s group in the Department of Chemistry, as described in chapter one. The quality and purity of the raw radical polymer material was assessed at various synthesis steps by X-ray diffractometry, cyclic voltammetry (CV), electron spin resonance spectroscopy, gel-permeation chromatography, nuclear magnetic resonance spectroscopy, and infrared and UV–vis absorption spectroscopy [21]. This polyradical dissolves readily in a variety of different solvents and can be easily formed into smooth thin films via spin coating, even at the lowest thicknesses.

P6OV thin film preparation was carried out in a nitrogen-loaded glove box (Nexus II, Vacuum Atmospheres Co.). The glove box is directly attached to an ultrahigh vacuum (UHV) chamber dedicated to thin-film contacting and metallization for memristor device fabrication from organic thin films. The glove box is also equipped with a multi-probe station for electronic

device testing [40]. The oxygen and moisture levels in the glove box were less than 5 ppm. With the UHV chamber attachment, the entire device fabrication and testing process could be directly carried out without direct sample exposure to air. P6OV thin films were spun from a solution of P6OV (25.0 mg) in anhydrous chlorobenzene (2.0 mL) in the aforementioned glove box. The solution was stirred overnight at 50 °C and subsequently filtered through 0.45 μm pore-size syringe filters (Cole–Parmer). Different spin speeds from 3000 to 500 rpm were used on a KW4 spin coater (Chemat Technologies Inc.) to obtain a set of films of thicknesses ranging from 10 ± 4 to 50 ± 4 nm, respectively.

BK7 glass substrates (Corning) with a variety of different pre-deposited bottom contact electrodes were used for P6OV thin-film growth in this study: (i) indium–tin oxide ($15 \Omega \text{ sq}^{-1}$ sheet resistance, purchased from Sigma-Aldrich, cat no. 50926-11-9), (ii) few layer graphene (FLG) layers grown using the solution-based processing technique described in chapter one introduced, a method previously developed by our group, [41,42] (iii) thermally evaporated aluminum (50 nm thickness) layers, and (iv) top calcium (20 nm) and bottom Al (30 nm) bilayers. Al/Ca bilayer electrodes are widely used in organic solar cell technologies because they offer work functions of $\approx 2.9\text{--}3.5$ eV that is intermediate between Ca and Al [24].

Al/Ca and Al bottom contact electrodes of the memristors investigated in this thesis work were directly deposited by thermal evaporation in the vacuum chamber adjacent to the fabrication glove box, immediately prior to spin-coating the overlying P6OV films. For Ca and Al deposition, pellets of these metals (KJ Lesker, no. EVMCAX203MMD and Aldrich no. 7429-90-5, respectively) were placed in alumina crucibles (KJ Lesker, no. EVC9AO). Crucibles were mounted in resistive tungsten basket heaters (KJ Lesker, no. EVB8B3030W) in the thermal evaporator chamber. These heaters were connected to a HP 6466C DC high-current power

supply and currents of 30 and 75 A (at 3 and 8 V) were used to evaporate Ca and Al, respectively. The thickness of thermally evaporated metal electrodes was measured in situ during growth using a Sycom STM-2 thickness monitor equipped with a quartz crystal oscillator. Each one of the four different predeposited bottom contact electrodes, Al/Ca, Al, FLG or ITO, was pre-patterned to obtain four identical areas on each glass substrate, following the architecture shown in **Figure 5.1** below.

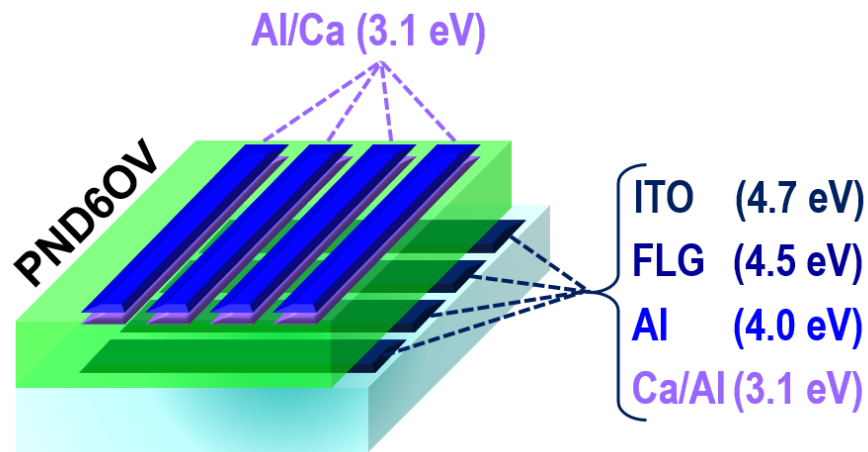


Figure 5.1: The memristor architecture used in this study. Sixteen memristors were simultaneously fabricated by spin coating a 10 nm thick layer of P6OV onto four identical prepatterned cathode electrodes, with four orthogonal anodes on top. The work function of the cathode materials is also indicated.

Even at the lowest thickness, 10 ± 4 nm, P6OV films on pre-patterned electrodes were previously shown to be continuous [21]. All of the memristor devices investigated in work were completed with electrode contacts on top of P6OV films, which consisted in Ca/Al bilayers (20 nm thick Ca and 30 nm thick Al). Top contacts were also thermally evaporated in the UHV chamber contiguous to the fabrication glove box immediately after P6OV thin film deposition. It is worthwhile noting that a symmetric device, with equal top and bottom contact work functions,

is obtained when bottom Al/Ca electrodes are used. Top contact devices were also patterned using an evaporation shadow mask, therefore our fabrication process allowed the formation of a 4×4 matrix of sandwich memristors from the same P6OV thin film, as shown in Figure 5.1, which were used for uncertainty estimates on the device performance.

5.2.2 Characterization

The topography and surface potential of P6OV thin films were simultaneously determined by atomic force microscopy (AFM) and Kelvin probe force microscopy (KPFM), respectively. AFM/KPFM images were recorded using a Witec Alpha 300S atomic force microscope system integrated with a KPFM accessory and a Stanford DS 345 function generator [43]. The operation and functionalities of this equipment were described in details in Section 1.3 of Chapter one. During the KPFM measurement, the function generator is locked-in at the second order harmonics of the AFM cantilever using the Stanford SR844-RF lock-in amplifier that is directly operated by the digital controller of the Witec instrument [43]. The KPFM measurements were performed in the correspondence of aluminum film (80 nm thickness), which was evaporated on the polymer thin film in the same deposition chamber described above. To minimize KPFM artifacts due to lateral contact of the tip with the film edge, [35] sample scans were performed parallel to the polymer-Al interface, resulting in a significant reduction in lateral contact artifacts. It is worthwhile to note that KPFM is capable of detecting effects at the mesoscopic level (i.e., a few nm or more) [43]. This technique is ideal to probe our system with a spatial resolution of about the length of an entire polyradical chain. At this scale, localized phenomena occurring at the individual monomer level are averaged, and the technique is ideal

for probing collective changes in a polyradical chain that switch it from low conductivity to high-conductivity states in P6OV memristors.

Current–voltage characteristics of the devices were recorded in sandwich configuration using a computer automated Keithley 2400 source meter with 10 mV scan step. In order to investigate the electrical bistability and optimize the write voltage (V_W), read voltage (V_R), and erase voltage (V_E) associated with the memory performance under different electrode properties, the current–voltage scans were performed at ± 10 V, a voltage range in which the device is known not to breakdown [21]. The stability tests were performed by repeated application of V_W , V_R , V_E , and V_R , in this order. Control devices, consisting in Al/Ca/P6OV/Ca/Al stack, were similarly investigated for comparison.

5.3 Current–Voltage Characteristics and Electronic Energy Levels in P6OV

The current–voltage (J–V) characteristics of one of our devices are shown in **Figure 5.2**. When tested for the first time, devices always exhibited a low-conductivity state. The low-conductivity J–V curve, indicated by red open dots in Figure 5.2, was recorded by sweeping the voltage at ± 10 mV s⁻¹ rate. Starting from $V = 0$, increasing negative voltages were applied, which led to relatively low current densities, $\approx 10^{-1}$ A cm⁻², until “write” voltage conditions were reached at $V_W \leq -4.8$ V. At these voltage levels, the system gradually transitioned to a high-conductivity state, with significantly higher current densities, about 1–10 A cm⁻². The corresponding J–V curve is indicated by black solid dots in Figure 5.2 and is representative of significantly higher conductivity in P6OV. The high-conductivity state persists at increasing positive voltages, until “erase” conditions are reached at $V_E \geq +3.5$ V. Sweeping at voltages larger than +3.5 V led the device to gradually revert to the low-conductivity state. As no transitions from high to low-conductivity state and vice versa occur in the $V_R = \pm 1.0$ V range,

any voltage $-V_R < V < +V_R$ can be used to “read” the device and understand in which state it lays.

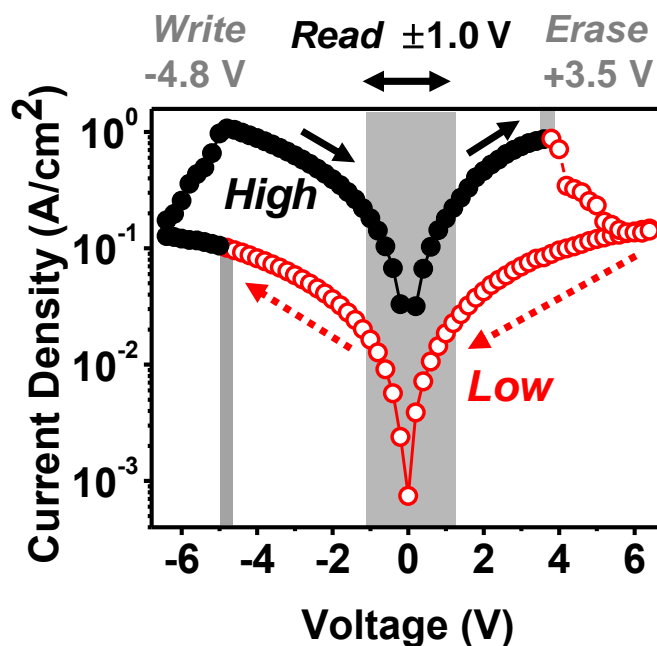


Figure 5.2: Current density–voltage (J – V) characteristics of a device showing memory effects, in which the write (V_W), read (V_R), and erase (V_E) voltages are indicated. Arrows along the J – V curves indicate the scanning direction, starting from $V = 0$. Red open dots correspond to the low-conductivity regime (for $V < 0$ until $V = V_W$ is reached). Black solid dots correspond to the subsequent high-conductivity regime (for $V_W < V < V_E$). The system gradually reverts to the low-conductivity regime at $V = V_E$.

In order to optimize the performance of P6OV as an active memory material, it is imperative to construct an energy-level matched electronic structure for the devices. P6OV in its neutral state is expected to possess a singly occupied molecular orbital (SOMO) at about mid-gap between the doubly occupied highest occupied molecular orbital (HOMO, π -bonding), and the lowest unoccupied molecular orbital (LUMO, π^* -antibonding). Considering that P6OV is a

nonconjugated polymer, the HOMO–LUMO energy band gap $E_{\pi\pi^*}$, corresponding to $\pi \rightarrow \pi^*$ interband optical transitions is expected to sit in the near-UV photon energy range, comparable to or slightly lower than 5.6 eV in benzene [28,29]. From our UV–visible (UV–vis) absorption measurements, reported in panel (a) of **Figure 5.3**, a broad and intense optical absorption feature is observed at 4.6 eV, with tails up to 5.0–5.2 eV. We therefore assign this optical absorption peak to $\pi \rightarrow \pi^*$ optical transitions between HOMO and LUMO molecular orbitals, with the formation of a delocalized electron–hole pair.

From Figure 5.3a, two less intense optical absorption features are also observed at lower energy, in the blue photon energy range. These peaks can be understood due to the presence of a SOMO energy level within the π – π^* optical band gap of P6OV and they can be assigned to SOMO $\rightarrow \pi^*$ and $\pi \rightarrow$ SOMO transitions, respectively. In SOMO $\rightarrow \pi^*$ transitions, an electron is promoted from an initially neutral (0) SOMO state to the LUMO, with the formation of a localized hole (+) in the correspondence of the SOMO and an electron delocalized in the conduction (π^*) band. In a $\pi \rightarrow$ SOMO transition, one electron is promoted from the HOMO to an initially neutral (0) SOMO state, at which a localized electron (–) is formed in conjunction with a delocalized hole in the valence (π) band. Closeness of the SOMO \rightarrow LUMO and HOMO \rightarrow SOMO optical absorption peaks, sitting at $E_{(0),(+,\pi^*)} \approx E_{(0,\pi),(-)} = 3.0 \pm 0.1$ eV, suggests that neutral SOMO energy levels are situated at $\varepsilon_{(0)} \approx \frac{1}{2} (\varepsilon_{\pi} + \varepsilon_{\pi^*})$, thus at mid-gap between the π and π^* band energy levels, ε_{π} and ε_{π^*} . This leads to the diagram of π , π^* , and (0) density of electronic states reported in **Figure 5.3b**.

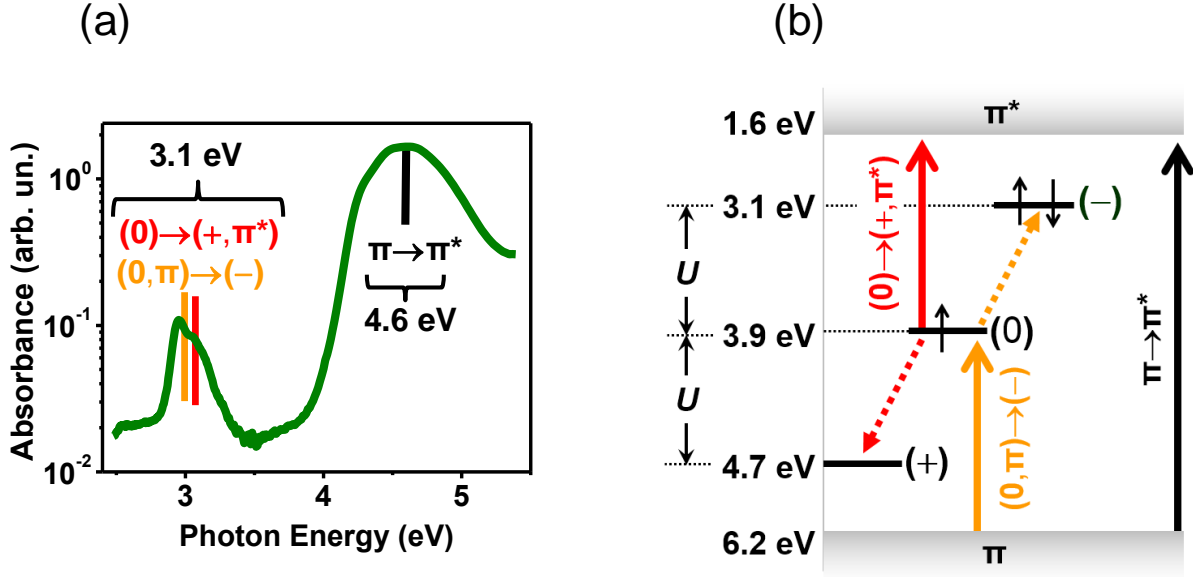


Figure 5.3: (a) P6OV absorbance versus photon energy. An intense absorption band at $E_{\pi\pi^*} = 4.6$ eV is observed, which is assigned to $\pi \rightarrow \pi^*$ interband transitions. Two less intense optical absorption bands at 3.1 ± 0.1 eV are assigned to SOMO \rightarrow LUMO and HOMO \rightarrow SOMO transitions. (b) Diagram of optical transition energies. The neutral SOMO level (0) sits close to mid-gap, which is corroborated by the closeness of SOMO \rightarrow LUMO and HOMO \rightarrow SOMO transition energies $E_{(0),(+,\pi^*)}$ and $E_{(0,\pi),(-)}$ (yellow and red lines in (a)). However, $E_{(0),(+,\pi^*)} + E_{(0,\pi),(-)} > E_{\pi\pi^*}$ due to non-negligibility of the Hubbard energy U in the SOMO level. The SOMO becomes positively charged (+) when losing an electron, actually leading to $(0) \rightarrow (+,\pi^*)$ transitions, and becomes negatively charged (-) when gaining one electron, actually leading to $(0,\pi) \rightarrow (-)$ transitions.

Although the energies $E_{(0),(+,\pi^*)}$ and $E_{(0,\pi),(-)}$ we assign to $(0) \rightarrow (+,\pi^*)$ (i.e., SOMO \rightarrow LUMO) and $(0,\pi) \rightarrow (-)$ (i.e., HOMO \rightarrow SOMO) transitions in Figure 5.3b are similar, it is interesting to observe that their sum, $E_{(0),(+,\pi^*)} + E_{(0,\pi),(-)} \approx 6.2$ eV, is significantly larger than $E_{\pi\pi^*} = 4.6$ eV, the $\pi \rightarrow \pi^*$ interband transition energy. This phenomenon can be understood by

considering the few-electron nature of (+), (0), and (−) electron states. Delocalized π and π^* electronic bands are multielectron systems that are marginally affected by the addition or removal of one electron [30–32]. However, these effects are expectedly more significant when a neutral SOMO state, a single-electron system, undergoes $(0) \rightarrow (+, \pi^*)$ or $(0, \pi) \rightarrow (-)$ transitions, with the consequent removal or addition of one electron, and the formation of an unoccupied (+) positively charged state or a doubly occupied (−) negatively charged state.

In few-electron systems, the actual position of an electron energy level is dramatically affected by their occupation number [31]. The subsequent change in energy levels, known as the Hubbard interaction energy U , corresponds to the energy lost or gained by the system due to the addition or removal of one electron [30,32] as a consequence of the increase or decrease in electron–electron Coulombic repulsion. When positively charged, a neutral (0) SOMO state sitting at $\varepsilon_{(0)}$ below the vacuum level is expected to generate an unoccupied energy level situated at $\varepsilon_{(+)} = \varepsilon_{(0)} + U$. Conversely, when the same SOMO state is negatively charged due to the addition of one extra electron, negative electron–electron Coulombic repulsion energy is more significant and the corresponding doubly occupied energy level will be situated at $\varepsilon_{(-)} = \varepsilon_{(0)} - U$. Consequently, under the assumption that $\varepsilon_{(0)}$ sits at mid-gap, nonzero Hubbard interaction energy results in $(0) \rightarrow (+, \pi^*)$ and $(0, \pi) \rightarrow (-)$ optical transitions occurring at

$$E_{(0)(+, \pi^*)} = \varepsilon_{\pi^*} - \varepsilon_{(+)} \approx \frac{1}{2}E_{\pi\pi^*} - U; \quad E_{(0, \pi)(-)} = \varepsilon_{(-)} - \varepsilon_{\pi} \approx \frac{1}{2}E_{\pi\pi^*} - U \quad (5.1)$$

respectively, which indicates $U \approx 0.8$ eV, consistent with similar values that were previously found in small carbon clusters [33].

In order to corroborate our UV-vis analysis and confirm the positions of ε_{π} , $\varepsilon_{(-)}$, $\varepsilon_{(0)}$, $\varepsilon_{(+)}$, and ε_{π^*} energy levels, we used Kelvin probe force microscopy (KPFM) images to directly measure the surface potential of P6OV. Surface potentials determined by KPFM may either

correspond to the position of the HOMO level, [34] the SOMO level, [35] or a combination of the two. In the specific case of P6OV, a polyradical exhibiting memory effects, the voltage used for KPFM imaging may influence the occupation number of mid-gap states, which may transition from neutral to positively or negatively charged, depending on the value of the nullifying bias voltage applied to the atomic force microscopy (AFM) tip used for the measurements, and affect the actual value of the surface potential. In order to solve this issue our KPFM images were performed after a first scan at which a high constant voltage +7 V, higher than the erase voltage of the device, was applied to the tip. Under those conditions, the device is erased, and the value of the surface potential is expected to reflect the position of the HOMO and SOMO levels.

Figure 5.4a shows the AFM and KPFM images, recorded simultaneously, of a P6OV thin film (bottom half of the images) in proximity of an aluminum contact thermally evaporated on top of it (top half of the images). The AFM image shows that P6OV is smooth and homogenous, which is indicative of nearly ideal conditions for KPFM measurements [35]. The KPFM image is also entirely uniform, with the exception of the sharp P6OV-Al interface. The Al contact can be used as a reference, since the work function of aluminum is known to be $\phi_{Al} = 4.0$ eV, [25] which compares well with the absolute values of surface potential obtained from nullifying KPFM voltages in that region. The histogram of surface potentials obtained from the Kelvin probe force image in Figure 5.4a is presented in **Figure 5.4b**, from which a value of 4.0 ± 0.1 eV, in excellent agreement with the known value of ϕ_{Al} , could be determined. Consequently, from the same histogram, it could be inferred that the HOMO energy level of P6OV sits at $\epsilon_{\pi} = 6.2 \pm 0.2$ eV below the vacuum level.

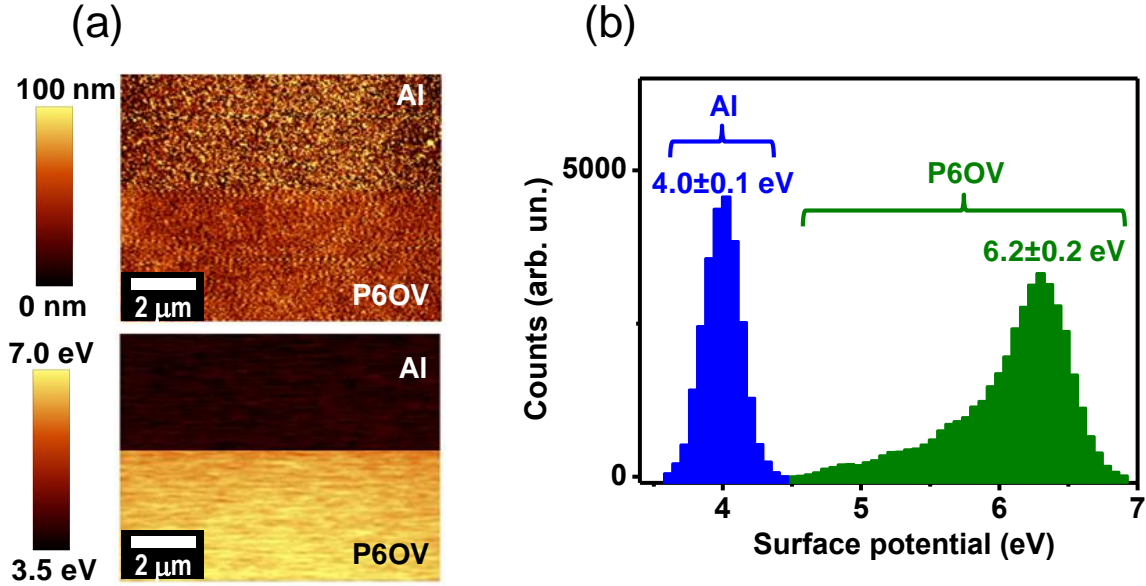


Figure 5.4: (a) AFM (top) and KPFM (bottom) images of P6OV film and nearby Al contact. (b) Histogram of surface potential obtained from KPFM image in (a). The HOMO energy level of P6OV sits at $\varepsilon_{\pi} = 6.2 \pm 0.2$ eV below the vacuum level as shown in Figure 5.3b.

From Figure 5.4b, it can also be observed that, in addition to the sharp peak at $\phi = \varepsilon_{\pi} = 6.2$ eV, the histogram of the surface potential of P6OV possesses a relatively broad tail at lower values of ϕ , down to about 4 eV. Although a quantitative multipeak fit would be too arbitrary, this low-energy tail indicates that values of $\varepsilon_{(0)} = 4.0 \pm 0.2$ eV are consistent with those that were directly inferred from Equation (5.1) and UV–vis absorption data. These results corroborate the band energy diagram of P6OV reported in Figure 5.3b, from which it is worthwhile noting that the energy level of unoccupied and positively charged polyradical sites, $\varepsilon_{(+)} = 4.7 \pm 0.2$ eV, aligns well with the work function of ITO electrodes, $\phi_{\text{ITO}} = 4.7$ eV. Conversely, the energy level of doubly occupied and negatively charged polyradical sites, $\varepsilon_{(-)} = 3.1 \pm 0.2$ eV, aligns well with the work function of Ca/Al electrodes, $\phi_{\text{Ca/Al}} = 3.1$ eV [24]. Finally $\varepsilon_{(0)}$, the energy level of the

neutral SOMO state, matches the work function of pure Al ($\phi_{\text{Al}} = 4.0$ eV) [25]. We anticipate that these findings will be essential for the construction and optimization of P6OV memristors, as well as for studying their transport properties, both in the high-conductivity and low-conductivity regimes.

5.4 Memristor Design Criteria

Panels (a) and (b) of **Figure 5.5** compare the current–voltage characteristics in the high-conductivity and low-conductivity regimes of four different devices. Such devices have the same anode, an Al/Ca bilayer, but utilize four different cathode materials at work functions ranging from $\phi = 3.1$ eV (for Ca/Al) to $\phi = 4.7$ eV (for ITO). Pure aluminum and weakly oxidized few-layer graphene ($\phi_{\text{FLG}} = 4.5$ eV) have work functions with intermediate values between those of Ca/Al and ITO [25–27]. **Figure 5.5a** reports the J–V curves of the devices in the high-conductivity regime, which are representative of typical values that were consistently found in a large number of similar devices. Conductivity in the high-conductivity regime was found to decrease in the order of

$$\sigma_{\text{H}}(\text{ITO}) > \sigma_{\text{H}}(\text{FLG}) > \sigma_{\text{H}}(\text{Al}) > \sigma_{\text{H}}(\text{Ca/Al}) \quad (5.2)$$

and, therefore, is higher for ITO-based devices, of which the cathode work function aligns with the surface potential of positively charged P6OV, $\phi_{\text{ITO}} = \varepsilon_{(+)} = 4.7$ eV.

In the other three types of devices, with FLG, Al and Ca/Al cathodes and $\phi \neq \varepsilon_{(+)}$, σ_{H} decreases at decreasing work function of cathode, proportionally to $\exp(-|\varepsilon_{(+)} - \phi| / k_{\text{B}}T)$. σ_{H} is lowest in devices with symmetric anode and cathode, both made out of Ca-coated aluminum. Even though their electrode work function matches the surface potential of negatively charged P6OV at $\phi_{\text{Ca/Al}} = \varepsilon_{(-)} = 3.1$ eV, the (+) energy level is much higher, at 4.7 eV, which leads to very significant

contact resistance.

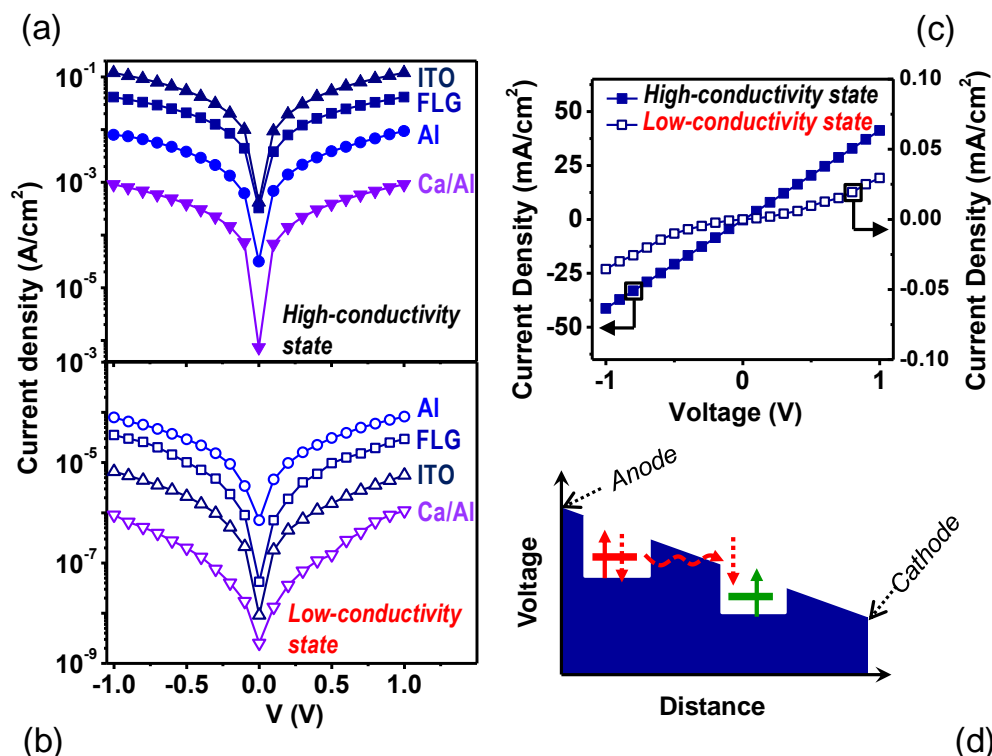


Figure 5.5: Current density versus voltage characteristics of P6OV thin films as a function of the cathode material in a) high-conductivity and b) low-conductivity regime. Output currents are strongly dependent on the work function of the cathode material. c) High-conductivity and low-conductivity current densities of Al/Ca-P6OV-FLG devices, showing ohmic and Poole–Frenkel behavior in the high and low conductivity regimes, respectively. d) Poole–Frenkel model at moderate electric fields, which leads to hopping in the low-conductivity regime.

The nearly ohmic characteristics of the J-V curves, demonstrated in **Figure 5.5c** for a device with FLG cathode, indicates extended-state transport in the high-conductivity regime for all of the devices irrespectively of the cathode material, consistently with previous observations in P6OV [21]. These observations strongly suggest that σ_H is determined by the contact resistance between positively charged P6OV monomers and the cathode in the same way as the contact

resistance between negatively charged P6OV monomers and the anode. Consequently, it is demonstrated that both positively charged (+) and negatively charged (–) oxoverdazyl rings in P6OV are required to observe extended state transport and high-conductivity regime in thin film memristors of this polyradical.

Further insight into the bistability and transport properties of P6OV memristors can be gained by observing their behavior in low-conductivity regime. In such regime, their conductivity can be inferred from the J-V curves in **Figure 5.5b**, and was observed to decrease in the order of

$$\sigma_L(\text{Al}) > \sigma_L(\text{FLG}) > \sigma_L(\text{ITO}) > \sigma_L(\text{Ca/Al}). \quad (5.3)$$

Consequently, σ_L is higher for cathodes of pure aluminum, with work function $\phi_{\text{Al}} = \varepsilon_{(0)} = 4.0$ eV, aligning to the SOMO of neutral P6OV. In the other three types of devices, with FLG, ITO and Ca/Al cathodes at $\phi \neq \varepsilon_{(0)}$, σ_L decreases as $\exp(-|\varepsilon_{(0)} - \phi| / k_B T)$. This indicates that the conductivity of P6OV memristors in the low-conductivity regime is determined by the contact resistance between the SOMO and the cathode. Such an observation agrees with previous findings [21] that the transport properties in such regime obey a Poole-Frenkel transport mechanism, demonstrated in **Figure 5.5d**, which involves diffusion of a limited number of localized electrons that are hopping through an array of neutral P6OV repeating units.

Figure 5.6 summarizes the information on the charge transport mechanism of our memristors in the low-conductivity (panel a) and high-conductivity (panel b) regimes, as can be inferred from the results shown in Figure 5.5. In the low-conductivity regime, P6OV monomers are in the neutral charge state. This finding is corroborated by previous electron spin resonance (ESR) measurements [21] showing a number of paramagnetic radicals comparable to the number of monomers. Optimal charge injection in the low-conductivity state occurs by electrons

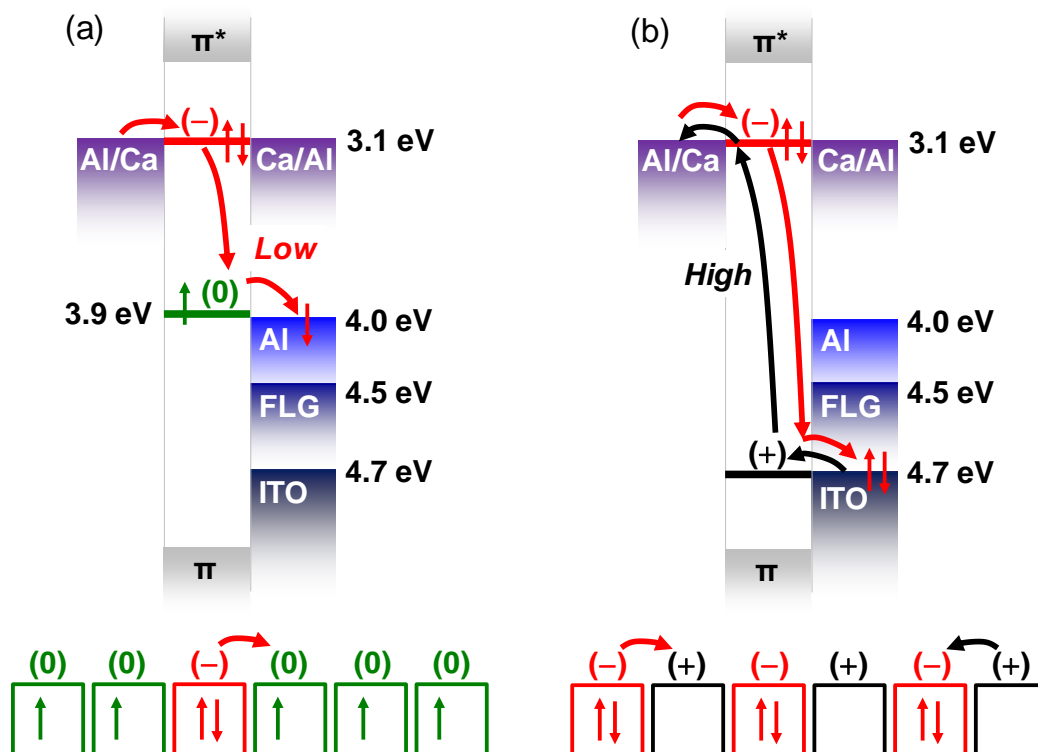


Figure 5.6: Energy band diagram of P6OV-based memristors demonstrating optimized charge transport in (a) low-conductivity and (b) high-conductivity regime. Energy bands in different memristor components are shown. Optimal charge injection in the low-conductivity regime occurs at 4.0 eV for electrons transferred to P6OV from the Al cathode. These electrons hop from monomer to monomer in a Poole-Frenkel transport mechanism (bottom left). In the high-conductivity regime, optimal hole injection occurs at 4.7 eV, when the cathode work function matches the $\varepsilon_{(+)}$ level of P6OV, and optimal electron injection occurs at 3.1 eV, when the anode work function matches the $\varepsilon_{(-)}$ level of P6OV. Simultaneous optimization of injection of electrons and holes is necessary to maximize extended state charge transport in the high-conductivity regime (bottom right).

transferred from the Al cathode at 4.0 eV work function. Such electrons hop between polymer repeating units in a Poole-Frenkel transport mechanism, for which a limited number of

monomers become positively charged. Hopping processes are relatively inefficient transport mechanisms, due to the localized nature of the carriers [36]. This explains the low conductivity in this regime.

Application of sufficiently high electric fields leads to charge polarization of thin film dielectric materials [37]. This is consistent with the fact that the 3.5 V threshold for erase voltages in our devices correspond to an energy $eV_E \approx 4U$, which is the sum of the formation energies of a doubly occupied, negatively charged monomer and an unoccupied and positively charged monomer. This configuration, shown in **Figure 5.6b**, preserves the charge neutrality of the polymer chain and is consistent with the observed lack of ESR signal in P6OV thin films in the high-conductivity state. In this regime, which occurs after the P6OV is polarized by an external electric field, ambipolar transport may occur by extended states, via diffusion of electrons toward the anode and simultaneous migration of holes through the cathode. It is worthwhile noting that, in this regime, optimal hole injection occurs for charges transferred from ITO to the $\epsilon_{(+)}$ level of P6OV, both at ~ 4.7 eV, while optimal injection of electrons occurs for charges transferred from Ca/Al to the $\epsilon_{(-)}$ level of P6OV, both at ~ 3.1 eV. For practical memristor applications, the “on” current in the high-conductivity state needs to be maximized, while the “off” current in the low-conductivity state needs to be kept to a minimum. Therefore, Al/Ca-P6OV-ITO architectures are optimal for the fabrication of polyradical thin film memristors based on P6OV, and our design criteria can be extended to ultrathin memory devices from a large variety of polyradicals, clearly indicating the generality of our study.

It is also important to bear in mind that the transport mechanism we propose in Figure 5.6 for our polyradical system in the high-conductivity state requires the polarization of an entire polyradical chain, not only individual monomers. Thus, our model is mesoscopic in nature and

not limited to individual quantum systems. The fact that, in our case, the Hubbard interaction energy of a single radical monomer coincides with the corresponding quantity averaged over an entire polyradical is a consequence of the fact that P6OV is nonconjugated and, therefore, each monoradical can be treated as a nearly isolated system. However, this does not limit the generality of the model, which can be applied to conjugated systems by considering that U can still be defined in such cases, and decreases with the number of monomers in the polyradical.

5.5 Memristor Performance

To demonstrate the critical significance of the electrode work functions in relation to the energy levels of the polyradical and the performance of the memory devices we fabricated, we carried out multiple consecutive cycles of electrical switching between low and high-conductivity regimes, as illustrated in **Figure 5.7**. Switching cycles presented in this work were performed for devices with the same anode, an Al/Ca bilayer, but different cathode materials with work functions decreasing from $\phi = 4.7$ eV (for ITO, panel a) to $\phi = 3.1$ eV (for Ca-coated Al, panel d). In all of these devices, the write, read and erase conditions were implemented by applying an appropriate external voltage, as previously shown in Figure 5.2. The switching of applied voltages is demonstrated by the lower red curves in Figure 5a-d.

Figure 5.7 confirms that negative 4.8 V write voltages brought the devices shown in panels (a–c) to a high-conductivity state. This regime led to relatively high output currents that could be read at +1.0 V applied voltage, while no appreciable transition could be observed in the symmetric Al/Ca-P6OV-Ca/Al device shown in panel (d). In panels (a)–(c) of Figure 5.7, a positive 3.5 V erase voltage eliminated the previously established high-conductivity regime, and returned the device to the low-conductivity state, as could be confirmed by subsequent readings

at +1.0 V. Once the devices switched to either state, they produced output currents commensurate with the conductivity in such regime, accordingly to Equations (5.2) and (5.3). Dramatically different behaviors and on/off ratios are therefore expected with different cathode materials.

Current changes during multiple sequences of write-read-erase-read cycles are demonstrated by the top blue curves in Figure 5.7, with the currents measured during six read cycles at $V_R = 1.0$ V are indicated by black dotted lines. In panels a and b, the two dotted lines are parallel and well distinguishable, indicating that different currents are reproducibly measured in the high-conductivity and low-conductivity regimes even after several write and erase operations. Figures 5.7a-b demonstrate that a bit can be written, stored, read and erased multiple times in P6OV based memristors with ITO and FLG cathodes. High on/off current ratios are generally associated with superior memory device performance [17,18]. Our memristors fabricated on ITO and FLG cathode materials (work functions: $\phi_{\text{ITO}} = 4.7$ eV and $\phi_{\text{FLG}} = 4.5$ eV, respectively) exhibited on/off current ratios of 400 and 30, respectively. These results point to the strong significance of the work function of the cathode materials on the performance of these memristors and with the fact that ITO cathodes are optimal for the performance of our devices, consistently with the band diagrams drawn in Figure 5.6. Stability and reproducibility of both ITO-based and FLG-based devices indicate that they both exhibit flash memory effects.

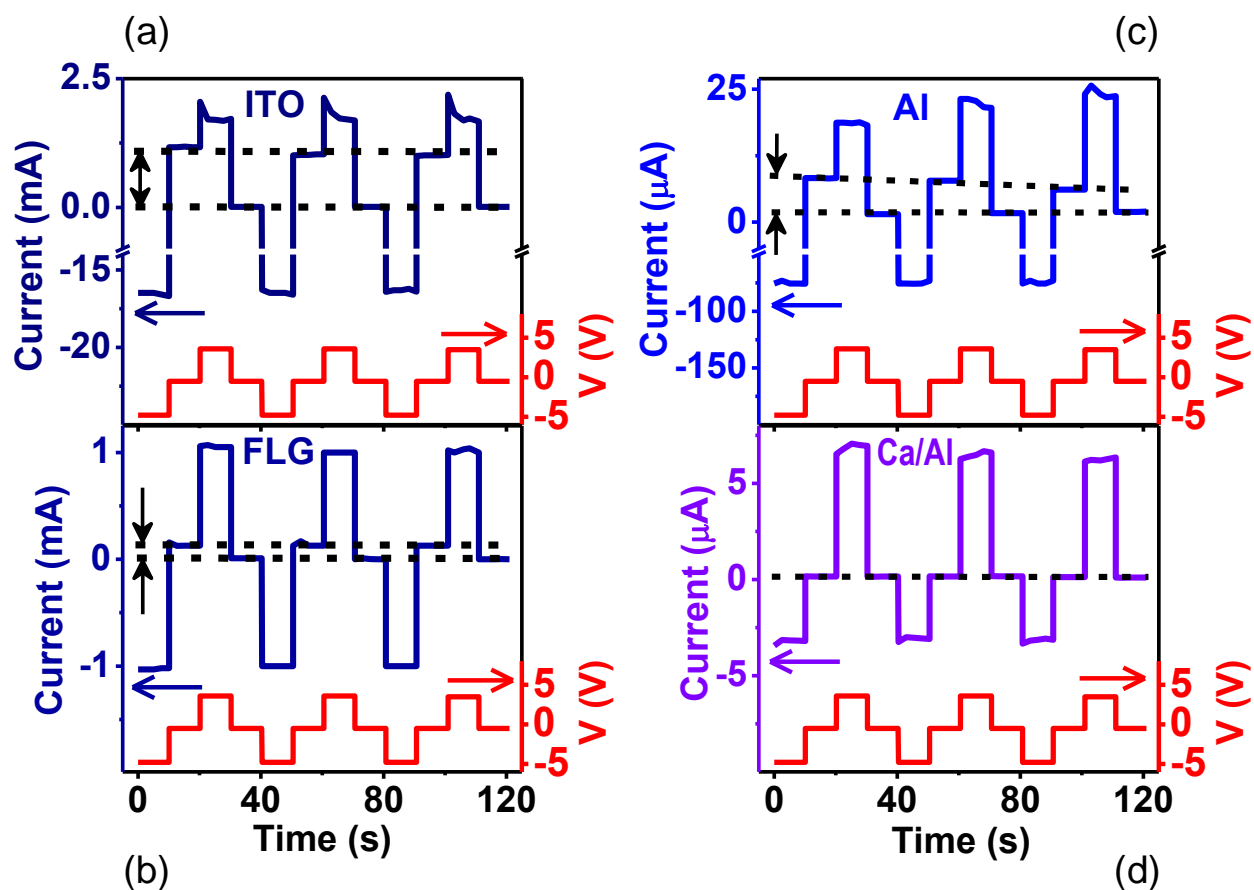


Figure 5.7: Measured output current (top curves) and corresponding applied voltages (red bottom curves) during multiple write–read–erase–read cycles of P6OV-based memristors with different cathode materials: (a) ITO (b) FLG (c) Al, and (d) Ca/Al. High-conductivity and low-conductivity states read at $V_R = +1.0$ V are indicated by black dashed lines, from which the on/off current ratios can be inferred. The work function of the cathode (e.g. FLG and ITO) needs to be 4.5–4.7 eV, comparable to the energy level $\varepsilon_{(+)}$ of the positively charged polyradical, in order to produce stable on/off ratios and ensure flash effects. Cathode work functions of the order of $\varepsilon_{(0)} \approx 4$ eV, the energy level of the neutral SOMO of P6OV, produce WORM effects, e.g. with Al. No memory effects were observed with symmetric Ca/Al and Al/Ca electrodes.

Panel c in Figure 5.7 shows that the “on” current of P6OV memristors with cathodes of pure Al decreases linearly with time after multiple write and erase cycles. Specifically, the on/off current ratio was about 6 during the first cycle, but decreased to 4 after the third writing cycle in this device architecture. Consequently, devices with Al cathode do not possess the same degree of stability and reproducibility of flash devices built on ITO and FLG electrodes, and they exhibit WORM effects. We assign this phenomenon to the lower work function of Al which aligns with the neutral energy level of P6OV, $\varepsilon_{(0)} = 4.0$ eV. In this configuration, electron transport from Al/Ca to the negatively charged energy level of P6OV and Al, at 4.0-eV is still optimized, but hole transport is not. Specifically, the positive energy level of P6OV, at $\varepsilon_{(+)} = 4.7$ eV, acts as a high-energy trap for holes diffusing from 4.0 eV energy in Al to 3.1 eV energy in Ca. This leads to the gradual depolarization and neutralization of some of the charged radical monomers of P6OV, corresponding to the gradual collapse of the high-conductivity state shown in Figure 5.6b. We suspect this effect is general enough to lead to lack of flash effects in several non-optimized polyradical memory devices that have been recently proposed in the literature [21-23].

In view of the above mentioned considerations, the major obstacle to polyradical memristor performance is in carefully engineering the contact resistance between the polymer thin films and the electrodes. Panel (a) in **Figure 5.8** demonstrates that a relationship exists between the cathode–anode work function difference and the measured on/off current ratios of the devices. Specifically, in symmetric Al/Ca-P6OV-Ca/Al devices, in which no surface potential difference between the electrodes exists, the high-conductivity state is extremely volatile and can only be retained for a relatively short time. Although J–V curves in the high-conducting regime can be obtained with relatively rapid scans as in Figure 3b, no on/off current

ratio higher than 1 could be obtained during write–read–erase–read cycles, and nonvolatile devices could not be achieved.

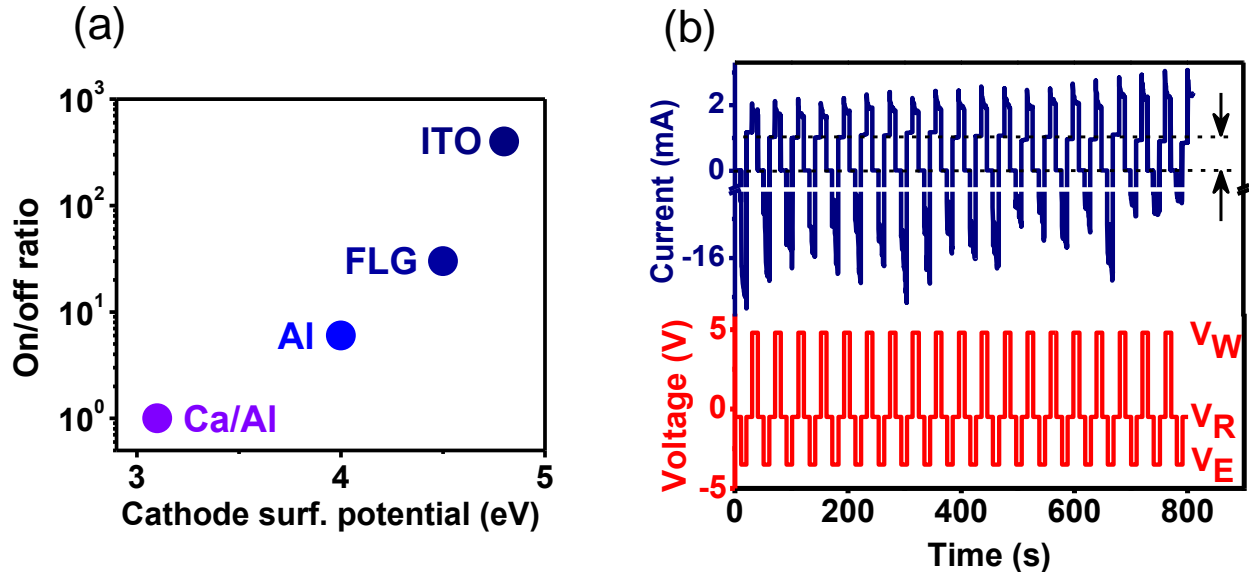


Figure 5.8: (a) On/off current ratio vs. device cathode surface potential. A high surface potential of the cathodes matching the positive charge state of P6OV are critical for high performance of the devices as shown in the optimized Al/Ca-P6OV-ITO memristor. (b) Current response (top curve) and corresponding applied voltage (bottom curve) obtained during the stability test of Al/Ca-P6OV-ITO memristor under constant write-read-erase-read voltage cycles. High on/off current ratios $\sim 10^2$ at 1.0 V reading voltage were achieved in the optimized device, with high reproducibility over several tens cycles of write–read–erase–read.

The capability of optimized memristors to retain information for a long period of time was further investigated. Once the on state of a device was activated, it was left in the glove box under nitrogen atmosphere without applied bias voltage. After a prolonged period of time, lasting up to several days, the device was still observed to remain in the same state and switched states

only with appropriate voltage bias. **Figure 5.8b** shows the result of the stability test studied on the same device under repeated cycles of bias conditions. The figure revealed that this device maintains excellent switching characteristics without degradation for several tens of cycles of on–off switching. These excellent switching cycles are a further demonstration that these types of devices, fabricated using a homogeneous layer of an organic polyradical, exhibit promising characteristics for operation as nonvolatile flash memristors.

5.6 Conclusion

In this chapter, we presented the fabrication of P6OV thin films and their characterization, and we outlined a design criterion for the fabrication of thin memristors based on a homogeneous active layer of this material. P6OV memristors may serve as a case study for the optimization of a broader class of polyradical thin film memristors. Devices presented in this chapter utilized a sandwich configuration with aluminum–calcium bilayers as anode material, and we investigated four cathode materials at different work functions, ranging from $\phi = 4.7$ eV for ITO electrodes to $\phi = 3.1$ eV for calcium–aluminum bilayers. The energy levels of the positive, neutral, and negative charge states of P6OV have been determined from a combination of UV–vis and KPFM measurements. The behavior of the SOMO energy level of P6OV at different degrees of charging could be understood in the framework of the Hubbard model [30] by assuming a correlation energy $U = 0.8$ eV. Knowledge of the positive, neutral and negative energy levels were vital to configure our memristor architectures for maximum performance.

Current–voltage characteristics show that a high-conductivity regime can be created, and subsequently eliminated by applying an erase voltage to the devices of the order of $V_E \approx 4U/e$. Resistivity in the high-conductivity regime was found to be lower for ITO-based devices, in

which the work function of the cathode matches the surface potential of positive charged P6OV radicals: $\phi_{\text{Al}} = \varepsilon_{(0)} = 4.0$ eV. In the other three types of devices, with FLG, Al and Ca/Al cathodes, and $\phi < \varepsilon_{(+)}$, the “on” current decreased at decreasing work function of the cathode. In the low-conductivity regime, the resistivity of P6OV memristors was determined by the contact resistance between the SOMO energy of neutral P6OV and the cathode. Consequently, the electrical conductivity was higher for devices with cathodes of pure aluminum, with work function $\phi_{\text{Al}} = \varepsilon_{(0)} = 4.0$ eV, but lower in the other types of devices with FLG, ITO, and Ca/Al cathodes, as the mismatch between the SOMO level $\varepsilon_{(0)}$ and the cathode work function increases. We demonstrated that the electrical bistability of our devices is due to two distinct transport regimes in P6OV, extended states and Poole–Frenkel.

Optimized flash memory effects were demonstrated in Al/Ca-P6OV-ITO, in which the energy levels of the positive and negative charged states of the polyradical align, respectively, to the cathode and anode work functions. More than 10^3 s of write–read–erase–read cycles were performed without significant current degradation. Conversely, Al/Ca-P6OV-Al devices, in which the cathode work function aligned with the neutral energy level of P6OV, exhibited WORM effects. Our results demonstrate the critical importance of energy-level matched electronic structures as the basis on which ultrathin, single-layer memristors can be successfully implemented.

References

- [1] J. C. Scott, L. D. Bozano, *Adv. Mater.* **2007**, 19, 1452.
- [2] M. Joodaki, *Selected Advances in Nanoelectronic Devices, Lecture Notes in Electrical Engineering*, Vol. 175, Springer-Verlag, Berlin **2013**, pp. 29–157.

- [3] Y. Ji, J. Hu, M. Lanza, *IEEE Nanotechnol. Mag.* **2015**, 9, 12.
- [4] M. Lanza, G. Bersuker, M. Porti, E. Miranda, M. Nafría, X. Aymerich, *Appl. Phys. Lett.* **2012**, 101, 4765342.
- [5] F. Yinug, *J. Int. Commer. Econ.* **2007**, 137, 1.
- [6] C. Zhao, C. Z. Zhao, S. Taylor, P. R. Chalker, *Materials* **2014**, 7, 5117.
- [7] M. A. Khan, U. S. Bhansali, D. Cha, H. N. Alshareef, *Adv. Funct. Mater.* **2013**, 23, 2145.
- [8] B. G. Kang, J. Jang, Y. Song, M. J. Kim, T. Lee, J. S. Lee, *Polym. Chem.* **2015**, 6, 4264.
- [9] Q. Boa, Q. Zhang, Y. Li, H. Li, J. He, Q. Xu, N. Li, D. Chen, J. Lu, *Org. Electron.* **2016**, 28, 155.
- [10] F. Zhang, C. Di, N. Berdunov, Y. Hu, Y. Hu, X. Gao, Q. Meng, H. Sirringhaus, D. Zhu, *Adv. Mater.* **2013**, 25, 1401.
- [11] J. Lee, E. Lee, S. Kim, G. S. Bang, D. A. Shultz, R. D. Schmidt, M. D. E. Forbes, H. Lee, *Angew. Chem. Int. Ed.* **2011**, 50, 4414.
- [12] K. L. Wang, Y. L. Liu, I. H. Shih, K. G. Neoh, E. T. Kang, *J. Polym. Sci., Part A: Polym. Chem.* **2010**, 48, 5790.
- [13] Y. Song, Y. P. Tan, E. Y. H. Teo, C. Zhu, D. S. H. Chan, Q. D. Ling, K. G. Neoh, E. T. J. Kang, *Appl. Phys.* **2006**, 100, 084508.
- [14] S. Paul, A. Kanwal, M. Chhowalla, *Nanotechnology* **2006**, 17, 145.
- [15] B. Zhang, Y. J. Chen, Y. F. Zhang, X. D. Chen, Z. G. Chi, J. Yang, J. M. Ou, M. Q. Zhang, D. H. Li, D. Wang, M. K. Liu, J. Y. Zhou, *Phys. Chem. Chem. Phys.* **2012**, 14, 4640.
- [16] Q. Zhang, J. Pan, X. Yi, L. Li, S. M. Shang, *Org. Electron.* **2012**, 13, 1289.

- [17] S. J. Liu, P. Wang, Q. Zhao, H. Y. Yang, J. Wong, H. B. Sun, X. C. Dong, W. P. Lin, W. Huang, *Adv. Mater.* **2012**, 24, 2901.
- [18] J. Chen, D. Ma, *Appl. Phys. Lett.* **2005**, 87, 023505.
- [19] Y. Yonekuta, K. Susuki, K. Oyaizu, K. Hondu, H. Nishide, *J. Am. Chem. Soc.* **2007**, 129, 14128.
- [20] T. Suga, M. Sakata, K. Aoki, H. Nishide, *ACS Macro Lett.* **2014**, 3, 703.
- [21] J. A. Paquette, S. Ezugwu, V. Yadav, G. Fanchini, J. B. Gilroy, *J. Polym. Sci., Part A: Polym. Chem.* **2016**, 54, 1803.
- [22] G. Liu, B. Zhang, Y. Chen, C. X. Zhu, L. Zeng, D. S. H. Chan, K. G. Neoh, J. Chen, E. T. Kang, *J. Mater. Chem.* **2011**, 21, 6027.
- [23] H. J. Yen, H. H. Tsai, C. Y. Kuo, W. Y. Nie, A. D. Mohite, G. Gupta, J. Wang, J. H. Wu, G. S. Liou, H. L. Wang, *J. Mater. Chem. C* **2014**, 2, 4374.
- [24] L. M. Chen, Z. Xu, Z. Honga, Y. Yang, *J. Mater. Chem.* **2010**, 20, 2575.
- [25] V. S. Fomenko, in *Handbook of Thermionic Properties: Electronic Work Functions and Richardson Constants of Elements and Compounds* (Ed: G. V. Samsonov), Plenum Press Data Division, NY **1966**, p. 10.
- [26] A. Facchetti, T. Marks, *Transparent Electronics: From Synthesis to Applications*, John Wiley and Sons Ltd, West Sussex, UK, **2010**, p.357.
- [27] J. H. Kim, J. H. Hwang, J. Suh, S. Tongay, S. Kwon, C. C. Hwang, J. Wu, J. Y. Park, *Appl. Phys. Lett.* **2013**, 103, 171604.
- [28] J. P. Doering, *J. Chem. Phys.* **1969**, 51, 2866.
- [29] A. Hiraya, K. Shobatake, *J. Chem. Phys.* **1991**, 94, 7700.
- [30] S. H. Simon, *The Oxford Solid State Basics*, Oxford University Press, Oxford, UK **2013**.

- [31] L. P. Kouwenhoven, D. G. Austing, S. Tarucha, *Rep. Prog. Phys.* **2001**, 64, 701.
- [32] F. L. Urias, E. C. Silva, E. M. Sandoval, M. Terrones, H. Terrones, *J. Mater. Chem.* **2008**, 18, 1535.
- [33] G. Fanchini, A. Tagliaferro, *Diamond Relat. Mater.* **2001**, 10, 191.
- [34] C. Musumeci, A. Liscio, V. Palermo, P. Samori, *Mater. Today* **2014**, 17, 504.
- [35] J. T. Price, J. A. Paquette, C. S. Harrison, R. Bauld, G. Fanchini, J. B. Gilroy, *Polym. Chem.* **2014**, 5, 5223.
- [36] N. F. Mott, E. A. Davis, *Electronic Processes in Non-Crystalline Materials*, Oxford University Press, Oxford, UK **1979**.
- [37] H. S. Nalwa, in *Handbook of Low and High Dielectric Constant Materials and Their Applications* (Ed: H. S. Nalwa), Academic Press, London, UK, **1999**.
- [38] M. Lanza, *Materials* **2014**, 7, 2155.
- [39] J. B. Gilroy, S. D. J. McKinnon, P. Kennepohl, M. S. Zsombor, M. J. Ferguson, L. K. Thompson, R. G. Hicks, *J. Org. Chem.* **2007**, 72, 8062.
- [40] S. Ezugwu, *Synthesis and characterization of copper nanoparticles and copper-polymer nanocomposites for plasmonic photovoltaic applications*. MSc Thesis, Univ of Western Ontario, London, ON Canada **2012** (see also <http://ir.lib.uwo.ca/etd/1025>)
- [41] F. Sharifi, R. Bauld, M. S. Ahmed, G. Fanchini, *Small* **2012**, 8, 699.
- [42] F. Pashaei, F. Sharifi, G. Fanchini, F. Lagugne-Labarthe, *Phys. Chem. Chem. Phys.* **2015**, 17, 21315.
- [43] A. Akbari-Sharraf, S. Ezugwu, M. S. Ahmed, M. G. Cottam, G. Fanchini, *Carbon* **2015**, 95, 199.

Chapter 6

Electrical, Optical and Thermal properties of P6OV:Graphene nanocomposites

In the previous chapter we discussed in detail the properties of poly-[1,5-diisopropyl-3-(cis-5-norbornene-exo-2,3-dicarboxiimide)-6-oxoverdazyl] (P6OV) with emphasis on their electrical bi-stability and we showed the physical mechanisms as well as the most promising structural design that leads to ultrathin flash memory device from organic polyradicals. In this chapter, we investigate the optical, electrical, morphological and thermal properties of nanocomposites formed by the incorporation of P6OV into graphene-based thin films. The work presented in this chapter is motivated by the world-wide need for advanced composites materials, for instance, polymer-based nanocomposites for thermal management applications [1-3]. Polymer based materials are especially needed in applications where light weight is desirable, such as in modern day aerospace structures [4].

In the first section of this chapter, we will discuss the fabrication of nanocomposite thin films produced by spin coating P6OV on graphene-based thin films deposited by vacuum filtration of exfoliated nanographite. Same thickness of P6OV will be coated on graphene-based thin films of different fraction, f of substrate covered area. In order to understand the effect of addition of graphene of different fraction of covered area f , we characterized the graphene samples with and without P6OV coatings.

6.1 Experimental

6.1.1 Thin film deposition

Graphene solution was made by surfactant-assisted exfoliation of nanographite described in details in chapter one [5]. We controlled the fraction of graphene platelets deposited on the

substrate by using different volumes of graphene/RNA suspension, from 5 ml to 40 ml. The suspensions were vacuum filtered onto 0.22 μm sacrificial (GSWP Millipore) filter membrane using the filtration set-up described in chapter one. Membranes loaded with graphene flakes were transferred to the glass substrate and dried in the oven at 60°C for 4 hours. The filter paper was then etched off in acetone and methanol baths leaving only the graphene on glass. These samples were subsequently annealed using a hot plate at 540°C for an hour inside glove box.

In order to enhance the electrical conductivity of our graphene-based thin films, we employed the procedure described by Parekh et al [6] for post-deposition treatment of the samples. The graphene thin films deposited on glass substrates were treated in nitric acid (HNO_3) and thionyl chloride (SOCl_2) by sequentially submerging the samples in the solution. The samples were dried gently with air after the $\text{HNO}_3/\text{SOCl}_2$ baths. To eliminate residual chemicals, samples were again submerged in water bath in 5 consecutive steps, dried with air and subsequently annealed at 540° C for 20 minutes inside the glove box. The resulting transparent and conducting graphene-based thin films on glass were then used as the substrate for coating P6OV to form P6OV/graphene composites.

The solution of P6OV was prepared by dissolving 12.5 mg of the polymer in 1 ml of anhydrous chlorobenzene. The solution was stirred overnight at 50 °C, filtered through 0.45 μm pore size syringe filters and spun on graphene/glass substrate. In order to promote adhesion, the P6OV solution was allowed to rest on the graphene/glass substrate for 2 minutes before spinning for 1 minute at 4000 rpm. The optimized thicknesses of P6OV were obtained by spin coating solution of the polymer on glass substrate at different spinning speeds. These thicknesses were measured by atomic force microscopy [7]. In order to perform the thickness measurements, part of the substrate was masked prior to spinning the polymer. The mask was then removed and

samples were analyzed in contact-mode using the Witec Alpha300S AFM microscope, from which topography profiles of the step in the correspondence of the masked area were obtained. **Figure 6.1** shows that the sample deposited on glass at spinning speed of 4000 rpm is about 10 nm thick. All the graphene-based samples studied in this chapter were coated with P6OV at 4000 rpm, which leads to the variation of only the fraction of the substrate covered with graphene-based platelets.

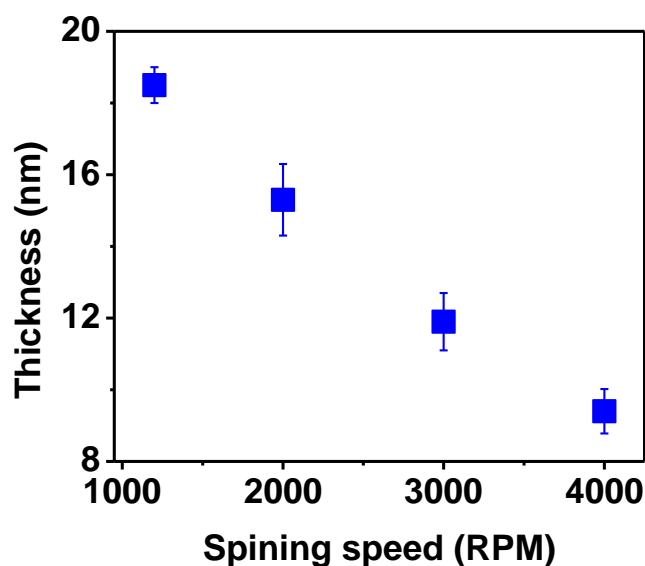


Figure 6.1: Variation of the thickness of P6OV films with the spin coating speed. P6OV was deposited on bare glass substrate for thickness optimization.

6.1.2 Characterization of P6OV/Graphene nanocomposites

The graphene-based thin films deposited on glass substrate were characterized prior to and after coating with P6OV. Optical images were taken to determine the fraction of the substrate covered with graphene-based platelets as a function of the filtration volume of graphene suspension. The sheet resistance of graphene with and without P6OV coating were

measured from current – voltage (I-V) curves recorded at room temperature using a Keithley 2400 source meter attached to a four-point probe station. Voltages in the ± 2.5 V range were applied in order to obtain I – V characteristics of the samples. Four-point probe experiments and measurements at different distances between the electrodes were performed in order to rule out the presence of a significant contact resistance between the contacts and the films. UV–vis transmittance of the samples was measured at normal incidence in a range of wavelengths between 380 nm and 500 nm using a Varian DMS80 spectrometer. This wavelength range was specifically chosen to cover the low intensity absorption peak observed in P6OV [8]. The thermal images of the samples were obtained using the near field scanning thermoreflectance imaging (NeSTRI) techniques described in details in chapter two. The topography, SNOM images and the phase and amplitude of the thermal images were recorded simultaneously during the NeSTRI scans.

6.2 Optical images and transmittance of Graphene and P6OV/Graphene nanocomposites

In this section the results of the optical images of graphene-based platelets deposited on glass substrate from different filtration volume of graphene suspension and the UV-Vis transmittance of the samples are presented. Optical microscope equipped with a 20x long working distance objective is used to obtain the images of graphene platelets deposited on glass substrates from different filtration volumes. Although optical microscope gives a relatively low resolution images compared to modern scanning probe microscopy techniques, the images obtained using optical microscope can advantageously cover a larger surface area of the sample than can be acquired using scanning probe techniques. In the specific case where high resolution images are not extremely important, such as obtaining the statistics of area of substrate covered

by samples the optical microscopes, provide on the microscale, images that correlate well with physical sample [9]. For the optical images of graphene-based platelets fabricated in this work, image J, a free program package for image processing and manipulation [10] was used to process the images to obtain the fraction of substrate area covered by the graphene platelets.

Figure 6.2 (a-d), show the images of graphene-based platelets on glass substrate measured with the optical microscope. In these figures, white color represents the graphene

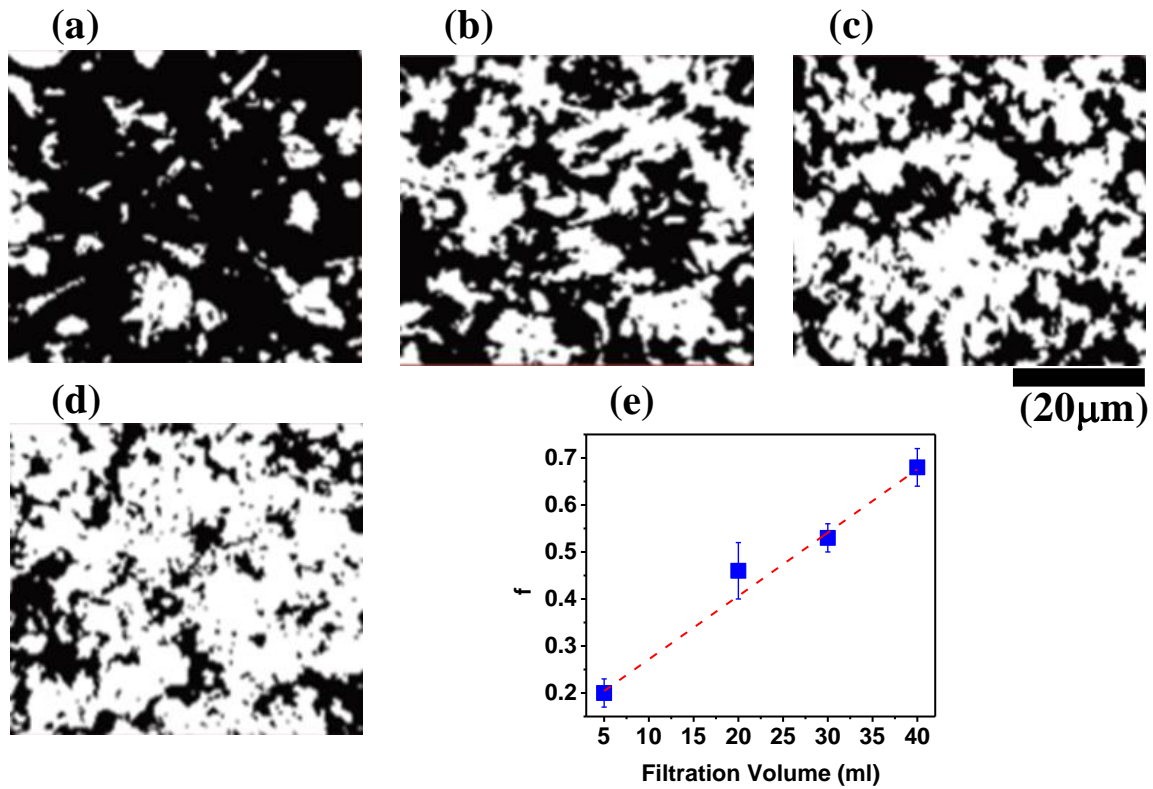


Figure 6.2: Optical images of graphene thin films deposited from different filtration volumes of (a) 5 ml (b) 20 ml, (c) 30 ml and (d) 40 ml. The optical images were processed using image J, an image processing package to obtain the fraction of the substrates covered by the graphene platelets. (e) Variation of graphene area fraction with the filtration volume.

platelets and black indicates voids or absence of graphene on the substrate. Assuming f is the fraction of glass substrate covered with graphene platelets, then $(1 - f)$ represents the fraction of voids on the same sample. A close observation of the images indicates that the area of the substrate covered by graphene platelets increases with the volume of solution used to prepare the samples, as expected. The coverage area as a function of filtration volume is reported in **Figure 6.2(e)** from where it can be observed that the fraction of covered area, f is linearly proportional to the filtration volume. **Figure 6.3** shows the AFM micrographs of same graphene samples after coating with P6OV at 4000 rpm. At this spinning speed, only about 10 nm of the polymer can be coated on the samples as demonstrated in Figure 6.1.

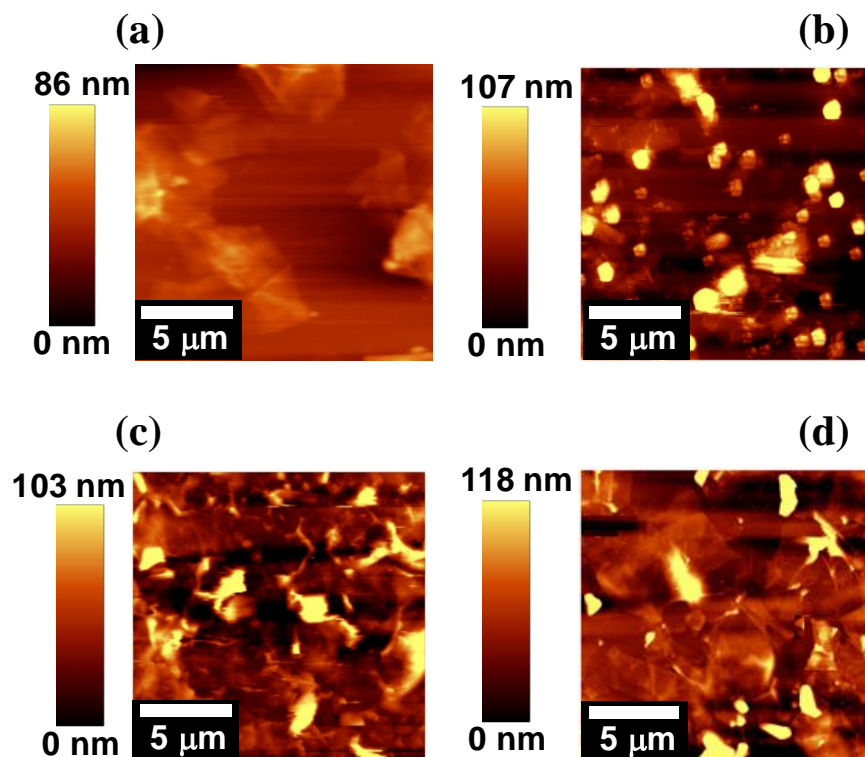


Figure 6.3: AFM topography of P6OV/graphene composites from different area coverage of graphene of (a) 0.20, (b) 0.46, (c) 0.53 and (d) 0.68

The AFM micrographs show that morphology of P6OV coated graphene platelets is affected by the fraction of covered area of the platelets. With small fraction of covered area ($f = 0.2$) the AFM micrograph shows that the P6OV forms a continuous layer and embeds sparse graphene platelets as in panel (a) of Figure 6.3. When $f \geq 0.56$, P6OV intermix with graphene and the polymer tends to isolate the graphene-based platelets, which also preserves the morphology of the platelets. However, panel b shows that P6OV coated on graphene of $f = 0.46$ forms agglomerates at the opposite of smooth films. While the reason for the topography difference is not clear since the conditions for the depositions were the same, such variation will offer us the opportunity to understand the morphological preference required for optimal performance and improved properties of our P6OV-based nanocomposites.

The optical transmittance of graphene-based thin films with and without P6OV is presented in **Figure 6.4**. Prior to coating with P6OV, the transmittance, T of the graphene-based samples, irrespective of the fraction of covered area, is nearly independent of the wavelength (dashed line in Figure 6.4). Similar observation has been reported for graphene thin films deposited from surfactant assisted exfoliation of graphite and is indicative of high transparency of graphene in the visible and near UV [11]. The behavior of the transmittance spectra is however different after coating with P6OV. Figure 6.4 shows a decrease in the transmittance spectra of the nanocomposites at around 400 nm wavelength. This is remarkable because the wavelength corresponds to the energy, $h\nu = 3.1$ eV in the optical absorption bands of P6OV at which we previously observed a SOMO \rightarrow LUMO and HOMO \rightarrow SOMO transitions [8]. These transitions involve only few charge carriers: electrons from the neutral SOMO levels are promoted to LUMO energy band upon absorption of photon energy, $h\nu = 3.1$ eV from the incident light and electrons from HOMO state being promoted to the SOMO level with the

formation of delocalized electrons in the LUMO and holes in the HOMO, respectively. Since SOMO states are few electron states, optical absorption associated with transitions to/from SOMO levels is expected to lead only to small changes in the transmittance of the samples as demonstrated in Figure 6.4.

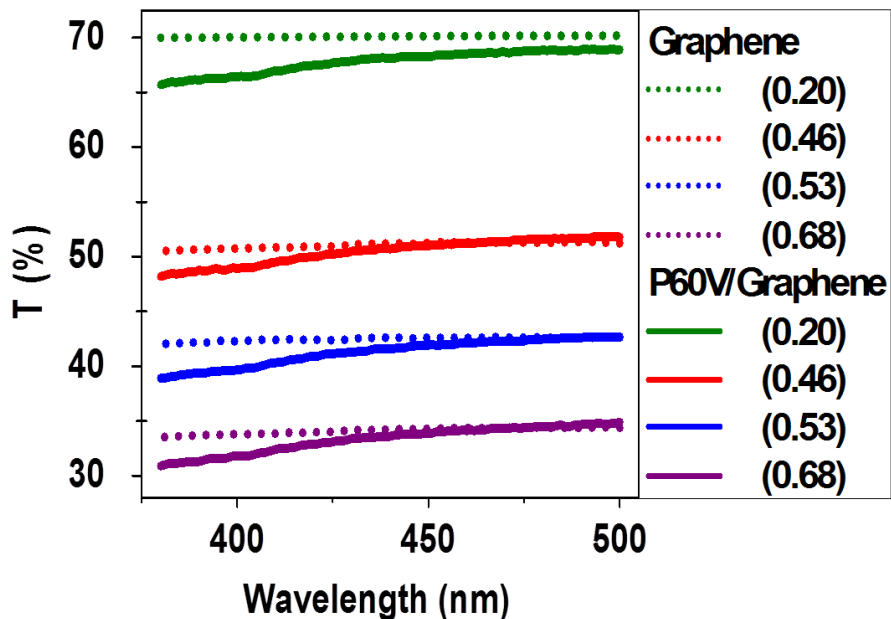


Figure 6.4: Optical transmittance of graphene thin films and P6OV/graphene nanocomposites measured in the wavelength range $\lambda = 380 - 500$ nm. This wavelength range was specifically selected to cover the previously observed SOMO-LUMO optical absorption peak in P6OV. The fraction of covered area is indicated on the right of the color code.

Figure 6.5 gives the value of the change in the transmittance at $\lambda = 400$ nm obtained from the difference in the transmittance values of P6OV/graphene nanocomposites and uncoated graphene-based thin films. The values of ΔT are very small as expected from P6OV coatings of extreme thinness and from the fact that the transitions involve the SOMO levels. However, the fact that ΔT is not constant with f is indicative of the amount of P6OV adsorbed on the surface of

graphene of different fractions of covered area. With $f \leq 0.2$, P6OV tends to form a continuous film around a few graphene platelets that results in a significant optical absorption in this sample. Phase segregation of P6OV solution to solid-state agglomerate during spinning operation on graphene platelets with $f = 0.46$ leads to the out of trend shift in the measured optical transmittance.

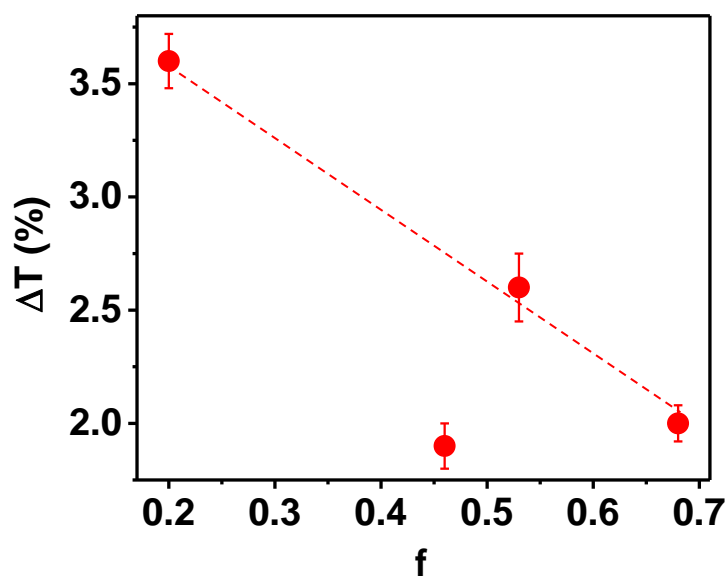


Figure 6.5: Change in transmittance, ΔT of graphene thin films without and with P6OV as a function of fraction, f of graphene covered area. ΔT was determined at the wavelength $\lambda = 400$ nm in which P6OV show significantly higher absorption due to SOMO \rightarrow LUMO and HOMO \rightarrow SOMO transitions [6].

The observed differences in the value of ΔT can also be understood by considering that graphene thin films obtained from large filtration volume and consequently higher fraction of covered area are less transparent which is indicative of significantly higher thickness. The fact

that the top surface of the sample at $f \geq 0.46$ is formed by floating graphene platelets is evident from the AFM micrographs, demonstrated previously in Figure 6.3, where the z-scale is comparatively high. Consequently, more graphene platelets are loosely attached to graphene layer below it by weak van der Waal force that can be detached during spin-coating of P6OV. This would lead to higher transmittance in the absence of any P6OV coating and consequently smaller ΔT .

6.3 Electrical conductivity of Graphene and P6OV/Graphene nanocomposites

Room-temperature sheet conductivity of our graphene-based samples with and without P6OV coating as a function of surface area covered by graphene platelets was determined from current – voltage characteristics obtained using a Keithley 2400 source meter. Voltages in the ± 2.5 V range were applied in order to obtain the current – voltage curves shown in **Figure 6.6**. The figures show that the measured current is linearly related to the applied voltage even after coating with P6OV, which is indicative that the ohmic conduction is preserved in the presence of thin layer of P6OV coating. In sandwich configuration, freshly fabricated P6OV sample is expected to exist in the low conductivity state in which the conduction mechanism obeys Poole – Frenkel electrical conduction model [8]. The fact that the I-V characteristics are ohmic shows that the electrical properties of the nanocomposites are dominated by the intrinsic high electrical conductivity of the graphene.

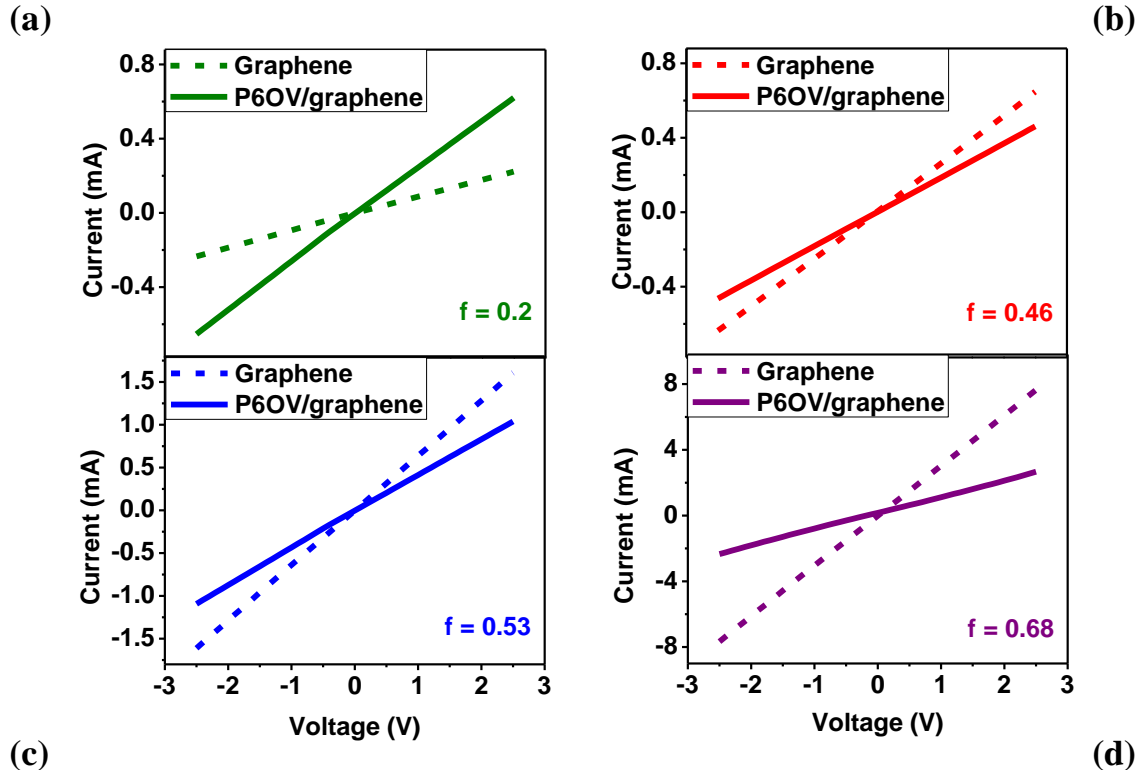


Figure 6.6: Current – voltage characteristics of graphene thin films and P6OV/graphene nanocomposites for different fraction of graphene covered area of (a) 0.2, (b) 0.46, (c) 0.53 and (d) 0.68.

The electrical transport in such graphene-based platelets is usually conceptualized in terms of the percolation theory [12, 13] as demonstrated in **Figure 6.7**. At a certain fraction of substrate area coverage, which is known as the percolation threshold (f_0), the graphene-based platelets form a network leading to a sudden change in the conductivity of the system from insulator to semi-metal conductor as conceptualized in panel (b) of Figure 6.7. In this and other materials of this kind, voids are also expected to play an important role in limiting the electrical transport of the sample. This is because, in view of percolation theory, no percolating pathway can be drawn through the sample if the critical threshold of covered area f_0 is not achieved. Consequently, graphene thin films of covered area, f less than the threshold, f_0 are expected to be

highly insulating, as depicted in Figure 6.7(a). If we neglect possible contribution of the contact resistance between platelets, the electrical conductivity can be found from the following relation [11, 13]:

$$K_{el} = S_0 \cdot (f - f_0)^n \quad (6.1)$$

where K_{el} is the sheet electrical conductivity of bulk graphene-based thin films, S_0 is the effective conductivity of a platelet and n is the critical exponent. From the current - voltage curves presented in Figure 6.6, we determined the sheet conductivity of both the graphene thin films and the nanocomposites as the inverse of the sheet resistance. In **Figure 6.8**, we show the sheet electrical conductivity (K_{el}) as a function of the fraction, f of surface area covered by graphene-based platelets with and without P6OV. The results of the conductivity presented in Figure 6.8(a) shows that the fraction of covered area strongly influences the electrical properties of the graphene-based films as we expected from eq. 6.1. As shown in this figure, eq. 6.1 is best fitted with $n = 1.8$, $S_0 = 400 \text{ S m}^{-1}$ and $f_0 = 0.32$.

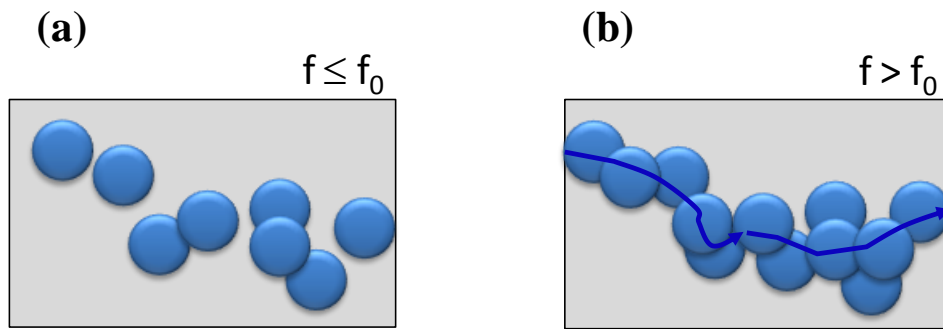


Figure 6.7: The conceptual representation of percolation of graphene-based platelets on the glass substrate - (a) about graphene percolation threshold, $f \leq f_0$, the films are mostly insulating and (b) above the threshold f_0 , the platelets form continuous conducting pathway along the substrate surface and the films have high electrical conductivity

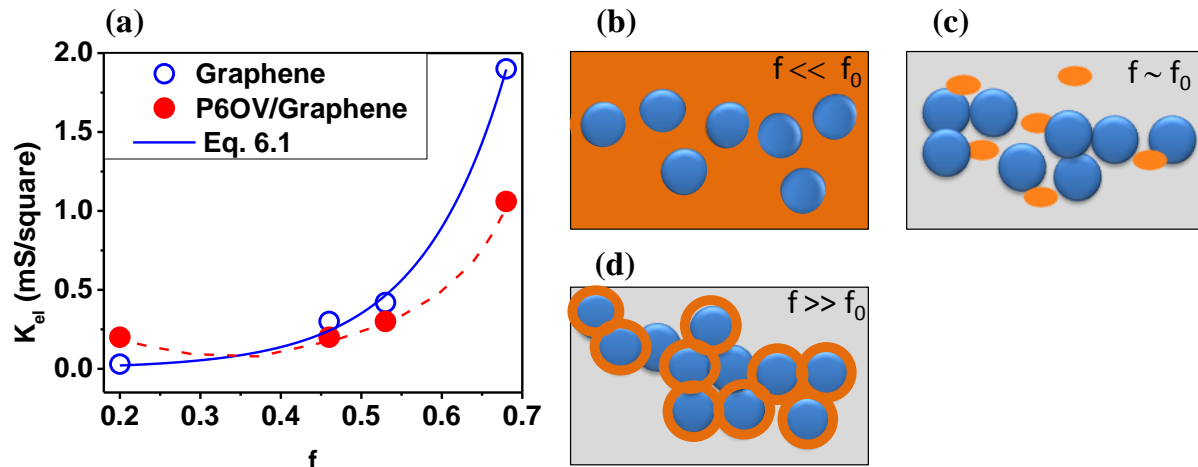


Figure 6.8: (a) Electrical conductivity (K_{el}) as function of the fraction, f of surface area covered by graphene platelets for graphene-based thin films (open dots) and P6OV/graphene nanocomposites (solid dots). Solid lines represent simulation of experimental data according to eq. 6.1. Restructuring of P6OV in a graphene-based film into three regions of (b) below graphene percolation threshold, in which P6OV forms a continuous layer embedding sparse graphene-based platelets, (c) about graphene percolation threshold, in which P6OV tends to aggregate and does not affect the electrical conductivity of the film and (d) quite above graphene percolation threshold, in which P6OV tends to isolate the graphene-based platelets, playing a detrimental role to the electrical conductivity.

Figure 6.8 also gives the sheet conductivity of the same graphene-based thin films after coating with P6OV. The electrical conductivity variation in the P6OV/graphene nanocomposites occurs in three stages, as illustrated in panels (b), (c) and (d) of Figure 6.8. Here, the process is explained in view of the morphological disparity of the polymer when coated on graphene-based platelets of different fraction of covered area. Below the graphene percolation threshold, the addition of thin layer of P6OV to sparse graphene platelets make the platelets contact to form effective conducting paths as in panel (b). In this morphological state, P6OV surrounds sparse

graphene platelets hence reducing the voids in the sample. Thus the polymer participates in the transport properties of the nanocomposites and improves the electrical conductivity of the sparse platelets as demonstrated in Figure 6.8 (a).

At higher graphene coverage area for which $f \sim f_0$, aggregate P6OV plays passive role and the electrical conductivity of the nanocomposites is nearly the same. This condition is described in panel (c) of Figure 6.8, where it can be seen that P6OV aggregates limitedly connect the graphene-based platelets. Going further, panel (d) demonstrates that at higher coverage area (quite above graphene percolation threshold) for which there is sufficient pathway for charge transport, the polymer imbeds the platelets and acting more as an insulating layer. In this morphology regime, all the graphene platelets tend to interlace with each other and only a thin P6OV layer of a few nm separates them. Transport between graphene platelets is therefore facilitated by the quantum mechanical tunneling and hopping between localized states situated at specific charged monomers along the polymer filament [14]. Since charge hopping is less efficient than free carrier transport, the electrical transport in the nanocomposites also becomes less efficient. This is responsible for the decrease in conductivity in the sample with the lowest $(I-f)$ voids shown in Figure 6.8(a).

6.4 Thermoreflectance imaging of P6OV/Graphene nanocomposites

The thermal parameters of P6OV/graphene nanocomposites, such as the amplitude and phase of thermoreflectance oscillations were studied using NeSTRI setup described in chapter two. NeSTRI allows direct nanoscale mapping of the transmittance and reflectance of the sample and consequently the absorbance, $A_0(x, y)$. The amount of heat $H(x, y)$ deposited at each point $(x,$

y) of the sample upon illumination with the pump beam is determined from the following relation:

$$H(x, y) = P_0 \cdot A_0(x, y) / D(x, y) \cdot \exp\{i\omega t\} \quad (6.2)$$

where $D(x, y)$ is the thickness of the absorbing film, determined from AFM topography referenced to the glass substrate, and $H_0(x, y) = P_0 \cdot A_0(x, y) / D(x, y)$ represents the amount of heat locally deposited per sample unit volume when uniformly illuminated at $P_0 = 0.05 \text{ mW}/\mu\text{m}^2$.

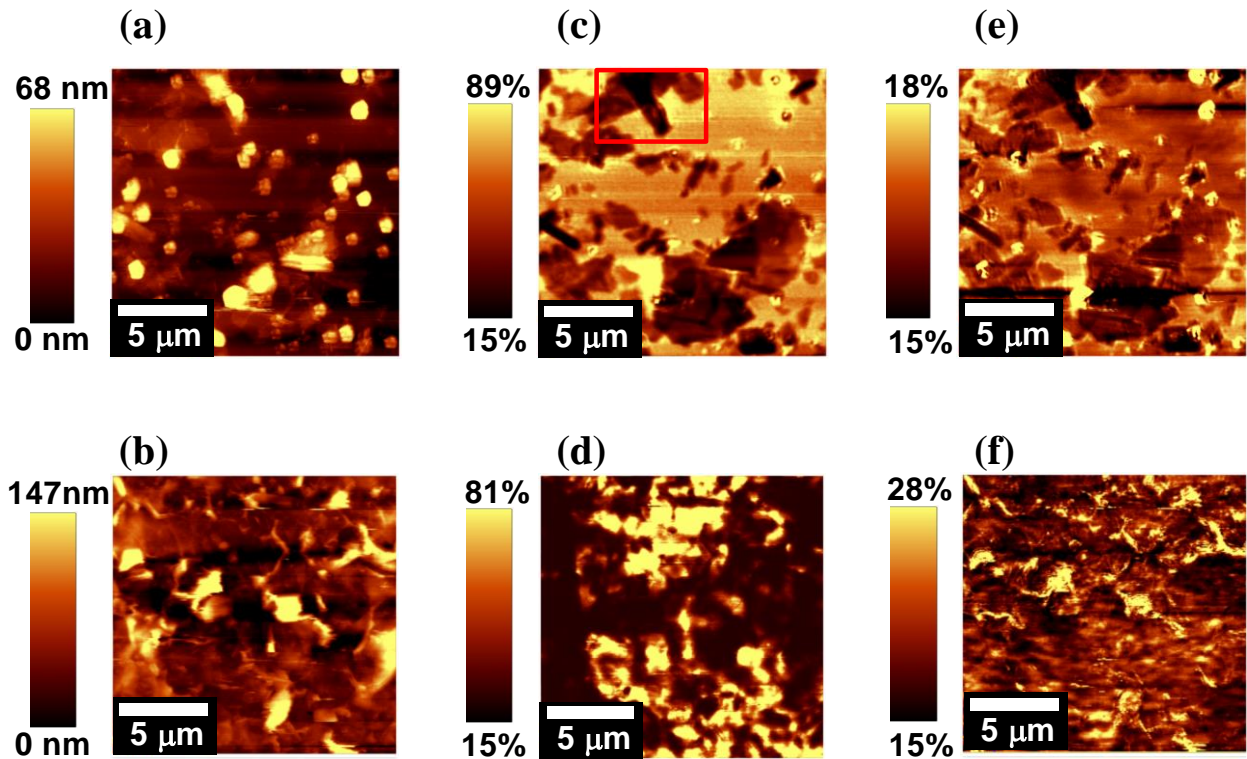


Figure 6.9: AFM topography (a, b), SNOM transmission (c, d) and (c) SNOM reflection images (e, f) of P6OV/graphene nanocomposites comprising of graphene platelet with $f = 0.46$ (top images; a, c, e) and $f = 0.53$ (bottom images; b, d, f). The topography was obtained simultaneously during SNOM measurements.

In **Figure 6.9**, we present the AFM topography, SNOM transmittance and reflectance images recorded on P6OV/graphene nanocomposites from the sample with different graphene area fraction of 0.46 (top images) and 0.53 (bottom images). The transmittance image in panels (c) and (d) provide the fraction of incident probe beam intensity transmitted through the sample at each point (x, y) . We observe from the images a good contrast between the transmittance in the region $(I-f)$, containing only thin layer of P6OV and the region, f covered with P6OV/graphene composites. Figure 6.9(e) and (f) show that the P6OV/graphene nanocomposites are only weakly reflecting. The SNOM data was normalized using the transmitted and reflected laser intensity from bare glass substrate. The nominal transmittance and reflectance of the glass substrate at the laser beam wavelength ($\lambda_p = 405$ nm) are 92% and 8% respectively [15]. Measurements at the same laser intensity for both samples and bare BK7 glass substrate were carried out to obtain a conversion factors. The absorbance, $A_0(x,y)$ of the sample was calculated via the relation

$$A_0(x,y) = I - \tau(x,y) - \rho(x,y) \quad (6.3)$$

where $\tau(x,y)$ and $\rho(x,y)$ are, respectively, the normalized transmittance and reflectance of the sample obtained from recorded SNOM data at 405 nm.

The information on the absorbance, in conjunction with the laser power P_0 , were used to determine the sample heating profile upon uniform illumination in each of the two samples shown in Figure 6.9. **Figure 6.10 (b)** provides a map of the amount of heat $H(x, y)$ typically deposited on P6OV/graphene nanocomposites computed using eq. 6.2. The left image of this figure is the mirror image of the platelets measured from the marked red box in Figure 6.9(c). The image of the heating profile shows that a significantly larger

amount of heat is deposited in the correspondence of graphene platelets. Since P_0 is reasonably constant, it can be inferred that, even at the nanoscale regime, the sample's absorption increases with the fraction, f of the substrate covered with graphene-based platelets, similar to the bulk transmittance data presented in Figure 6.5. In both samples, the oscillatory nature of the heating profile provides changes in the thermorefectance that give rise to measureable thermal parameters such as the amplitude and phase as we present them in the following paragraphs.

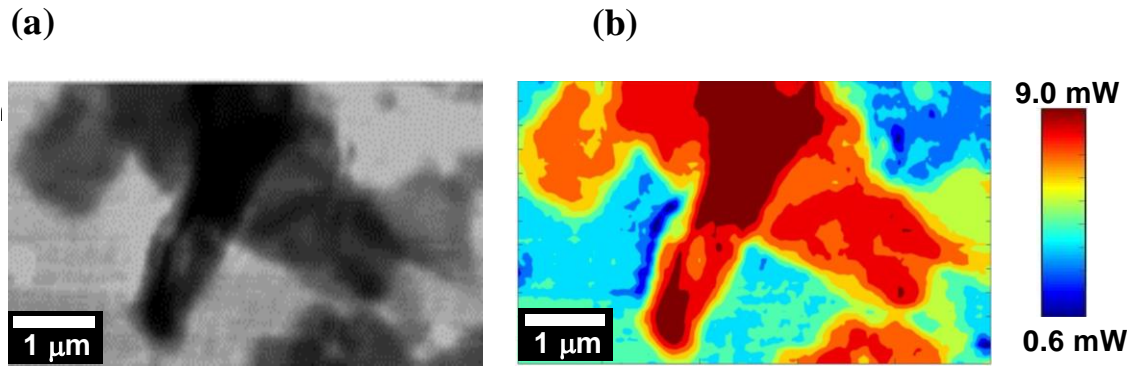


Figure 6.10: (a) Mirror image of graphene platelets indicated by rectangular box in Fig. 6.9(c) and (b) heat profile image of P6OV/graphene nanocomposite. Large amount of heat is generated in the correspondence of graphene platelet that can be attributed to more absorption of pump beam.

With NeSTRI, we detect the small changes in the amplitude and phase of the temperature profile from changes in the thermorefectance oscillations of the probe beam. **Figure 6.11** (a-d) is the result of our NeSTRI measurement on P6OV/graphene nanocomposites showing respectively, the thermal amplitude (top images) and phase (bottom images) of the temperature profile obtained at 105 Hz modulation of pump beam. The phase lag of the NeSTRI signal relative to the pump beam depends on the average mean free path of the thermal waves reaching

each point (x, y) from surrounding regions and consequently on the thermal diffusivity of the sample. Depending upon the thermal diffusivity of the material, a thermal wave generated at the sample surface as a consequence of illumination by a modulated pump beam, propagates to the adjoining air with a specific time delay. Figure 6.10 (c, d) shows that more delay is measured in the correspondence of the graphene platelets signifying that the lateral thermal diffusion lengths are smaller in this region. The ratio of the phase lag in the two samples with different graphene area coverage, $f(0.53)/f(0.46)$ is 0.16. This shows that the higher the graphene coverage area, the less the phase lags, so that heat generated at different points propagate faster with more graphene coverage. The contribution/effects of the polymer on the thermal properties of the samples is also evident from the aggregated P6OV in Figure 6.11 (c). The P6OV aggregates in this figure have high phase lag which implies low thermal diffusivity. However, some of the aggregates do not have low diffusivity, indicating they are possibly in a high-conductivity state [8].

The amplitude measured in the two samples have features that are comparatively different between the sample and within each sample as well. In line with our previous observation in chapter 2, the amplitude of NeSTRI signal is expected to directly depend on thermosreflectance oscillations due to periodic heating of air close to sample. From the illuminated region of sample, heat diffuses along the surface and to the adjoining air and the higher the thermal conductivity the larger the diffusion of heat along the surface of the sample. Heat is subsequently transferred from the nanocomposite surface to the adjoining air, which indicated that the amplitude of the NeSTRI signal, at a constant absorption coefficient of the film, is proportional to the thermal conductivity, K_{th} . The results of our NeSTRI presented in Figure 6.11 shows that at higher f , phase is normally more homogenous while the amplitude is higher, indicating higher thermal conductivity. It can be concluded that, since the sheet

conductivity show the polymer in high-state, the observed high amplitude and consequently higher K_{th} indicates that P6OV diminishes the contact thermal resistance between graphene platelets. On the other hand, a comparison of the amplitude of the two samples averaged over the entire image, show that the sample with higher graphene coverage area is higher by 7x.

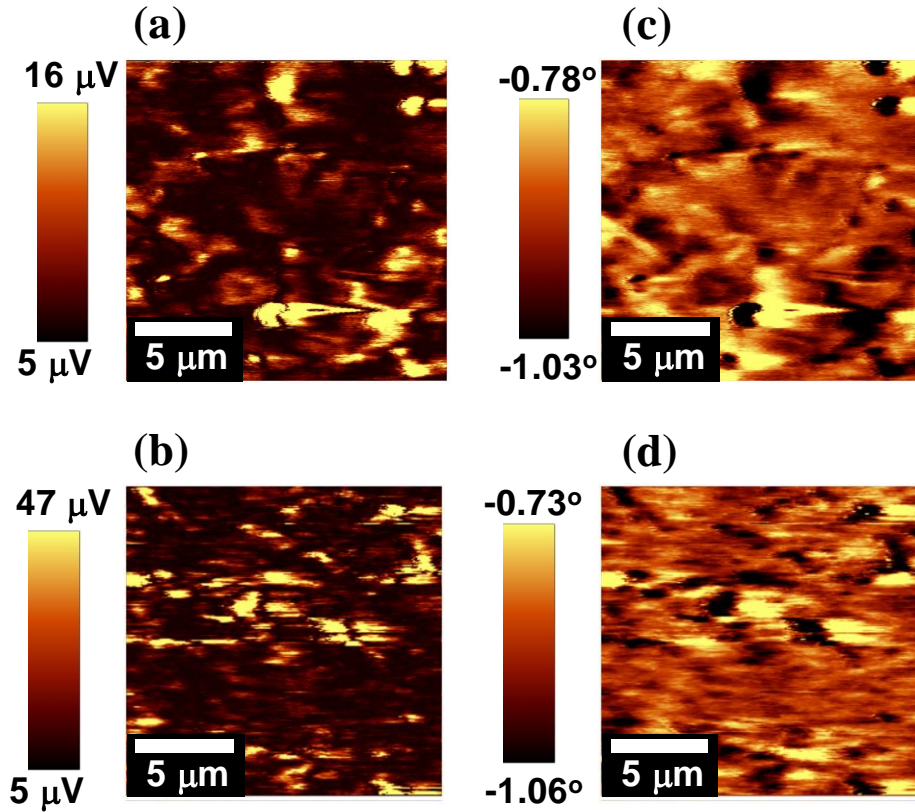


Figure 6.11: Thermal amplitude (a, b) and Phase (c, d) of P6OV/graphene nanocomposites, comprising of graphene platelet with $f = 0.46$ (top images; a, c) and $f = 0.53$ (bottom images; b, d). These images were obtained during the NeSTRI scan at a pump beam modulation frequency of 105 Hz.

6.5 Conclusion

In this chapter, we studied the thermophysical properties of nanocomposites formed by incorporation of P6OV via spin coating the polymer onto graphene platelets. The thickness of the polymer was kept constant by coating the film at the same deposition condition while varying the thickness of the base graphene-based thin films. P6OV/graphene nanocomposites show slight decrease in the optical transmittance at wavelength, $\lambda \leq 400$ nm in which the polymer is known to experience light absorption due to SOMO \rightarrow LUMO and HOMO \rightarrow SOMO transitions. The electrical conductivity of the base graphene thin films increased with increasing coverage area of graphene platelets, consistent with percolation theory predictions. The calculated threshold of covered area f_0 required to provide minimum pathway for electrical conduction was 32% of the substrate surface. However, coating with P6OV decreased the conductivity in sample in which graphene coverage area is more than 50%.

NeSTRI studies shows that phase of the modulated thermosreflectance images are, in general, more homogenous with high f , the fraction of graphene covered area. However, some of the P6OV form aggregates with relatively higher diffusivity that can presumably be associated with high electrical-conductivity-state in the polymer. In this high state, the polymer tends to diminish the inter-platelet thermal resistance thereby increasing the thermal conductivity and consequently high thermal amplitude. The associated future work would be to design a suitable device architecture that would permit tuning the electrical conductivity of the P6OV from low conductivity state to high state and to study the thermal properties in the two states. This could serve as thermal switch for next generation electro-thermal devices.

References

- [1] Y. Lee, D. Kim, J. Seo, H. Han, S. B. Khan, *Polymer International* **2013**, 62(9), 1386
- [2] H. Fukushima, L. T. Drzal, B. P. Rook, M. J. Rich, *J. Therm. Anal. Cal.* **2006**, 85, 235
- [3] P. C. Ma, N. A. Siddiqui, G. Marom, J. K. Kim, *Composites: Part A* **2010**, 41, 1345
- [4] M. Peters, C. Leyens, *Materials Science and Engineering – Vol. III – Aerospace and Space Materials In Encyclopedia of Life Support Systems (EOLSS)*
- [5] F. Sharifi, R. Bauld, M. S. Ahmed and G. Fanchini, *Small*, **2012**, 8, 699
- [6] B. B. Parekh, G. Fanchini, G. Eda, M. Chhowalla, *Appl. Phys. Lett.* **2007**, 90, 121913
- [7] S. Ezugwu, M.S. Ahmed, R. Bauld, R. Divigalpitiya, G. Fanchini, *Thin Solid Films*, **2013**, 534, 520
- [8] S. Ezugwu, J. A. Paquette, V. Yadav, J. B. Gilroy, G. Fanchini. *Adv. Electron. Mater.* **2016**, 1600253, DOI: 10.1002/aelm.201600253
- [9] J. M. Atkin, S. Berweger, A. C. Jones, M. B. Raschke, *Advances in Physics*, **2012**, 61(6), 745
- [10] Web resource: <http://rsb.info.nih.gov/ij/>
- [11] M. S. Ahmed, S. Ezugwu, R. Divigalpitiya, G. Fanchini, *Carbon*, **2013**, 61, 595
- [12] I. Mutlay. L. B. Tudoran, *Fullerenes, Nanotubes, and Carbon Nanostructures* **2014**, 22, 413
- [13] L. Hu, D. S. Hecht, and G. Gruner, *Nano Letters*, **2004**, 4, 2513

- [14] J. A. Paquette, S. Ezugwu, V. Yadav, G. Fanchini, J. B. Gilroy. *J. Polym. Sci., Part A: Polym. Chem.* **2016**, 54, 1803
- [15] Web resource: <http://www.crystran.co.uk/optical-materials/optical-glass-n-bk7-and-others>

Chapter Seven

Conclusion and Future work

7.1. Conclusions

In this thesis, we presented the results of our studies on the thermal and electronic properties of graphene-based thin films and organic polyradicals. The near field scanning thermoreflectance imaging (NeSTRI) we developed in this thesis work was employed to investigate at nanoscale, the thermal properties of thin films of graphene and graphene based nanocomposites. Using NeSTRI, we determined the thermal conductivity of micrometre-size multilayer graphene platelets to be about 600 W/m/K, consistent with theoretical predictions. We also find that the thermal conductivity is locally higher at specific crystallographic edges of multilayer graphene platelets, which is indicative of the spatial resolution of our method. NeSTRI measurements on large area graphene platelets decorated with copper nanoparticles (Cu-NPs) shows that the nanoparticles suppress the thermal conductivity of graphene due partly to the interfacial thermal resistance arising from poor thermal coupling between graphene and copper nanoparticles.

On the electronic properties of graphene decorated with copper nanoparticles, we developed the physical framework for understanding graphene doping by metallic nanoparticles. We showed that large contacts are less effective at modifying the band structure of graphene in comparison with an ensemble of many particles randomly distributed on the graphene surface. We employed a modified tight-binding model to investigate the influence of Cu-NPs on the band structure and work function of graphene. Local variations in the graphene work function due to the presence of Cu-NPs break the electron-hole symmetry of graphene shifting the Fermi level away from the Dirac point, effectively doping graphene even in the absence of charge transfer or

chemical bonding. Our calculations are in agreement with SKPFM experiments and show that Cu-NP area coverage is the most important factor in controlling the decrease of the work function of graphene in the presence of Cu, as well as the subsequent decrease in electrical resistivity. We also demonstrated that the electrical transport of graphene-based thin films in the presence of Cu-NPs is controlled at room temperature by a Poole Frenkel mechanism. A unique advantage conferred by Cu-NP doping is evident when we compare the electrical conductivity of doped and undoped graphene thin films. For a graphene film with $f_j = 18\% \pm 5\%$ area coverage of Cu-NPs, the transmittance reduces by only $\sim 9\%$, while its conductivity increases by more than 400%. In addition to the enhanced conductivity and the preservation of transparency, the presence of Cu-NPs gives rise to surface plasmon bands, which can be used for wide range of applications, including plasmon enhanced solar cells and surface-plasmon sensors.

In chapter five, we presented a design criterion for ultrathin memristors based on a homogeneous active layer made out of poly-[1,5-diisopropyl-3-(cis-5-norbornene-exo-2,3-dicarboxiimide)-6-oxoverdazyl] (P6OV), a polyradical. The devices we fabricated utilized a sandwich configuration with aluminum–calcium bilayers as anode material, and we investigated four cathode materials at different work functions, ranging from $\phi = 4.7$ eV for ITO electrodes to $\phi = 3.1$ eV for calcium–aluminum bilayers. The energy levels of the positive, neutral, and negative charge states of P6OV have been determined from a combination of UV–vis and KPFM measurements. The behavior of the SOMO energy level of P6OV at different degrees of charging could be understood in the framework of the Hubbard model by assuming a correlation energy $U = 0.8$ eV. Knowledge of the positive, neutral and negative energy levels were vital to configure our memristor architectures for maximum performance. Current–voltage characteristics show that a high-conductivity regime can be created, and subsequently eliminated

by applying an erase voltage to the devices of the order of $V_E \approx 4U/e$. Resistivity in the high-conductivity regime was found to be lower for ITO-based devices, in which the work function of the cathode matches the surface potential of positively charged P6OV radicals: $\phi_{\text{ITO}} = \varepsilon_{(+)} = 4.7$ eV. In the other three types of devices, with FLG, Al and Ca/Al cathodes, and $\phi < \varepsilon_{(+)}$, the “on” current decreased at decreasing work function of the cathode. In the low-conductivity regime, the resistivity of P6OV memristors was determined by the contact resistance between the SOMO energy of neutral P6OV and the cathode. Consequently, the electrical conductivity was higher for devices with cathodes of pure aluminum, with work function $\phi_{\text{Al}} = \varepsilon_{(0)} = 4.0$ eV, but lower in the other types of devices with FLG, ITO, and Ca/Al cathodes, as the mismatch between the SOMO level $\varepsilon_{(0)}$ and the cathode work function increases. We demonstrated that the electrical bistability of the devices is due to two distinct transport regimes in P6OV, extended states and Poole–Frenkel.

Optimized flash memory effects were demonstrated in Al/Ca-P6OV-ITO, in which the energy levels of the positively and negatively charged states of the polyradical align, respectively, to the cathode and anode work functions. More than 10^3 s of write–read–erase–read cycles were performed without significant current degradation. Conversely, Al/Ca-P6OV-Al devices, in which the cathode work function aligned with the neutral energy level of P6OV, exhibited WORM effects. Our results demonstrate the critical importance of energy-level matched electronic structures as the basis on which ultrathin, single-layer memristors can be successfully implemented.

In chapter six, we presented the results of the optical, electrical and thermal characterization of nanocomposites fabricated by coating a thin layer (thickness ~ 10 nm) of P6OV on graphene-based platelets of different fraction of substrate covered area. The optical

transmittance of the nanocomposites shows a marked decrease in the transmittance spectra due to absorption at $h\nu = 3.1$ eV photon energy, corresponding to the SOMO→LUMO and HOMO→SOMO transitions in the polyradical. Changes in the optical transmittance, ΔT between the P6OV coated and uncoated graphene-based thin films shows a preferential adsorption of the polyradical on the surface of graphene of different fractions of covered area. The electrical and thermal properties of the nanocomposites were similarly discussed in view of graphene area fraction.

The benefit of P6OV coating on the electrical conductivity manifests only when the fraction of graphene covered area, f is slightly below the percolation threshold f_0 . In this regime, the sheet electrical conductivity increases by over 500 % as a result of P6OV providing an effective conducting paths between sparse graphene-based platelets. However, at higher graphene coverage area for which $f \geq f_0$, P6OV imbeds the platelets and tends to acts as an insulating layer between contacting platelets. On the other hand, the polymer tends to diminish the inter-platelet thermal resistance thereby increasing the thermal conductivity which resulted in increased thermal amplitude measured by NeSTRI. The fact that the electrical conductivity increased significantly at lower f by incorporating P6OV of only few nanometer thickness provides the means of cost reduction in fabricating polymer/graphene nanocomposites.

7.2. Future Work

The NeSTRI we developed in this thesis work is a material characterization technique that facilitates investigation of thermal properties of low dimensional and nanostructured systems. Heat generated in the sample upon illumination with pump beam is transferred to the adjoining air causing a change in its refractive index that is detected via thermoreflectance

technique. To increase the resolution and efficiency of the thermoreflectance detection, it would be ideal to replace air with photothermal fluid that has a high temperature coefficient of refractive index. This would increase the sensitivity of thermoreflectance detection and consequently enable measurement of very thin samples such as soft biological samples due to the non-destructive nature of our NeSTRI. Automating the setup would also enhance its capability and data collection can be achieved at a range of incident photon energies, a range of modulation frequencies of excitation beam and a range of incident beam powers.

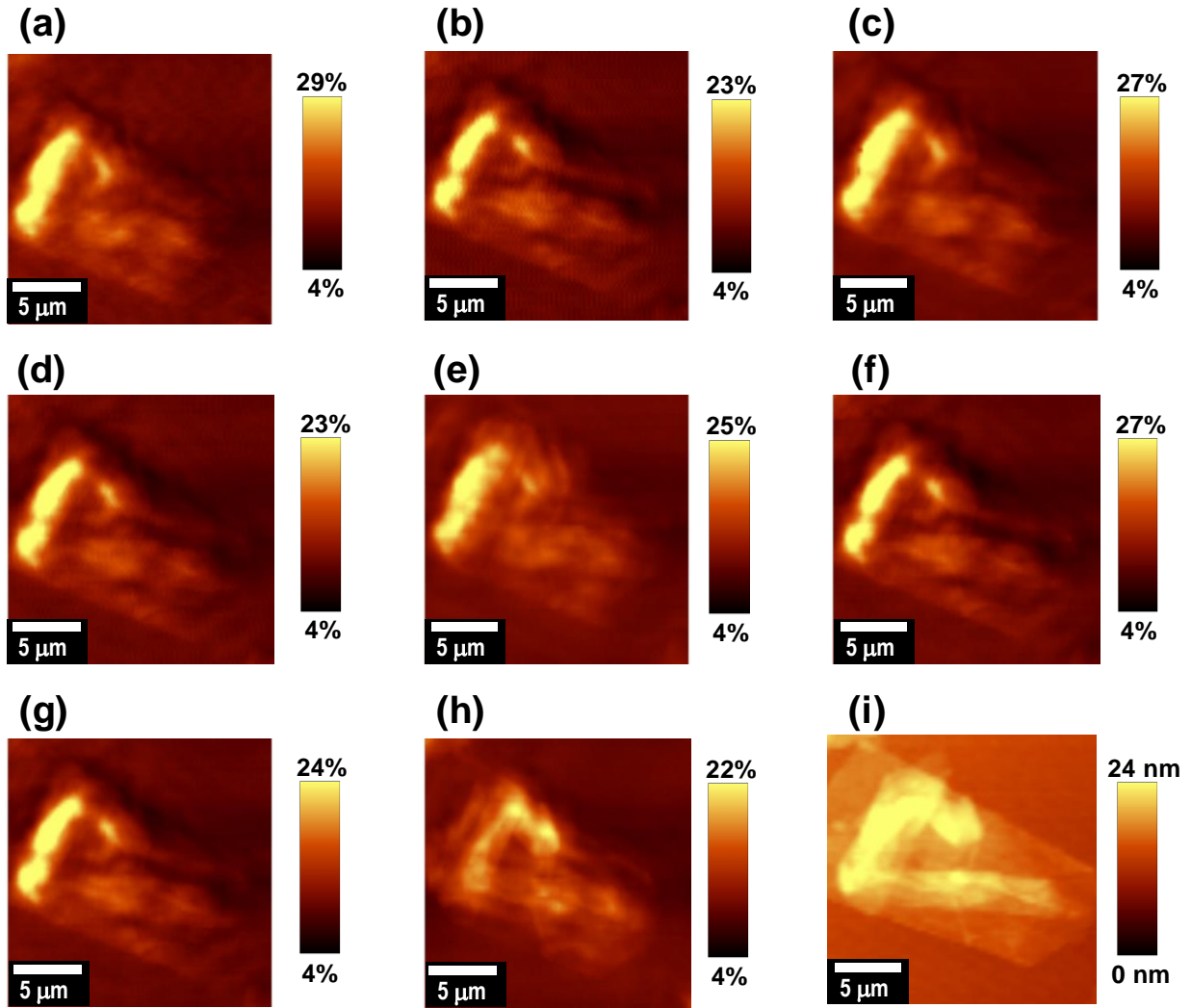
Although switching effects have been demonstrated by us in a sandwich configuration, conducting AFM will be essential as a future tool for probing memory switching effects in P6OV at the nanoscale. Conducting AFM measurements are particularly challenging in this system because of the thinness of the soft polyradical samples, which are easily damaged by the AFM tip when working in contact-mode as required by conducting scanning probe measurements. Native oxide at the AFM tip surface may also affect spin polarization. This is a very critical issue in radical polymers in which transport is highly spin polarized, as clearly shown by us in Figure 5.6. Nanoscale transport and conducting AFM measurements in polyradical memory devices can be the subject of future work.

In another important follow-up to our work on organic polyradicals, we are proposing the fabrication of bi-stable thermal device from P6OV as an active electro-thermal material. This is in line with the observed electrical bistability exhibited by P6OV polyradicals. We anticipate that a more detailed study on the thermal properties of P6OV in the two electrical conductivity regimes may lead to a breakthrough in polymer based electro-thermal devices with bistable thermal properties. This would require careful architectural design that facilitates in-situ

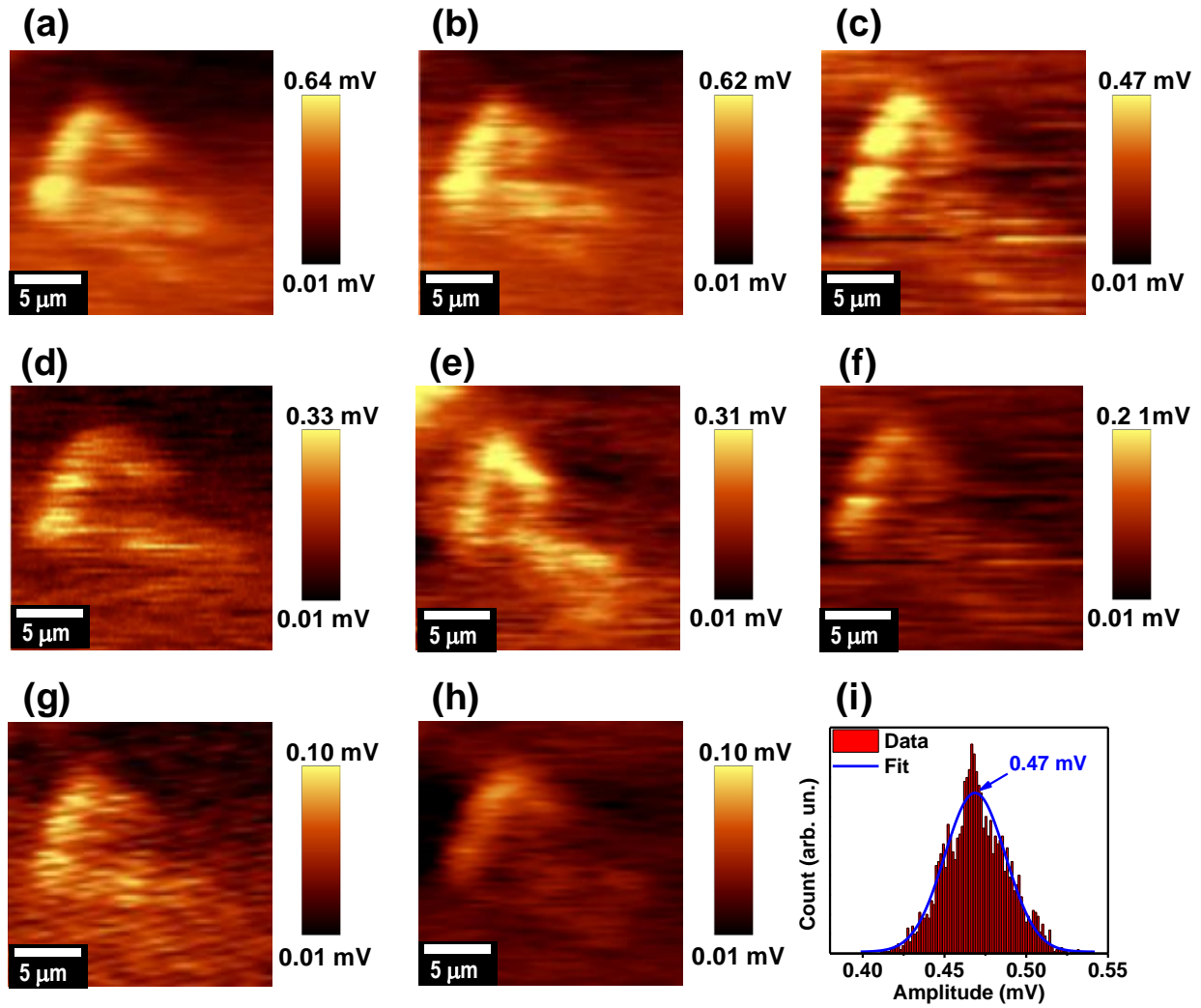
electrical switching of the device while performing nanoscale thermal measurement. The device can potentially be used as thermal switch in a variety of applications.

Appendix A:

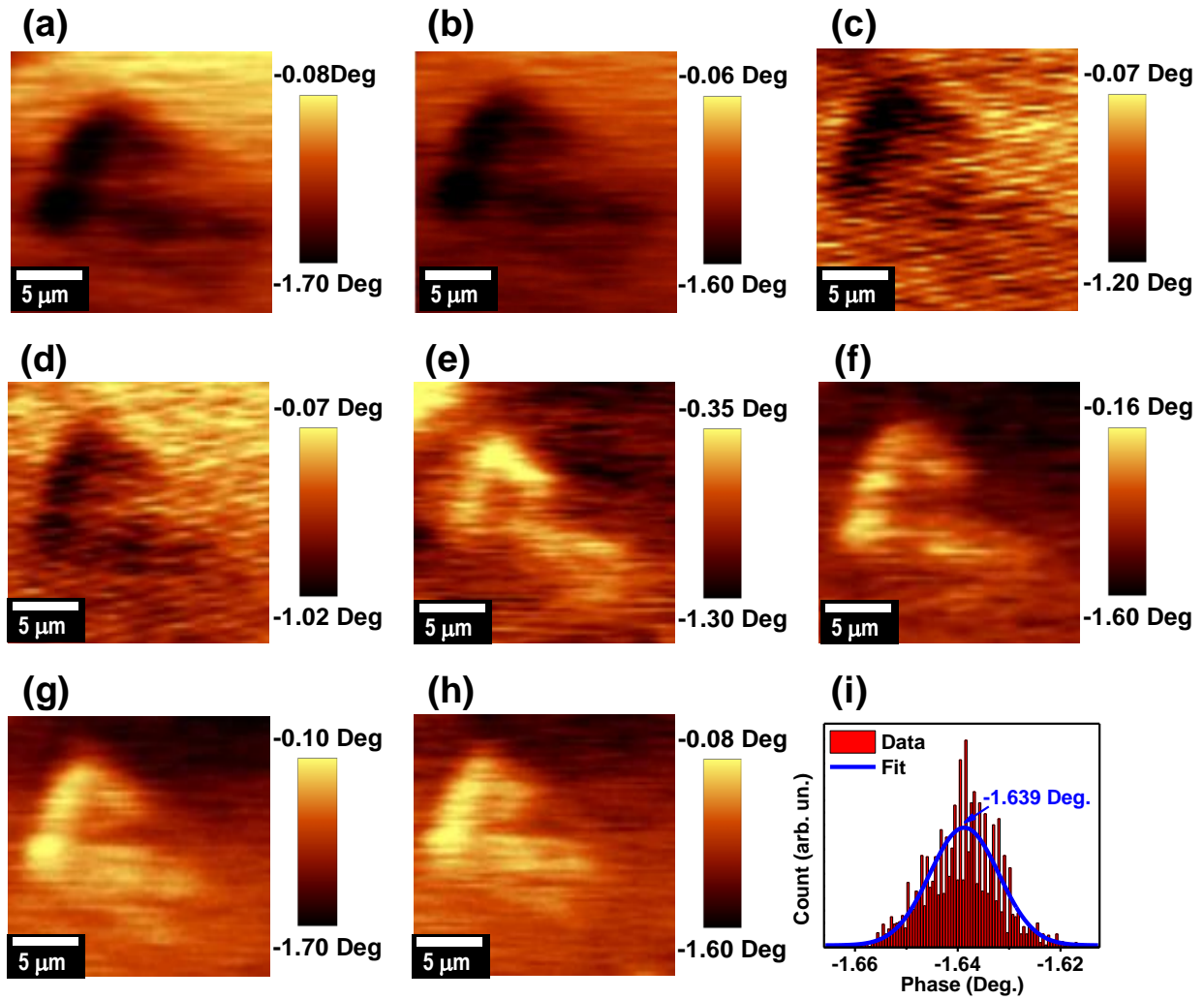
Complementary Images to Chapter 2



SNOM reflectance images at different frequencies of (a) 25 Hz, (b) 75 Hz, (c) 105 Hz, (d) 135 Hz (e) 150 Hz (f) 200 Hz (g) 250 and (h) 350 Hz (i) The corresponding AFM topography of the same sample



NeSTRI amplitude images at different frequencies of (a) 25 Hz, (b) 75 Hz, (c) 105 Hz, (d) 135 Hz (e) 150 Hz (f) 200 Hz (g) 250 and (h) 350 Hz (i) Typical Gaussian fit on the amplitude data. The peak of the Gaussian fit is taken as the representative value for the data.



NeSTRI phase images at different frequencies of (a) 25 Hz, (b) 75 Hz, (c) 105 Hz, (d) 135 Hz (e) 150 Hz (f) 200 Hz (g) 250 and (h) 350 Hz (i) Typical Gaussian fit on the phase data. The peak of the Gaussian fit is taken as the representative value for the data.

Appendix B:

Copyright permissions

In this appendix, all the permissions granted from publishers for reusing figures, tables, and texts are presented.

ELSEVIER LICENSE TERMS AND CONDITIONS

Nov 02, 2016

This Agreement between Sabastine Ezugwu ("You") and Elsevier ("Elsevier") consists of your license details and the terms and conditions provided by Elsevier and Copyright Clearance Center.

License Number	3981131130923
License date	Nov 02, 2016
Licensed Content Publisher	Elsevier
Licensed Content Publication	Carbon
Licensed Content Title	Doping graphene thin films with metallic nanoparticles: Experiment and theory
Licensed Content Author	Arash Akbari-Sharbaf, Sabastine Ezugwu, M. Shafiq Ahmed, Michael G. Cottam, Giovanni Fanchini
Licensed Content Date	December 2015
Licensed Content Volume Number	95
Licensed Content Issue Number	n/a
Licensed Content Pages	9
Start Page	199
End Page	207
Type of Use	reuse in a thesis/dissertation
Portion	full article
Format	electronic
Are you the author of this Elsevier article?	Yes
Will you be translating?	No
Order reference number	

Title of your thesis/dissertation	Nanoscale thermal and electronic properties of thin films of graphene and organic polyradicals
Expected completion date	Dec 2016
Estimated size (number of pages)	200
Elsevier VAT number	GB 494 6272 12
Requestor Location	Sabastine Ezugwu Dept. Of Physics and Astronomy The University of Western Ontario 1151 Richmond St London, ON N6A 3K7 Canada Attn: Sabastine Ezugwu
Total	0.00 CAD

**JOHN WILEY AND SONS LICENSE
TERMS AND CONDITIONS**

Nov 03, 2016

This Agreement between Sabastine Ezugwu ("You") and John Wiley and Sons ("John Wiley and Sons") consists of your license details and the terms and conditions provided by John Wiley and Sons and Copyright Clearance Center.

License Number	3981140554529
License date	Nov 03, 2016
Licensed Content Publisher	John Wiley and Sons
Licensed Content Publication	Advanced Electronic Materials
Licensed Content Title	Design Criteria for Ultrathin Single-Layer Flash Memristors from an Organic Polyradical
Licensed Content Author	Sabastine Ezugwu, Joseph A. Paquette, Vishal Yadav, Joe B. Gilroy, Giovanni Fanchini
Licensed Content Date	Oct 10, 2016
Licensed Content Pages	1
Type of use	Dissertation/Thesis
Requestor type	Author of this Wiley article
Format	Electronic

Portion	Full article
Will you be translating?	No
Title of your thesis / dissertation	Nanoscale thermal and electronic properties of thin films of graphene and organic polyradicals
Expected completion date	Dec 2016
Expected size (number of pages)	200
Requestor Location	Sabastine Ezugwu Dept. Of Physics and Astronomy The University of Western Ontario 1151 Richmond St London, ON N6A 3K7 Canada Attn: Sabastine Ezugwu
Publisher Tax ID	EU826007151
Billing Type	Invoice
Billing Address	Sabastine Ezugwu Dept. Of Physics and Astronomy The University of Western Ontario 1151 Richmond St London, ON N6A 3K7 Canada Attn: Sabastine Ezugwu
Total	0.00 CAD

**JOHN WILEY AND SONS LICENSE
TERMS AND CONDITIONS**

Nov 03, 2016

This Agreement between Sabastine Ezugwu ("You") and John Wiley and Sons ("John Wiley and Sons") consists of your license details and the terms and conditions provided by John Wiley and Sons and Copyright Clearance Center.

License Number	3981141144456
License date	Nov 03, 2016
Licensed Content Publisher	John Wiley and Sons
Licensed Content Publication	Journal of Polymer Science Part A: Polymer Chemistry

Licensed Content Title	Synthesis, characterization, and thin-film properties of 6-oxoverdazyl polymers prepared by ring-opening metathesis polymerization
Licensed Content Author	Joseph A. Paquette, Sabastine Ezugwu, Vishal Yadav, Giovanni Fanchini, Joe B. Gilroy
Licensed Content Date	Jan 18, 2016
Licensed Content Pages	11
Type of use	Dissertation/Thesis
Requestor type	Author of this Wiley article
Format	Electronic
Portion	Text extract
Number of Pages	2
Will you be translating?	No
Title of your thesis / dissertation	Nanoscale thermal and electronic properties of thin films of graphene and organic polyradicals
Expected completion date	Dec 2016
Expected size (number of pages)	200
Requestor Location	Sabastine Ezugwu Dept. Of Physics and Astronomy The University of Western Ontario 1151 Richmond St London, ON N6A 3K7 Canada Attn: Sabastine Ezugwu
Publisher Tax ID	EU826007151
Billing Type	Invoice
Billing Address	Sabastine Ezugwu Dept. Of Physics and Astronomy The University of Western Ontario 1151 Richmond St London, ON N6A 3K7 Canada Attn: Sabastine Ezugwu
Total	0.00 CAD

Permission for Figure 1.4:

Three-dimensional scanning near field optical microscopy (3D-SNOM) imaging

of random arrays of copper nanoparticles: implications for plasmonic solar cell enhancement

S. Ezugwu, H. Ye and G. Fanchini, *Nanoscale*, 2015, 7, 252

DOI: 10.1039/C4NR05094K

If you are not the author of this article and you wish to reproduce material from it in a third party non-RSC publication you must [formally request permission](#) using RightsLink. Go to our [Instructions for using RightsLink page](#) for details.

Authors contributing to RSC publications (journal articles, books or book chapters) do not need to formally request permission to reproduce material contained in this article provided that the correct acknowledgement is given with the reproduced material.

CURRICULUM VITAE

SABASTINE CHUKWUEMEKA EZUGWU

Education

- 2016 **Doctor of Philosophy (Physics)**, The University of Western Ontario, Canada.
- 2012 **Master of Science (Physics)**, The University of Western Ontario, Canada.
- 2009 **Master of Science (Solar Energy Physics)**, The University of Nigeria Nsukka, Enugu State, Nigeria.
- 2004 **Bachelor of Technology (Industrial Physics)**, Federal University of Technology Owerri, Imo State, Nigeria.

Publications

Patent

- 1) **S.C. Ezugwu**, G. Fanchini and R. Divigalpitiya. Carbon coated articles and methods for making the same. US patent application number: 69590US002; International Publication Number: WO 2013/096350 A1 (2013)

Referred Proceedings

- 2) **S.C. Ezugwu**, F.I. Ezema, S.N. Agbo, A.B.C. Ekwealor, P.U. Asogwa and R.U. Osuji (2009). Synthesis and characterization of thallium sulphide/cadmium sulphide and lead sulphide/cadmium sulphide thin films grown in a polymer matrix by chemical bath deposition (CBD) method. *24th European Photovoltaic Solar Energy Conference*, 21-25 September 2009, Hamburg, Germany. p. 295 – 298
- 3) **S.C. Ezugwu**, P.U. Asogwa, R.U. Osuji, F.I. Ezema, B.A. Ezekoye, A.B.C. Ekwealor, (2009). CdS thin solid films for photovoltaic application. *International Seminar on Theoretical Physics & National Development*, 5-8 July 2009, Abuja, Nigeria, 2 (2009) 89 – 99.
- 4) F.I. Ezema, R.U. Osuji, **S.C. Ezugwu**, P.U. Asogwa, A.B.C Ekwealor, B.A. Ezekoye, (2009). Chemical bath deposition of heterojunction thin films for solar cell application, *International Conference on Photonics, Nanotechnology and Computer Application*, India (ICOPNAC 2009), 1, 144 – 150.

Peer Reviewed Articles

- 5) **S. Ezugwu**, S. Kazemian, D. W. Choi, R. Bauld and G. Fanchini. Contactless scanning near-field thermo-reflectance imaging. Under Review in *Nanoscale*.
- 6) **S. Ezugwu**, J. A. Paquette, V. Yadav, J. B. Gilroy and G. Fanchini. Design criteria for ultrathin single-layer flash memristors from an organic polyradical. *Advanced Electronic Materials*. (2016) 1600253, DOI: **10.1002/aelm.201600253**
- 7) Ye Li, **S. Ezugwu**, J. Park, R. Bauld, Y. Zhao, A. Sarkissian and G. Fanchin. Cathode deposition, paramagnetic defect formation and performance degradation in polymer–fullerene solar cells. *Solar Energy* 129 (2016) 20 – 27.
- 8) J. Park, A. Akbari-Sharbaz, **S. Ezugwu**, R. Bauld and G. Fanchin. Direct synthesis of highly conducting graphene nanoribbon thin films from graphene ridges and wrinkles. *Acta Materialia* 107 (2016) 96 – 101.
- 9) J. A. Paquette, **S. Ezugwu**, V. Yadav, G. Fanchini and J. B. Gilroy. Synthesis, Characterization, and Thin-Film Properties of 6-Oxoverdazyl Polymers Prepared by Ring-Opening Metathesis Polymerization. *Journal of Polymer Science, Part A: Polymer Chemistry* 54 (2016) 1803 – 1813.
- 10) I. C. Amaechi, A. C. Nwanya, D. Obi, **S. C. Ezugwu**, A. E. Udounwa, A.B.C. Ekwealor, R. U. Osuji, M. Maaza and F. I. Ezema. Structural characterization and electrochemical properties of cerium-vanadium (Ce-V) mixed oxide films synthesized by chemical route method. *Ceramics International* 171 (2016) 128 – 141.
- 11) A. Akbari-Sharbaz, **S. Ezugwu**, M. S. Ahmed, M. G. Cottam and G. Fanchini. Doping graphene thin films with metallic nanoparticles: experiments and theory. *Carbon* 61 (2015) 595 – 601.
- 12) R. Chikwenze and **S. C. Ezugwu**. Sulphur induced changes in the band gap energy and the transparency window of chemical bath deposited ZnO:S thin films. *Chalcogenide Letters* 12(8) (2015) 399 – 406.
- 13) A. C. Nwanya, S. U. Offiah, I. C. Amaechi, S. Agbo, **S. C. Ezugwu**, B. T. Sone, R. U. Osuji, M. Maaza and F. I. Ezema, Electrochromic and electrochemical supercapacitive properties of Room Temperature PVP capped Ni(OH)₂/NiO Thin Films. *Electrochimica Acta* 171 (2015) 128 – 141.
- 14) **S. Ezugwu**, H. Ye and G. Fanchini. Three-dimensional scanning near field microscopy (3D-SNOM) imaging of random arrays of copper nanoparticles: implications for plasmonic solar cell enhancement. *Nanoscale* 7 (2015) 252 – 260.
- 15) S. U. Offiah, A. C. Nwanya, **S. C. Ezugwu**, B. T. Sone, R. U. Osuji, M. Malik, C. D. Lokhande and F. I. Ezema. Chemical Bath Synthesis and physico-chemical Characterizations

of NiO-CoO Composite Thin Films for Supercapacitor applications. *International Journal of Electrochemical Science*. 9 (2014) 5837 – 5848.

- 16) S. U. Offiah, M. O. Nwodo, A. C. Nwanya, **S. C. Ezugwu**, S. N. Agbo, P. U. Ugwuoke, R. U. Osuji, M. Malik and F. I. Ezema. Effects of post-thermal treatments on morphological and optical properties of NiO/Ni(OH)₂ thin films synthesized by solution growth. *Optik* 125 (2014) 2905 – 2908.
- 17) M. S. Ahmed, **S. Ezugwu**, R. Divigalpitiya and G. Fanchini. Relationship between electrical and thermal conductivity in graphene-based transparent and conducting thin films. *Carbon* 61 (2013) 595 – 601.
- 18) **S. Ezugwu**, M.S. Ahmed, R. Bauld, R. Divigalpitiya and G. Fanchini. Influence of the addition of graphene-based materials on the thermophysical properties of Poly(3,4-ethylenedioxythiophene):poly(styrenesulfonate) thin film nanocomposites. *Thin Solid Films* 534 (2013) 520 – 528.
- 19) S. L. Mammah, F. E. Opara, F. B. Sigalo, **S. C. Ezugwu** and F. I. Ezema. Annealing Effect on the Solid State and Optical Properties of α -Fe₂O₃ Thin Films Deposited Using the Aqueous Chemical Growth (ACG) Method. *Materials Sciences and Applications* 3 (2012) 793 – 801.
- 20) S. U. Offiah, P. E. Ugwuoke, A.B.C. Ekwealor, **S. C. Ezugwu**, R. U. Osuji and F. I. Ezema. Structural and spectral analysis of chemical bath deposited copper sulfide thin films for solar energy conversions. *Digest Journal of Nanomaterials and Biostructures* 7(1) (2012) 165 – 174.
- 21) **S. C. Ezugwu**, F. I. Ezema, P. U. Asogwa, A. E. Ajuba, M. P. Ogbu and D. D. O. Eya. The effect of deposition time on the structure and optical properties of ZnO thin films by aqueous chemical growth technique. *Digest Journal of Nanomaterials and Biostructures* 6(3) (2011) 1301 – 1310.
- 22) A. E. Ajuba, **S. C. Ezugwu**, P. U. Asogwa, F. I. Ezema. Composition and optical characterization of ZnO/NiO multilayer thin films: Effect of annealing temperature. *Chalcogenide Letters* 7(10) (2010) 573 – 579.
- 23) **S. C. Ezugwu**, P. U. Asogwa, F. I. Ezema and P. M. Ejikeme. Structural and Optical characterization of PVP-capped lead oxide nanocrystalline thin films. *Optoelectronics and Advanced Materials* 12(8) (2010) 1765 – 1771.
- 24) F. I. Ezema, **S. C. Ezugwu**, P. U. Asogwa, A.B.C. Ekwealor and R.U. Osuji. Synthesis and characterization of CdS nanowires and CdS/TiS nonoflower grown in a polymer matrix by chemical bath deposition (CBD) method. *Optoelectronics and Advanced Materials-Rapid Communications*. 7(5) (2010) 747 – 750.
- 25) **S. C. Ezugwu**, F. I. Ezema and P.U. Asogwa. Synthesis and characterization of ternary

CuSbS₂ thin films: effect of deposition time. *Chalcogenide Letters* 7(5) (2010) 369 – 376.

- 26) P. U. Asogwa, **S. C. Ezugwu**, F. I. Ezema, A.B.C. Ekwealor, B. A. Ezekoye and R. U. Osuji. Effect of thermal annealing on the band gap and optical properties of chemical bath deposited PbS-CuS thin films. *Optoelectronics and Advanced Materials* 11(7) (2009) 940 – 944.
- 27) P. U. Asogwa, **S. C. Ezugwu**, F. I. Ezema and R. U. Osuji. Influence of dip time on the optical and solid state properties of As-grown Sb₂S₃ thin films. *Chalcogenide Letters* 6(7) (2009) 287 – 292.
- 28) **S. C. Ezugwu**, F. I. Ezema, R. U. Osuji, P. U. Asogwa, B. A. Ezekoye, A.B.C. Ekwealor, C. Chigbo, M. Anusuya and M. Mahaboob Beevi. Optical studies of chemically deposited PVA-capped PbS nanoparticle thin films. *Optoelectronics and Advanced Materials – Rapid Communications* 3(6) (2009) 528 – 532.
- 29) **S. C. Ezugwu**, F. I. Ezema, R. U. Osuji, P. U. Asogwa, A.B.C. Ekwealor and B. A. Ezekoye. Effect of deposition time on the band-gap and optical properties of chemical bath deposited CdNiS thin films. *Optoelectronics and Advanced Materials – Rapid Communications* 3(2) (2009) 141 – 144.

CHAPTERS IN BOOKS

- 30) P. Bazylewski, A. Akbari-Sharbaz, **S. Ezugwu**, T. Ouyang, J. Park and G. Fanchini (2016). Graphene Thin Films and Graphene Decorated with Metal Nanoparticles. *In Crystalline and Non-Crystalline Solids*, Edited by Pietro Mandracci. InTech Publication, 1 – 16
- 31) P. U. Asogwa, V. A. Ezekoye and **S. C. Ezugwu** (2009). Alternative Sources of Energy. *In Introduction to Natural Sciences-2*, Edited by Asogwa P. U. New Crest Publishers, Onitsha, Nigeria. 215 – 230.

Awards

2014-2015 Award of Excellence in Teaching, Graduate Teaching Assistant, Physics and Astronomy, University of Western Ontario, Canada

Related work Experience

2008 - 2009: Physics Demonstrator, University of Nigeria, Nsukka.

2011 - 2012: Graduate Teaching Assistant, Western University Canada

2013 - 2016: Graduate Teaching Assistant, Western University Canada